UC Berkeley
UC Berkeley Electronic Theses and Dissertations

Title
Majorana fermions and Dirac edge states in topological phases

Permalink
https://escholarship.org/uc/item/532758sb

Author
Shivamoggi, Vasudha Bhimsen

Publication Date
2011

Peer reviewed|Thesis/dissertation

Majorana fermions and Dirac edge states in topological phases

by

Vasudha Bhimsen Shivamoggi

A dissertation submitted in partial satisfaction of the

requirements for the degree of

Doctor of Philosophy

in

Physics

in the

Graduate Division

of the

University of California, Berkeley

Committee in charge:

Professor J. E. Moore, Chair
Professor A. Vishwanath
Professor D. C. Chrzan

Fall 2011

Majorana fermions and Dirac edge states in topological phases

Copyright 2011

by

Vasudha Bhimsen Shivamoggi

Abstract

Majorana fermions and Dirac edge states in topological phases

by

Vasudha Bhimsen Shivamoggi

Doctor of Philosophy in Physics

University of California, Berkeley

Professor J. E. Moore, Chair

In part 1, we study a realization of a chain of Majorana bound states at the interfaces between alternating ferromagnetic and superconducting regions at a quantum spin Hall insulator edge. In the limit of well separated Majoranas, the system can be mapped to the transverse field Ising model. The disordered critical point can be reached by tuning the relative magnitude or phases of the ferromagnetic and superconducting order parameters. We compute the voltage dependence of the tunneling current from a metallic tip into the Majorana chain as a direct probe of the random critical state. In part 2, we present an analytic prescription for computing the edge dispersion $E(k)$ of a tight-binding Dirac Hamiltonian terminated at an abrupt crystalline edge. Specifically, we consider translationally invariant Dirac Hamiltonians with nearest-layer interaction. We present and prove a geometric formula that relates the existence of surface states as well as their energy dispersion to properties of the bulk Hamiltonian. We further prove the bulk-boundary correspondence between the Chern number and the chiral edge modes for quantum Hall systems within the class of Hamiltonians studied in the paper. Our results can be extended to the case of continuum theories which are quadratic in the momentum, as well as other symmetry classes.

To my parents and Rohi,
with gratitude and affection.

Contents

List of Figures

Acknowledgments

I have been very lucky to grow up and study in an environment that nurtures learning and scholarship. The freedom to read and pursue studies in exactly what one wants does not exist everywhere, especially for women, and I am grateful for the opportunities I have had. My education is a happy product of the American public school system. I've had the good fortune to have excellent teachers and mentors all through my education. Their expertise and dedication is admirable. I can't name them all here, but am especially indebted to Connie Sovie, Robert White, Kathy Savage, Tami Ackerson, Alan Levine, and Joel Moore.

The physics department at Berkeley has been a wonderful place to be for the past six years. Above all, it is friendly and stimulating, and you can't ask for better in a research program. Anne and Donna have tirelessly and somehow always good-naturedly helped me navigate through my years here. I've learned so much from talented groupmates and classmates, and I'm truly happy to have been part of this community.

My parents, far beyond encouraging me to read, kept our house so full of books of every kind that it would take a lifetime to go through them all. This thesis would not have been the same without my sister Rohini and her unending stream of questions, which from the beginning have exercised my skills in explaining. I have wonderful family and friends, in Berkeley and far away from it, and I thank them all for their support and friendship.

Chapter 1

Introduction

On an unremarkable day in 1938, a young man boarded a ship from Palermo to Naples, Italy, and was never heard from again. Ettore Majorana, styled by Fermi as one of the true geniuses of physics on par with Galileo and Newton, had a brilliant if brief career. His most ground-breaking work was the prediction of a fermion equal to its own antiparticle. Though the result lay forgotten for decades, recent years have seen a revival in the fortunes of the Majorana fermion. Current experiments are investigating the Majorana nature of the neutrino, Majorana's original suggestion for his particle. If observed as a fundamental particle, Majorana's theory could force a rethinking of the idea of lepton conservation.

The other branch of promising developments, Majorana fermions as emergent excitations in condensed matter systems, is the focus of part 1 of this thesis. What makes them of fundamental interest in this context is the fact that they are fractional excitations, but in an unusual sense. In contrast to the fractionally charged excitations of fractional quantum Hall (FQH) states, a Majorana fermion is charge-neutral and describes half the degrees of freedom as a usual electron. The discovery that they can be used for topological quantum computation is an important motivating factor in the study of this field. A qubit composed of two Majorana fermions is robust to local decoherence and makes an attractive candidate for quantum memory.

As electronic states, Majorana fermions appear at edges or vortices of Dirac systems in a topological phase. They are a special example of topologically protected edge states, which are the focus of part 2 of this thesis. The properties of these edge states are remarkably insensitive to disorder or material-specific terms that destroy such edge states in ordinary systems – this is the sense in which they are topological. The existence of these edge states signals a boundary between two fundamentally different phases.

Topological phases have been studied before in the context of the strongly interacting FQH states, which require a many-body description. The advantage of studying Dirac systems, as we do here, is that the idea of edge states protected by a bulk topological invariant can be understood within a single-particle framework. The discovery of topological insulators and superconductors has set off an enormous research effort, from the abstract classification of such systems based on their underlying symmetries to the practical applications of spintronics and quantum computation. It has also provided an unexpected means of awakening Majorana's long-dormant theory. Topological edge states, their relation to

bulk invariants, and their behavior as chains of Majorana fermions, are the subject of this thesis.

We begin this introduction in Sec. 1.1 with a simple but illustrative 1D model for topologically protected edge states discovered by Jackiw and Rebbi. In Secs. 1.2-1.3 we introduce Majorana fermions and show how superconductors can host them as solutions reminiscent of the Jackiw-Rebbi model. We also discuss some of the unusual behavior these excitations imply. In Sec. 1.4 we review proposals for realizing Majorana fermions in topological insulators and semiconductors with strong spin-orbit coupling. Finally, Sec. 1.5 contains a brief summary of the main results of this thesis.

1.1   The Jackiw-Rebbi model

Jackiw and Rebbi first discovered localized electron states associated with topological defects in 1D. A two-band model for relativistic electrons obeying the Dirac equation is given by:

$$H\psi(x) = -iv_F\sigma^z\partial_x\psi(x) + \sigma^x m(x)\psi(x) = E\psi(x) \ , \tag{1.1}$$

where σ^i are Pauli matrices written in the basis of electron and hole operators, and we have set $\hbar = 1$ for convenience. When $m(x)$ is equal to a constant m_0, the translational invariance of the system allows us to substitute the crystal momentum k for $i\partial_x$ in Eq. 1.1. The energy eigenvalues are given by $E_\pm = \pm\sqrt{v_F^2 k^2 + m_0^2}$. $m(x)$ is referred to as the mass term since it opens an energy gap analogous to that of the rest mass for relativistic particles. A system obeying Eq. 1.1 thus supports delocalized electrons with energies that occur in $+E/-E$ pairs.

Jackiw and Rebbi discovered that this picture is radically modified when the mass term has a topological defect [44]. The simplest example in 1D is a mass term that switches sign at the origin: $m(x) = m_0 \operatorname{sgn}(x)$. This can arise when the electron is coupled to a field that spontaneously breaks symmetry to take the values $\pm m_0$. The point $x = 0$ represents a domain wall between two degenerate, inequivalent ground states. The key result is that localized at such a defect is a single electron state at the middle of the gap. We solve for this state explicitly by setting $E = 0$ in Eq. 1.1. Multiplying on the left by $i\sigma^z$ gives [89]

$$v_F\partial_x\psi_0(x) - \sigma^y m(x)\psi_0(x) = 0 \tag{1.2}$$

which has the solution

$$\psi_0(x) = \psi_0(0) \ \exp\left[\frac{\lambda}{v_F}\int_0^x dx'm(x')\right] \tag{1.3}$$

for

$$\psi_0(0) = \begin{pmatrix} 1 \\ \lambda i \end{pmatrix} \ , \quad \lambda = \pm 1.$$

For the mass term chosen above, the solution is normalizable for $\lambda = -1$. When $m(x)$ switches sign in the opposite direction, $m(x) = -m_0 \operatorname{sgn}(x)$, the normalizable solution is

given by $\lambda = +1$. This result can be generalized in the following way: each time the mass changes sign at $x = x_0$, there is a zero-energy electron state with wavefunction

$$\psi_0(x) = \psi_0(0) \ \exp\left(\frac{-m_0}{v_F}|x - x_0|\right). \tag{1.4}$$

This solution is sharply localized at the mass defect. Note that Eq. 1.4 could not be a solution of the Schrodinger equation, which requires both $\psi_0(x)$ and $\psi_0'(x)$ to be continuous. However the Dirac equation is only first order and therefore allows solutions with discontinuities in the first derivative.

To understand the topological properties of the zero-energy state, we turn to particle-hole symmetry. As noted above for the constant mass case, the bulk energies of Eq. 1.1 occur in $+E/-E$ pairs. This is a consequence of the properties of the Pauli matrices rather than the particular form of the mass term. The Hamiltonian in Eq. 1.1 anticommutes with $\sigma^y : \{H, \sigma^y\} = 0$. Acting σ^y on an energy eigenstate produces another eigenstate with opposite energy:

$$\begin{aligned} H\left(\sigma^y \psi_E\right) &= -\sigma^y H \psi_E \\ &= -E\sigma^y \psi_E . \end{aligned} \tag{1.5}$$

σ^y maps each eigenstate with energy $+E$ to another with energy $-E$, and guarantees that the solutions come in pairs symmetric about the origin:

$$\sigma^y \psi_E = \psi_{-E} . \tag{1.6}$$

Such states, however, are not topologically protected: even if we manage to engineer a system with two low-energy states, additional terms can push them symmetrically out of the gap and into the bulk bands.

The crucial exception to this picture is an energy eigenstate at $E = 0$. According to Eq. 1.6, such a state is mapped to itself under particle-hole conjugation: $\sigma^y \psi_0 = \psi_0$, and therefore doesn't need a symmetry-related partner. As a check, one can show that the solution found in Eq. 1.3 is an eigenvector of σ^y. The presence of a single eigenstate at $E = 0$ is topologically protected: particle-hole symmetry requires the eigenstates to lie symmetrically about $E = 0$, and without a partner, the state at $E = 0$ is stuck there.[1]

Jackiw and Rebbi originally found this result in a particle physics context, for 1D electrons coupled to a spontaneously broken symmetry boson field. They further showed that as a consequence of the particle-hole symmetry, the fermion number of the zero-energy state is required to be $\pm 1/2$. This remarkable discovery of fractionalization was soon followed by a similar result in a very different system: polyacetylene [45], [86]. In the condensed matter model, a 1D chain with alternating hopping strengths between nearest neighbors has two possible ground states (Fig. 1.1(a)). Analogous to the Jackiw-Rebbi model, a domain wall between the two ground states (Fig. 1.1(b)) creates a zero-energy electron state localized at the interface. In a spinless system, this mid-gap state would have fractional charge

---

[1]In this chapter, we use the term "mid-gap state" to describe a topologically protected state which is constrained by particle-hole symmetry to the center of the gap, $E = 0$. It should be noted, however, that in single-particle models without the $+E/-E$ symmetry, a mid-gap state can lie anywhere inside the gap.
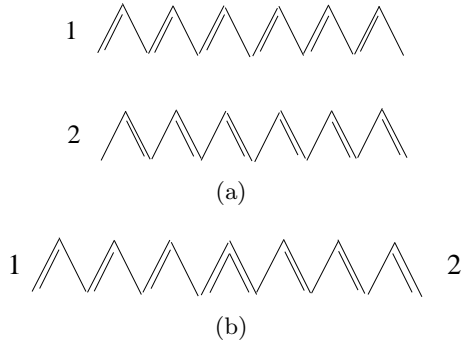
Figure 1.1: (a) A chain with alternating hopping strengths has two degenerate ground states, 1 and 2. (b) A domain wall, consisting of two adjacent bonds of equal strength, interpolates between the ground states 1 and 2. A zero-energy electron state with charge $\pm\frac{1}{2}$ is localized at the defect.

$q = \pm e/2$; however the presence of two distinct spin species in polyacetylene obscures this effect.

Despite its simplicity, the Jackiw-Rebbi model has been generalized to describe many other examples of fractionalization and topologically protected states in condensed matter systems. Defects in 2- or 3D can be studied using dimensional reduction, and more complicated mass terms can be included using Dirac Gamma matrices (higher dimensional generalizations of the Pauli matrices). In part 2 of this thesis, we shall derive an analytic method to relate these topologically protected localized states to a bulk topological invariant. Now we turn to a specific example, Majorana fermions.

1.2 Majorana Fermions

The defining property of a Majorana fermion is that it is indistinguishable from its own antiparticle. This requires a Majorana fermion to be charge-neutral, since the antiparticle of an electrically charged particle has opposite charge and is therefore physically distinct. Charged particles arise from complex fields, with complex conjugation giving rise to antiparticles. Majorana fermions are therefore necessarily described by real fields. Ettore Majorana made the startling discovery that such fields can be found as solutions to the complex-valued Dirac equation [58], opening the door to a new kind of particle unlike either the conventional bosons or fermions of quantum theory.

Let's begin with the Dirac equation, which is the relativistic analogue of the Schrodinger equation for electrons [94]:

$$(i\gamma^\mu \partial_\mu - m)\,\psi = 0. \tag{1.7}$$

Here γ^μ are called the Dirac Gamma matrices and obey the Clifford algebra, $\{\gamma^\mu, \gamma^\nu\} = 2\eta^{\mu\nu}$. Dirac found Gamma matrices satisfying this algebra which contain both real and

imaginary matrix elements. The solution for the field ψ is then required to be complex-valued as well, a necessary feature for a description of the electrically charged electron. The ground state consists of filled negative-energy states and empty positive-energy states. We can add excitations by populating a positive-energy state to create an electron, or depopulating a negative-energy state to create a hole. The subsequent observation of the positron solidified the Dirac equation as the correct description of the electron and its antiparticle.

Majorana, however, was uncomfortable with the infinite sea of filled negative-energy states [81] and sought to eliminate it by identifying negative-energy excitations with positive ones. For this, one needs particles that are equal to their own antiparticles, and Majorana argued that the Dirac equation allows such solutions. He showed that using an alternate representation to Dirac's, it is possible to write Gamma matrices that satisfy the Clifford algebra and are *purely imaginary*. In this case, Eq. 1.7 has purely real solutions ψ which describe Majorana fermions.

So it is possible for Majorana fermions to exist as relativistic particles; now we turn to the question of which particles. Majorana initially suggested neutrinos, but the apparent distinction between neutrinos and anti-neutrinos as well as lack of neutrino mass seemed incompatible with Majorana fermions. Recent observations of neutrino oscillations, however, have revived speculation on the Majorana nature of neutrinos. The as-yet unobserved neutrino-less double-beta decay requires blurring of neutrinos and anti-neutrinos, and if seen may provide evidence that Majorana fermions can be fundamental particles.

An alternate approach, which is the one studied in part 1 of this thesis, is to search for Majoranas as quasiparticle excitations in condensed matter systems. The electrons that make up these systems are by themselves clearly not Majorana fermions, but several systems in the past decade have been predicted to realize Majorana fermions as low-lying excitations. Emergent excitations can have properties very different from that of the constituent electrons, for example fractionally charged anyonic excitations in FQH states. Majorana fermions can be thought of as the real and imaginary parts of Dirac fermions. Thus two of them are required to describe the degrees of freedom of a single Dirac fermion, and a Majorana is often referred to as "half an electron."

1.3   Superconducting Systems

Before plunging into technical details, we first give an intuitive picture of how Majorana fermions arise in condensed matter systems. Superconductors make Majorana fermions possible in two important ways. First, their ability to absorb or donate Cooper pairs puts the electron and hole on equal standing: an electron is equivalent to a hole, modulo a Cooper pair. Second, superconductors have a built-in particle-hole symmetry that relates positive and negative energy eigenstates. The standard BCS approach is to work with two copies of the system – one in terms of electrons and one in holes, solve for the energies, and then recover the original system by taking only half the solutions as physical. As seen above, the Dirac equation in the presence of a topological defect admits a single zero-energy electron state. In a superconductor, only half of this state is physical, making it possible for the zero-energy state to be a Majorana fermion.

1.3.1   Zero-energy Edge States

This argument can be make more formal by considering the BCS Hamiltonian for pairing between like spins [71]. (Why equal spins are necessary will be discussed below.)

$$H_{BCS} = \sum_{\mathbf{k}} \xi_{\mathbf{k}} c_{\mathbf{k}}^\dagger c_{\mathbf{k}} + \frac{1}{2} \left(\Delta_{\mathbf{k}}^* c_{-\mathbf{k}} c_{\mathbf{k}} + \Delta_{\mathbf{k}} c_{\mathbf{k}}^\dagger c_{-\mathbf{k}}^\dagger \right) \tag{1.8}$$

Here $c_{\mathbf{k}}$ and $c_{\mathbf{k}}^\dagger$ are creation and annihilation operators of an electron with momentum $\mathbf{k}$, and we have dropped the spin index for convenience. $\xi_{\mathbf{k}}$ is the single-particle energy and approaches the chemical potential μ as $\mathbf{k}$ goes to zero. The spin component of the Cooper pair is symmetric under parity, therefore the gap function $\Delta_{\mathbf{k}}$ must be odd to satisfy Fermi statistics. For low $\mathbf{k}$, it is simplest to take $\Delta_{\mathbf{k}} \approx \Delta_0(k_x - ik_y)$ to describe complex p-wave pairing. The Hamiltonian in Eq. 1.8 can be diagonalized by defining quasiparticles $\alpha_{\mathbf{k}}$ that satisfy $[\alpha_{\mathbf{k}}, H_{BCS}] = E_{\mathbf{k}} \alpha_{\mathbf{k}}$. This is done using the Bogoliubov-Valatin transformation [80]:

$$\alpha_{\mathbf{k}} = u_{\mathbf{k}} c_{\mathbf{k}} + v_{\mathbf{k}} c_{-\mathbf{k}}^\dagger \tag{1.9a}$$

$$\alpha_{\mathbf{k}}^\dagger = u_{\mathbf{k}}^* c_{\mathbf{k}}^\dagger + v_{\mathbf{k}}^* c_{-\mathbf{k}} \tag{1.9b}$$

where $|u_{\mathbf{k}}|^2$ and $|v_{\mathbf{k}}|^2$ are given by $\frac{1}{2}(1 \pm \xi_{\mathbf{k}}/E_{\mathbf{k}})$ respectively, and $E_{\mathbf{k}}^2 = \xi_{\mathbf{k}}^2 + |\Delta_{\mathbf{k}}|^2$. The BCS ground state is given by

$$|GS\rangle = \prod_{\mathbf{k}} \left(u_{\mathbf{k}} + v_{\mathbf{k}} c_{\mathbf{k}}^\dagger c_{-\mathbf{k}}^\dagger \right) |0\rangle. \tag{1.10}$$

$|v_{\mathbf{k}}|^2$ gives the probability of a Cooper pair between electrons of momentum $+\mathbf{k}$ and $-\mathbf{k}$, and normalization requires that $|u_{\mathbf{k}}|^2 + |v_{\mathbf{k}}|^2 = 1$.

$\alpha_{\mathbf{k}}^\dagger$ is the creation operator of a quasiparticle excitation at momentum $\mathbf{k}$. To get a Majorana excitation at zero-energy we require $\alpha_0^\dagger = \alpha_0$, and Eqs. 1.9a-1.9b imply that $u_0 = v_0^*$. Together with the normalization constraint, there are two ways to satisfy this condition: with u_0 and v_0 both purely real or both purely imaginary. These two possibilities define the Majorana operators associated with the zero-energy electron mode:

$$\gamma_1 = \frac{1}{\sqrt{2}}(c_0 + c_0^\dagger) \,, \tag{1.11a}$$

$$\gamma_2 = \frac{i}{\sqrt{2}}(c_0 - c_0^\dagger) \,. \tag{1.11b}$$

Note that both these solutions satisfy $\gamma_i^\dagger = \gamma_i$, and obey the anticommutation relations $\{\gamma_i, \gamma_j\} = \delta_{ij}$.

Now we are in a position to see why pairing between like spins is a requirement for Majorana fermions. In an s-wave superconductor, where Cooper pairs form spin-singlets and the gap function is even under parity, the quasiparticle operators analogous to Eqs. 1.9a-1.9b become

$$\alpha_{\mathbf{k}} = u_{\mathbf{k}} c_{\mathbf{k}\uparrow} + v_{\mathbf{k}} c_{-\mathbf{k}\downarrow}^\dagger \tag{1.12a}$$

$$\alpha_{\mathbf{k}}^{\dagger} = u_{\mathbf{k}}^* c_{\mathbf{k}\uparrow}^{\dagger} + v_{\mathbf{k}}^* c_{-\mathbf{k}\downarrow} \ . \tag{1.12b}$$

In this case, even at $\mathbf{k} = 0$, there is no way to satisfy the Majorana condition $\alpha_{\mathbf{k}} = \alpha_{\mathbf{k}}^{\dagger}$ as the spins are always off. Thus p-wave pairing is crucial to the existence of Majorana excitations.

The Majorana operators in Eqs. 1.11a- 1.11b were found as the self-adjoint excitations of H_{BCS}, but in retrospect we could have just written them down as the real and imaginary components of the electron operator c_0. Neglecting spin, an electron state comes with two degrees of freedom: it can be occupied or unoccupied, which we describe using the operators c and $c^{\dagger}$. In the Majorana representation, these two degrees of freedom are described using operators of two *different* fermions γ_1 and γ_2, each of which is equal to its own adjoint. The existence of Majorana fermions only becomes well-defined if they are localized and spatially separated. When a Dirac excitation breaks up into two Majorana fermions that can be moved arbitrarily far apart, then the elementary excitations of the system can be viewed as Majorana rather than Dirac.

A $p + ip$ superconductor is in what is known as the weak-pairing phase when $\mu < 0$ and strong-pairing phase when $\mu > 0$, with a phase transition at $\mu = 0$ [71]. In the weak-pairing phase, the system hosts Majorana fermions at vortices and edges, and we give a brief derivation of the latter case here. Read and Green pointed out that an edge between a system in the weak-pairing phase and vacuum is equivalent to a domain wall in the chemical potential. Consider a semi-infinite $p + ip$ superconductor in the weak-pairing phase, with an edge at $x = 0$. We can arrange the particle-number density to vanish outside the superconductor ($x > 0$) by setting μ to be large and positive, while inside the system $\mu < 0$. The edge then marks thus marks a domain wall in μ.

Now let's solve for the zero-energy state localized by the domain wall. The Bogoliubov-de Gennes equations, which determines $u_{\mathbf{k}}$ and $v_{\mathbf{k}}$ and are derived by implementing $[\alpha_{\mathbf{k}}, H_{BCS}] = E_{\mathbf{k}}\alpha_{\mathbf{k}}$, take the following form for small energies:

$$Eu = -\mu u + \Delta_0 i \left(\frac{\partial}{\partial x} + k_y \right) v \tag{1.13a}$$

$$Ev = \mu v + \Delta_0 i \left(\frac{\partial}{\partial x} - k_y \right) u \tag{1.13b}$$

Setting $E = k_y = 0$ gives the normalizable solution

$$u(x) = u_0 \exp \left[-\int_0^x dx' \, \frac{\mu(x')}{\Delta_0} \right] \ . \tag{1.14}$$

Just as in the Jackiw-Rebbi model, a domain wall in the mass term leads to a localized, zero-energy state. For small energies $E \neq 0$, a similar calculation gives chiral states that are bound to the edge and propagate along it.

The same results apply to a vortex, which can be viewed as a circular edge surrounding a region where the order parameter vanishes. The domain wall argument explains why there are no mid-gap edge states when the superconductor is in the strong-pairing phase. In this case $\mu > 0$ on both sides of the edge, and without a defect in μ no zero-energy state is possible. Thus Majorana fermions are bound to edges and vortices in $p + ip$ superconductors in the weak-pairing phase.
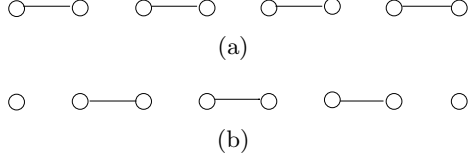
Figure 1.2: (a) When $t = 0$ every Majorana operator is paired with another, and the ground state is non-degenerate. (b) For $\mu = 0$ the two Majorana operators at the ends of the chain are left unpaired, leading to a two-fold degeneracy in the ground state.

1.3.2   Kitaev Model

Kitaev found a simpler way to derive Majorana edge states in a 1D wire which introduced an important motivating reason to study these excitations: the use of Majoranas to form topologically protected qubits [50]-[51]. Consider the Hamiltonian for a long chain with hopping and p-wave pairing between nearest neighbors:

$$H = -\sum_j \left[\mu \left(c_j^\dagger c_j - \frac{1}{2} \right) + t c_j^\dagger c_{j+1} + \Delta_0 c_j^\dagger c_{j+1}^\dagger + h.c. \right] \; . \tag{1.15}$$

Switching to Majorana variables, $\gamma_{2j-1} = (c_j + c_j^\dagger)/\sqrt{2}$ and $\gamma_{2j} = i(c_j^\dagger - c_j)/\sqrt{2}$, and treating the case where $t = \Delta_0$, Eq. 1.15 becomes

$$H = i \sum_j \left(-\mu \; \gamma_{2j-1} \gamma_{2j} + 2t \; \gamma_{2j} \gamma_{2j+1} \right) \; . \tag{1.16}$$

This model has two phases, with a phase transition at $\mu = 2t$. For an intuitive understanding of these phases, it is helpful to consider two limiting cases. First, when $t = \Delta_0 = 0$, the only interactions are between Majoranas corresponding to the same electron (Fig. 1.2(a)). The ground state is non-degenerate, with each electron state being unoccupied.

In the other limiting case with $\mu = 0$, the terms in the Hamiltonian connect Majoranas from different electrons, leaving one free Majorana on either end of the chain (Fig. 1.2(b)). Now there are two degenerate ground states $|\psi_0\rangle$ and $|\psi_1\rangle$, which are distinguished by the operator $P = -i\gamma_1\gamma_L$:

$$-i\gamma_1\gamma_L \; |\psi_0\rangle = +|\psi_0\rangle \;\; , \quad -i\gamma_1\gamma_L \; |\psi_1\rangle = -|\psi_1\rangle \; . \tag{1.17}$$

To get a better understanding of the operator P, imagine creating Dirac operators from γ_1 and γ_L: $c_b = (\gamma_1 - i\gamma_L)/\sqrt{2}$, $c_b^\dagger = (\gamma_1 + i\gamma_L)/\sqrt{2}$. In terms of this new variable, $P = -(c_b^\dagger c_b - \frac{1}{2})$ and measures the fermion number parity. The two ground states $|\psi_0\rangle$ and $|\psi_1\rangle$ thus have even and odd fermion parity respectively, corresponding to an unoccupied and occupied electron state.

Although we worked out two extreme cases on the phase diagram, it can be shown that the results are generic to the entire phase [50]. For $\mu > 2t$, the ground state is non-degenerate. For $\mu < 2t$, the chain has one free Majorana fermion at each end as well as two degenerate ground states that differ by fermion parity.

1.3.3 Majorana Oddities

We should pause here to note the unusual nature of this electron state. It arises from two Majorana fermions localized at opposite ends of the chain, and is therefore highly non-local. This property is exactly what makes such electron states promising candidates for quantum computation. The two-state system needed to make a qubit can come from the spin-up and spin-down states of an electron. Unfortunately these states are very susceptible to local decoherence, which makes them undesirable for quantum memory. By contrast, a qubit created from two Majoranas stores information in two spatially separated locations. Local sources of decoherence cannot simultaneously act on both ends of the chain, making this qubit robust to error.

Tunneling

Tunneling an electron in a qubit composed of Majorana fermions is markedly different from tunneling into an ordinary electron state. Consider two Majoranas located at $x = \pm L$. The Majorana states are localized, and one may naively expect an electron tunneling into the system at $x = -L$ to fill the Majorana state localized at $x = -L$ as well. The Majorana state, however, doesn't conserve fermion number since it mixes electrons and holes. Instead, it is the linear combinations of the two Majorana states, analogous to $|\psi_0\rangle$ and $|\psi_1\rangle$ in the 1D wire, that are eigenstates of fermion parity and energy. When an electron tunnels into either Majorana fermion, it couples to one of these non-local states.

A tunneling process into an ordinary electron state has two possible outcomes: 1. if the state is empty, the electron fills it, and 2. if the state is already occupied, Pauli exclusion forbids the process. By contrast, Majorana fermions allow tunneling to occur in two distinct ways. Suppose the system is initially in the state with the effective electron state unoccupied, $|\psi_0\rangle$. Tunneling an electron in bumps the state up to $|\psi_1\rangle$, so far nothing unexpected. Now consider the system to be in the occupied state $|\psi_1\rangle$. Tunneling an electron in switches the system back to $|\psi_0\rangle$, rather than annihilating it. The tunneled electron and the electron effectively occupying the qubit are both absorbed by the superconductor as a Cooper pair. This peculiar result is due to the fact that $\gamma_i^2 = 1$ for a Majorana operator, rather than 0 as for electron operators.

Statistics

In addition to forming non-local qubits, Majorana fermions are attractive candidates for quantum computation because they obey non-Abelian statistics. A system with $2N$ Majorana states can have N Dirac states. Since the Majorana fermions have zero energy, the ground state has a degeneracy of 2^N, corresponding to each Dirac state being filled or empty. This degeneracy allows for the existence of non-trivial statistics. 2D braiding operations that move one Majorana around another not only result in a phase factor, making them anyons, but can also move the system from one of the degenerate ground states to another. Two distinct operations need not commute; hence the terminology non-Abelian.

The term "Majorana fermion" is therefore a bit misleading. The operators describing these excitations obey fermionic anticommutation relations; under interchange, however, they display novel behavior quite different from ordinary fermionic statistics. This property depends crucially on the Majorana excitations being well-separated, since interactions be-

tween nearby Majoranas cause energy splittings and destroy the ground state degeneracy. The non-Abelian statistics marks a fundamental difference between condensed matter manifestations of Majoranas and high energy proposals. High energy Majorana fermions have mass, which implies a non-degenerate ground state and conventional fermionic statistics.

There has been much recent work on ways to utilize the unusual statistics to manipulate qubits [64], [12]. Here we will only mention observable consequences of a more mundane transformation property of Majorana fermions. Referring back to Eq. 1.15, a change in the superconducting phase $\Delta_0 \to \Delta_0 e^{i\phi}$, can be eliminated through a gauge transformation $c \to ce^{i\phi/2}$, $c^\dagger \to c^\dagger e^{-i\phi/2}$. When ϕ advances by 2π, this implies that the Majorana operators pick up a minus sign: $\gamma_i \to -\gamma_i$ [43].

This seemingly simple result can be used to derive the non-Abelian statistics and has surprising experimental signatures. Imagine forming a Josephson junction between Majorana bound states γ_1 and γ_2 at $y = \pm L$ respectively. While the phase at $y = -L$ is held fixed, the phase at $y = +L$ is advanced by 2π. According to the transformation rule derived above, γ_1 is unchanged while $\gamma_2 \to -\gamma_2$. The Dirac operator created from these two Majorana operators transform as

$$c \to c^\dagger \quad , \quad c^\dagger \to c \tag{1.18}$$

which is equivalent to switching fermion parity. Advancing the superconducting phase by 2π switches the ground state from even-parity to odd, or vice versa. Two such processes are required to bring the system back to its original state, leading to an unusual 4π-periodicity in the Josephson effect rather than the conventional 2π [26], [50].

For chiral Majorana fermions that propagate along some interface, this relative minus sign can be observed through interferometry. Suppose we have gap-crossing chiral electrons that split up into two Majorana branches. The Majorana fermions take separate paths before joining up again at a further point. If the region enclosed by the two Majorana paths contains n flux quanta, the Majorana operators transform as

$$\gamma_1 \to \gamma_1 \quad , \quad \gamma_2 \to (-1)^n \gamma_2 \ . \tag{1.19}$$

When n is odd, the relative minus sign means that the Majorana fermions join together to form a hole. In this way, electrons can be converted to holes through interference of the Majoranas [3], [27].

1.4 Proposed Realizations

In this section, we turn to the issue of finding materials that host Majorana fermions in their excitation spectrum. The early work of Read and Green as well as Kitaev both relied crucially on p-wave pairing, which unfortunately has proven difficult to find in nature. Sr_2RuO_4 is a superconducting material predicted to have a $p + ip$ time-reversal-breaking phase [57], but experimental detection of Majorana excitations remains inconclusive. A related phase is the Moore-Read wavefunction believed to describe the $\nu = 5/2$ FQH state, which can be viewed as a $p + ip$ superconductor of composite fermions [71]. Here too, interferometry studies of the charge and statistics of the excitations are promising, but

yet to be fully convincing [93]. A major breakthrough of the last few years has been the idea to *engineer* p-wave pairing from conventional s-wave superconductors using spin-orbit coupling. We discuss two such proposals in this section.

1.4.1 Topological Insulators

The idea to create p-wave pairing artificially was first proposed by Fu and Kane using topological insulators (TI) [30], a class of insulating materials where strong spin-orbit coupling leads to a band inversion [36], [69]. This topologically non-trivial phase supports gapless edge or surface states that are protected by a bulk topological invariant [47], [46], [62]. In 2D this phase has been observed in HgTe sandwiched between layers of CdTe. Above a critical thickness, the bands of the HgTe layer are inverted, and transport measurements indicate conductance due to gapless edge modes [53]. In the simplest case, these "helical" edge modes consist of counter-propagating spin-up and spin-down electrons, hence the terminology "quantum spin Hall" (QSH) for this phase.

The proximity effect between an s-wave superconductor and these surface states leads to a superconducting state that is time-reversal-symmetric but topologically similar to the $p + ip$ superconductor, with Majorana fermions trapped in vortices. The calculation is presented in some detail in Chp. 2, so we skip the derivation here. Adding ferromagnetic material between two superconducting regions of different phase gives a probe of the fractional Josephson effect [26]. Related setups examine chiral Majorana fermions via interferometry or tunneling [3], [27], [55].

The discovery that p-wave pairing can be manufactured out of conventional superconductors reinvigorated the search for Majoranas. In addition to proximity setups, Majoranas are also predicted to exist in vortices of Bi_2Te_3, which has been shown to be a bulk superconductor [39]. A substantial material difficulty, however, lies in the fact that these materials are not very good insulators. Without a large band gap, the mid-gap Majorana states lose their topological protection and are harder to detect.

1.4.2 Semiconducting Nanowires

Recent studies of the semiconductors InSb and InAs made the unexpected prediction that these systems can host Majorana fermions as well [77]. Although not intrinsically topological in nature, these materials have strong spin-orbit coupling which drives the system into a topological phase when in proximity to an s-wave superconductor. To see how the spin-orbit interaction induces p-wave pairing, we start with the Hamiltonian [4]

$$H_0 = \int d^2\mathbf{r}\psi^\dagger \left[-\frac{\nabla^2}{2m} - \mu - i\alpha(\sigma^x\partial_y - \sigma^y\partial_x) \right] \psi \qquad (1.20)$$

where α is the strength of the Rashba coupling, and the Pauli matrices act on the spin sector. The presence of this term creates two spin-split bands which cross at $\mathbf{k} = 0$. Depositing a ferromagnetic insulator on the material introduces the term

$$H_M = \int d^2\mathbf{r}\psi^\dagger \left(V_Z\sigma^z \right) \psi \qquad (1.21)$$

which opens a gap of size $|2V_Z|$ between the two bands. When the chemical potential μ is chosen so that the Fermi level lies within the gap, the Fermi surface consists of two points with opposite $\mathbf{k}$ and spin. This scenario is crucial since the oppositely aligned spins can pair up in proximity to an s-wave superconductor. It can be shown formally that adding such a term,

$$H_{SC} = \int d^2\mathbf{r} \left(\Delta_0 \psi_\uparrow^\dagger \psi_\downarrow^\dagger \right) \tag{1.22}$$

creates s-wave pairing when $\Delta_0 \gg |V_Z - \mu|$, but also p-wave pairing when $\Delta_0 \ll |V_Z - \mu|$. Thus a phase transition at $\Delta_0^2 = V_Z^2 - \mu^2$ separates a topological phase, with Majorana fermions trapped in vortices, from a trivial phase. With a suitable combination of Rashba and Dresselhaus coupling, the ferromagnetic insulator may be replaced by an in-plane magnetic field for a more experimentally feasible setup [4]. Further extensions to 1D nanowires show that it is possible to probe the non-Abelian nature of the excitations using T-junctions [66], [5]. The prediction of Majorana excitations in these materials has been the cause of much optimism since experimentally they are well-studied and have an observed proximity effect [91], [15].

1.5 Summary of this thesis

1.5.1 Part I: Random Majorana Chain

A chain of Majorana fermions may be created by alternately depositing ferromagnetic (FM) and superconducting (SC) regions along a QSH edge. A single zero-energy Majorana fermion appears at each SC/FM boundary if it is sufficiently narrow, and we study how unique features of the chain can be observed using a metallic tunneling tip. An ideal, uniform system realizes the interesting free-Majorana fermion quantum critical point. Realistically, however, FM and SC domains will inevitably vary randomly in size and proximity amplitude, and therefore the proposed system would realize an even more interesting model: the random Majorana fermion chain in its random-singlet phase [13]. So far, likely experimental Majorana signatures in the shot noise were discussed for a single Majorana pair [11], [65], [55]. Experimentally, it may be even simpler to pattern an irregular phase-separated mixture of SC and FM materials to contact the QSH edge, rather than a precise controlled-lithography FM-SC-FM configuration.

Furthermore, the Majorana fermion chain may give a first convincing measurement of the random-singlet phase and its associated Griffiths scaling. Contrary to spin chains where neutron scattering or other spin-sensitive probes can only give limited information, the Majorana chain setup allows a direct electronic tunneling measurement that reveals the nature of the random singlet phase. Although this model is based on FM and SC regions coupled to the QSH edge, the critical properties calculated here also apply to other setups. For example, a Majorana chain can also be realized by applying a magnetic field to a quantum wire with spin-orbit coupling [77], [66]. An experimental realization of these systems will most likely include randomness in the location of the superconducting vortices, and thus the Majorana fermions.

In Chp. 2, we calculate the energies of the Majorana bound states of an QSH-FM-SC heterostructure and then find the Hamiltonian for the Majorana fermion chain. In

Chp. 3, we map the model onto the random transverse-field Ising model and discuss a real-space renormalization group (RSRG) method for studying low-energy behavior. In Chp. 4, we generalize a method of implementing the RSRG as unitary transformations in order to study a Majorana chain coupled at one end to an STM lead. In Chp. 5, we calculate the energy levels of a critical Majorana chain coupled at one end to an STM lead and find the voltage dependence of the tunneling current. A two-lead setup is considered in Chp. 6, where we compute heat and electrical conductance through the Majorana chain.

1.5.2 Part II: Bulk-Boundary Correspondence

Topological order is responsible for interesting new states of matter that do not fit into the standard symmetry-breaking picture. [92] For decades, the Landau paradigm successfully described systems by looking at the underlying symmetries, with phase transitions occurring between phases with different symmetries. However the integer quantum Hall (IQH) effect showed this approach to be incomplete, since it exhibits transitions between phases of the same symmetry. These phases are instead distinguished by topological order, with gapless modes localized at domain walls between regions of different topological order.

For systems with a non-zero bulk gap at all points in the Brillouin zone, it is possible to define a topological invariant of the Hamiltonian. Systems with non-trivial topological invariants are termed topological insulators (TI) and topological superconductors. The invariants are robust to smooth deformations that do not close the bulk gap and underlie the precise quantization of response functions in topologically ordered systems. [36, 70, 79, 52] This was first realized in IQH states, where the Hall conductivity can be expressed as the first Chern number of the $U(1)$ vector bundle of Bloch states. [90, 8, 84] For time-reversal invariant (TRI) systems in two-dimensions (2D), a $\mathbb{Z}_2$ topological invariant distinguishes between the vacuum (trivial phase) and the quantum spin Hall (QSH) state. [47, 46, 9, 53] In three-dimensions (3D), there are four $\mathbb{Z}_2$ invariants describing TRI systems, one of which distinguishes between the vacuum and a strong topological insulator and is robust to disorder. [31, 63, 74, 41, 95, 18] The quantized magnetoelectric response may be written in terms of this $\mathbb{Z}_2$ invariant. [67, 21]

Although a topological invariant is an abstract quantity defined for a fully periodic system, it is manifested physically as mid-gap surface states. In IQH systems, the quantized Hall conductance can be formulated in terms of the the number of chiral edge states. [54, 35] Similarly, the 2D/3D $\mathbb{Z}_2$ invariant for TRI systems determines whether there are an odd or even number of helical modes/Dirac cones at a given edge or surface. [28] In the cases above, the edge states smoothly connect the bulk valence and conduction bands and the number of such modes is protected by the topological invariant: they cannot be deformed into a single bulk band unless the bulk gap closes. By contrast, edge modes in an ordinary system do not traverse the bulk gap and are thus susceptible to localization by disorder. For superconducting systems, the topological invariants determine the number of Majorana modes localized at the edge or in vortices. [61, 71] These states are at zero energy and are protected by particle-hole symmetry and the superconducting gap. Systems such as $p + ip$ superconductors (SC) in the "weak pairing phase" or SC-TI heterojunctions can support Majorana modes which obey non-Abelian statistics. [30, 43]

The goal of this part is to derive a rigorous connection between the bulk invari-

ants and the surface dispersion. A heuristic way to understand this bulk-boundary is as follows. Consider a domain wall between two bulk insulators with suitably defined topological invariants that take the values ν_L and $\nu_R \neq \nu_L$ in some regions. Since the value of the invariant cannot change for finite energy gap, this means the bulk gap closes at some interface. Mid-gap excitations can thus exist, but they are confined to the interface by the bulk gap in the other regions. This argument applies to domain walls between regions with different values of the invariant, of which an edge is a special case where one of the regions is the vacuum (trivial phase).[44, 88].

In Chp. 7, we introduce the bulk quantities of a lattice Hamiltonian that determine topological behavior. We also state the two main results of the paper, Theorem 1 relating the parameters of the bulk Hamiltonian to the surface spectrum in a geometric way, and Theorem 2 proving the bulk-boundary correspondence between chiral edge states and the Chern number. The proofs are presented separately in Chps. 9-10. In Chp. 8, we demonstrate the range of applicability of our theorems and give examples of topologically ordered systems. We extend the results from lattice Hamiltonians to continuum quadratic Hamiltonians, with discussions on its implications.

Part I

Random Majorana Chain

Chapter 2

FM-SC-QSH Heterostructures

In this chapter, we consider edge states of a QSH system that are gapped via coupling to FM and SC materials. We show that a vortex in the phase of the pair potential or in the magnetization results in Majorana bound states localized at the interfaces. To leading order, the Hamiltonian for the Majorana chain consists of nearest-neighbor interactions between these bound states.

2.1 Ferromagnetic regions at QSH edge

Before solving the full problem with the SC regions, it is useful to examine the case of FM material whose magnetization changes direction across a sharp interface. Without a pairing term, the Hamiltonian conserves fermion number and cannot support Majorana bound states. However, solving this problem gives insight into the zero-energy electron state that "splits" into two Majorana states in the presence of the SC. In this section, we find solutions in each region and then impose boundary conditions at the interface to solve for the energies and wavefunctions. The Hamiltonian for QSH edge states coupled to FM material is given by

$$H = \left(\psi_\uparrow^\dagger \ \psi_\downarrow^\dagger \right) \begin{pmatrix} -iv\partial_x - \mu & M^*(x) \\ M(x) & iv\partial_x - \mu \end{pmatrix} \begin{pmatrix} \psi_\uparrow \\ \psi_\downarrow \end{pmatrix} \tag{2.1}$$

where the diagonal terms express the helical nature of the QSH edge states, and the off-diagonal terms are due to the FM material. This is expressed more compactly as $H = \frac{1}{2} \Psi^\dagger \mathcal{H} \Psi$ for

$$\Psi = (\psi_\uparrow, \psi_\downarrow)^T \tag{2.2}$$

$$\mathcal{H} = -iv\partial_x \sigma^z + \operatorname{Re} M(x)\sigma^x + \operatorname{Im} M(x)\sigma^y - \mu \tag{2.3}$$

where σ^i are Pauli matrices that act on the space of right and left movers. Note that when $M(x)$ is uniform, the bulk energy is given by

$$E(k) = \mu \pm \sqrt{v^2 k^2 + M_0^2} \tag{2.4}$$

The bulk band is gapped when $M_0 > \mu$. For the remainder of this chapter, we set $\mu = 0$.

When the direction of the magnetization changes at $x = 0$, the term due to the ferromagnetic coupling in the Hamiltonian can be written as

$$\mathcal{H}_M = M_0 \left[\Theta(x) + \cos\phi \; \Theta(-x) \right] \sigma^x + M_0 \sin\phi\,\Theta(-x)\sigma^y \tag{2.5}$$

where $\Theta(x)$ is the Heaviside function. We look for solutions of the Hamiltonian in each region.

Region I $(x < 0)$:

$$\mathcal{H} = -iv\partial_x\sigma^z + M_0 \cos\phi \; \sigma^x + M_0 \sin\phi \; \sigma^y \tag{2.6}$$

Solutions to $\mathcal{H}\psi = E\psi$ are given by

$$\psi_{A_1}, \psi_{B_1} = e^{\pm \int_0^x dx'/\lambda} \begin{pmatrix} \frac{iM_0}{v}e^{-i\phi} \\ \mp\frac{1}{\lambda} + \frac{iE}{v} \end{pmatrix} \tag{2.7}$$

where

$$\lambda \equiv \frac{v}{\sqrt{M_0^2 - E^2}} \tag{2.8}$$

The general solution for the wavefunction in Region I is given by $\psi_I = A_1\psi_{A_1} + B_1\psi_{B_1}$. Note that ψ_{A_1} is normalizable in this region while ψ_{B_1} is not.

Region II $(x > 0)$:

$$\mathcal{H} = -iv\partial_x\sigma^z + M_0 \; \sigma^x \tag{2.9}$$

Solutions to $\mathcal{H}\psi = E\psi$ are

$$\psi_{A_2}, \psi_{B_3} = e^{\mp \int_0^x dx'/\lambda} \begin{pmatrix} \frac{iM_0}{v} \\ \pm\frac{1}{\lambda} + \frac{iE}{v} \end{pmatrix} \tag{2.10}$$

The general solution for the wavefunction in Region II is given by $\psi_{II} = A_2\psi_{A_2} + B_2\psi_{B_2}$. We continue the notation that ψ_{A_2} and ψ_{B_2} are the normalizable and non-normalizable solutions respectively.

Matching solutions at each interface

By imposing continuity on the wavefunctions at $x = 0$, we can derive a quantization condition on the energy. This restriction can be written in terms of a transfer matrix:

$$\begin{pmatrix} A_2 \\ B_2 \end{pmatrix} = \begin{pmatrix} T_{11} & T_{12} \\ T_{21} & T_{22} \end{pmatrix} \begin{pmatrix} A_1 \\ B_1 \end{pmatrix} \tag{2.11}$$

To solve for the matrix elements, we set $\psi_I(0) = \psi_{II}(0)$ and get the following equation:

$$A_1 \begin{pmatrix} \frac{iM_0}{v}e^{-i\phi} \\ -\frac{1}{\lambda} + \frac{iE}{v} \end{pmatrix} + B_1 \begin{pmatrix} \frac{iM_0}{v}e^{-i\phi} \\ \frac{1}{\lambda} + \frac{iE}{v} \end{pmatrix} = A_2 \begin{pmatrix} \frac{iM_0}{v} \\ \frac{1}{\lambda} + \frac{iE}{v} \end{pmatrix} + B_2 \begin{pmatrix} \frac{iM_0}{v} \\ -\frac{1}{\lambda} + \frac{iE}{v} \end{pmatrix} \tag{2.12}$$

The top line of Eq. 2.12 is equivalent to

$$A_2 = e^{-i\phi}A_1 + e^{-i\phi}B_1 - B_2 \tag{2.13}$$

After some uninteresting algebra, Eqs. 2.12-2.13 reduce to

$$B_2 \sim \left\{ A_1 \left[\left(-\frac{1}{\lambda} + \frac{iE}{v} \right) - e^{-i\phi} \left(\frac{1}{\lambda} + \frac{iE}{v} \right) \right] + B_1 \left[\left(\frac{1}{\lambda} + \frac{iE}{v} \right) - e^{-i\phi} \left(\frac{1}{\lambda} + \frac{iE}{v} \right) \right] \right\} \tag{2.14}$$

where the coefficients in front of A_1 and B_1 are the expressions for T_{21} and T_{22} respectively.

Note that the A_i's are the coefficients in front of the normalizable solutions in Regions I and II, while the B_i's are the coefficients of the non-normalizable solutions. A wavefunction that is normalizable in Region I (ie, $B_1 = 0$) must also normalizable in Region II ($B_2 = 0$). To ensure this, we set the part of B_2 that depends on A_1 equal to zero: $T_{21} = 0$.

$$\left(-\frac{1}{\lambda} + \frac{iE}{v} \right) - e^{-i\phi} \left(\frac{1}{\lambda} + \frac{iE}{v} \right) = 0$$

$$\lambda = \frac{v}{iE} \frac{e^{i\phi/2} + e^{-i\phi/2}}{e^{i\phi/2} - e^{-i\phi/2}}$$

$$E = \pm M_0 \cos\frac{\phi}{2} \tag{2.15}$$

Eq. 2.15 is the main result of this section and gives the energy of the electron state localized by a change in direction of the magnetization. This result can be substituted into Eqs. 2.7 and 2.10 to find the wavefunctions in each region. They are localized at the origin, with decay length

$$\lambda = \frac{v}{M_0 \sin\frac{\phi}{2}}. \tag{2.16}$$

As a special case, consider the case where the magnetization rotates by π across the interface: $M(x) = M_0 \left[\Theta(x) - \Theta(-x) \right]$. The expressions for the wavefunctions in each region can be combined into the following:

$$\psi_A = e^{-M_0|x|/v} \begin{pmatrix} 1 \\ -i \end{pmatrix} \ , \ \psi_B = e^{+M_0|x|/v} \begin{pmatrix} 1 \\ i \end{pmatrix}. \tag{2.17}$$

We focus on ψ_A since it is the normalizable solution. ψ_A is localized $x = 0$, as expected since this is the location of the discontinuity in $M(x)$. It is also particle-hole symmetric (in this case the particle-hole operator is σ_y, and ψ_A is an eigenvector of σ^y). Therefore the solution is a zero-energy, particle-hole symmetric wavefunction. Eq. 2.16 shows that this is the case where the wavefunction is most localized. As ϕ moves away from π, the energies of the solutions separate away from 0, and the solutions are less well-localized about the origin.

2.2 Superconducting region between Ferromagnetic regions

Now consider the case where a pairing potential is confined to a small region between ferromagnetic material whose magnetization rotates by ϕ across the superconducting region:

$$M(x) = \begin{cases} M_0 e^{i\phi} & , \; x < -L \\ M_0 & , \; x > +L \end{cases}$$

$$\Delta(x) = \begin{cases} \Delta_0 & , \; -L < x < L \\ 0 & , \; otherwise \end{cases}$$

We again start with the expression $H = \frac{1}{2}\Psi^\dagger \mathcal{H}\Psi$, but now the presence of the pair potential means we need a 4-component wavefunction:

$$\Psi = \left(\psi_\uparrow, \psi_\downarrow, \psi_\downarrow^\dagger, -\psi_\uparrow^\dagger\right)^T \tag{2.18a}$$

$$\begin{aligned} \mathcal{H} = &- iv\partial_x \sigma^z \tau^z + \Delta_0 \Theta(x+L)\Theta(-x+L)\tau^x \\ &+ M_0\left[\Theta(x-L) + \cos\phi \; \Theta(-x-L)\right]\sigma^x + M_0 \sin\phi \; \Theta(-x-L)\sigma^y \end{aligned} \tag{2.18b}$$

where τ^i are Pauli matrices that act on the ψ and $\psi^\dagger$ blocks. The solution is independent of the phase of Δ in this geometry, and we set it to zero for simplicity. In the uniform case, the bulk energy gap is given by the smaller of $|M_0 \pm \Delta_0|$. As in the previous section, we solve for the wavefunction in each region and impose continuity to derive the allowed energies.

Region I $(x < -L)$:

$$\mathcal{H} = -iv\partial_x \sigma^z \tau^z + M_0 \cos\phi \; \sigma^x + M_0 \sin\phi \; \sigma^y \tag{2.19}$$

Solutions to $\mathcal{H}\psi = E\psi$ are given by:

$$\psi_{A_1}, \psi_{C_1} = e^{\pm \int_0^x dx'/\lambda}\begin{pmatrix} \frac{iM_0}{v}e^{-i\phi} \\ \mp\frac{1}{\lambda} + \frac{iE}{v} \\ 0 \\ 0 \end{pmatrix}, \quad \psi_{B_1}, \psi_{D_1} = e^{\pm \int_0^x dx'/\lambda}\begin{pmatrix} 0 \\ 0 \\ -\frac{iM_0}{v}e^{-i\phi} \\ \mp\frac{1}{\lambda} - \frac{iE}{v} \end{pmatrix} \tag{2.20}$$

where

$$\lambda \equiv \frac{v}{\sqrt{M_0^2 - E^2}} \; . \tag{2.21}$$

The general solution for the wavefunction in Region I is given by $\psi_I = A_1\psi_{A_1} + B_1\psi_{B_1} + C_1\psi_{C_1} + D_1\psi_{D_1}$. In this section we use the notation that ψ_{A_i} and ψ_{B_i} are the normalizable solutions, while ψ_{C_i} and ψ_{D_i} are not.

Region II $(-L < x < L)$:

$$\mathcal{H} = -iv\partial_x \sigma^z \tau^z + \Delta_0 \tau^x \tag{2.22}$$

Solutions:

$$\psi_{A_2}, \psi_{C_2} = e^{\pm \int_0^x dx'/\Lambda} \begin{pmatrix} 0 \\ \frac{i\Delta_0}{v} \\ 0 \\ \pm\frac{1}{\Lambda} + \frac{iE}{v} \end{pmatrix} \; , \; \psi_{B_2}, \psi_{D_2} = e^{\pm \int_0^x dx'/\Lambda} \begin{pmatrix} -\frac{i\Delta_0}{v} \\ 0 \\ \pm\frac{1}{\Lambda} - \frac{iE}{v} \\ 0 \end{pmatrix} \tag{2.23}$$

where

$$\Lambda \equiv \frac{v}{\sqrt{\Delta_0^2 - E^2}} \; . \tag{2.24}$$

The general solution for the wavefunction in Region II is given by $\psi_{II} = A_2 \psi_{A_2} + B_2 \psi_{B_2} + C_2 \psi_{C_2} + D_2 \psi_{D_2}$.

Region III $(x > L)$:

$$\mathcal{H} = -iv\partial_x \sigma^z \tau^z + M_0 \; \sigma^x \tag{2.25}$$

Solutions:

$$\psi_{A_3}, \psi_{C_3} = e^{\mp \int_0^x dx'/\lambda} \begin{pmatrix} \frac{iM_0}{v} \\ \pm\frac{1}{\lambda} + \frac{iE}{v} \\ 0 \\ 0 \end{pmatrix} \; , \; \psi_{B_3}, \psi_{D_3} = e^{\mp \int_0^x dx'/\lambda} \begin{pmatrix} 0 \\ 0 \\ -\frac{iM_0}{v} \\ \pm\frac{1}{\lambda} - \frac{iE}{v} \end{pmatrix} \tag{2.26}$$

The general solution for the wavefunction in Region III is given by $\psi_{III} = A_3 \psi_{A_3} + B_3 \psi_{B_3} + C_3 \psi_{C_3} + D_3 \psi_{D_3}$.

Matching solutions at each interface We impose continuity on the wavefunctions at each interface to obtain T_1 and T_2, defined as follows:

$$\begin{pmatrix} A_3 \\ B_3 \\ C_3 \\ D_3 \end{pmatrix} = T_2 \begin{pmatrix} A_2 \\ B_2 \\ C_2 \\ D_2 \end{pmatrix} = T_1 T_2 \begin{pmatrix} A_1 \\ B_1 \\ C_1 \\ D_1 \end{pmatrix} \tag{2.27}$$

Note that A_i and B_i are the coefficients in front of the normalizable solutions in Regions I and III, while C_i and D_i are coefficients of the non-normalizable solutions. The following restriction, that a wavefunction that is normalizable in Region I must also be normalizable in Region III, leads to a quantization condition on the energy. This condition is equivalent to setting the determinant of the lower left 2×2 submatrix of $T_1 T_2$ to 0. The algebra to solve for T_1 and T_2 is similar to the FM-FM case, so we won't give the full expressions here. The condition becomes

$$e^{i\phi} \left[e^{-4L/\Lambda} \left(\frac{1}{\lambda} - \frac{1}{\Lambda}\right)^2 + e^{4L/\Lambda} \left(\frac{1}{\lambda} + \frac{1}{\Lambda}\right)^2 \right] E^2$$

$$= \frac{1}{\Lambda^2} \left(E^2 + \frac{v^2}{\lambda^2}\right)(1 + e^{2i\phi}) + 2e^{i\phi}\frac{1}{\lambda^2}\left(E^2 + \frac{v^2}{\Lambda^2}\right) \tag{2.28}$$

The full solution to Eq. 2.28 is too complicated to solve analytically, so we settle for an approximation. We are interested in low-energy excitations located well inside the bulk energy gap, so the energies can be restricted to $E \ll M_0, \Delta_0$. These energies arise as the splitting due to weakly interacting Majorana states, which must be widely separated in order for the energies to be small. Therefore we make the additional approximation that $L \gg \frac{v}{\Delta_0}$. With these simplifications, Eq. 2.28 becomes

$$e^{i\phi}e^{4L\Delta_0/v}(M_0 + \Delta_0)^2 E^2 = \Delta_0^2 M_0^2 \left(1 + e^{2i\phi}\right) + 2e^{i\phi}M_0^2\Delta_0^2$$

$$E = \pm 2e^{-2L\Delta_0/v}\frac{M_0\Delta_0}{M_0 + \Delta_0}\cos\frac{\phi}{2} \tag{2.29}$$

The penetration depth into the FM regions is given by $\lambda = \frac{v}{M_0 \sin\phi/2}$, again indicating that the best-localized wavefunctions are in systems where the phase changes by π.

Let us examine the special case when $\phi = \pi$ further. The normalizable solutions are given by

$$\psi_1 = e^{+\int_0^x dx' \Delta(x')/v - \frac{M_0}{v}|x|}\begin{pmatrix} -1 \\ i \\ -i \\ 1 \end{pmatrix} \ , \ \psi_2 = e^{-\int_0^x dx' \Delta(x')/v - \frac{M_0}{v}|x|}\begin{pmatrix} i \\ 1 \\ 1 \\ i \end{pmatrix} \tag{2.30}$$

ψ_1 is localized at $x = L$, while ψ_2 is localized at $x = -L$. They also satisfy particle-hole symmetry: $\kappa\psi_1 = \psi_1, \kappa\psi_2 = \psi_2$.

To study the Majorana nature of these solutions, we first construct the corresponding field operators, $\Gamma_i = \Psi^\dagger\psi_i$. Because of the redundancy in the way we expressed Ψ, $\Gamma_{-E} = \Gamma_E^\dagger$. Note that both states satisfy $\Gamma_i^\dagger = \Gamma_i$, so these are Majorana states. We have found that coupling QSH edge states to an SC region between two FM regions with opposite magnetization leads to two mid-gap Majorana fermions. Comparing this result to the electron solution found in the previous section, the effect of the SC region is to split the zero-energy electron mode into two Majorana modes with exponentially suppressed energies.

2.3 Hamiltonian of the chain

To write the Hamiltonian for the Majorana chain, we also need the effective interaction for Majorana modes separated by an FM region, *ie* the SC-FM-SC geometry. However this is easily obtained from the result for the FM-SC-FM geometry using a duality property of the Hamiltonian [65]. If we allow for the pair potential term to have an arbitrary phase, then the Hamiltonian can be written in a more symmetric way:

$$\mathcal{H} = -iv\partial_x\sigma^z\tau^z + \vec{\Delta}(x)\cdot\vec{\tau} + \vec{M}(x)\cdot\vec{\sigma} \tag{2.31}$$

where $\vec{M}(x) = (M_0\cos\phi_m, M_0\sin\phi_m, 0)$ and $\vec{\Delta}(x) = (\Delta_0\cos\phi_s, \Delta_0\sin\phi_s, 0)$. The form of Eq. 2.31 shows that the excitation energies have the same form when $\vec{M}(x)$ and $\vec{\Delta}(x)$ are

$$\underset{\gamma_1}{\bigcirc} \xrightarrow[\varepsilon_{12}]{M_0 e^{i\phi_1}} \underset{\gamma_2}{\bigcirc} \xrightarrow[\varepsilon_{23}]{\Delta_0 e^{i\phi_2}} \underset{\gamma_3}{\bigcirc} \xrightarrow[\varepsilon_{34}]{M_0 e^{i\phi_3}} \underset{\gamma_4}{\bigcirc} \xrightarrow[\varepsilon_{45}]{\Delta_0 e^{i\phi_4}} \underset{\gamma_5}{\bigcirc} \xrightarrow[\varepsilon_{56}]{M_0 e^{i\phi_5}} \underset{\gamma_6}{\bigcirc}$$
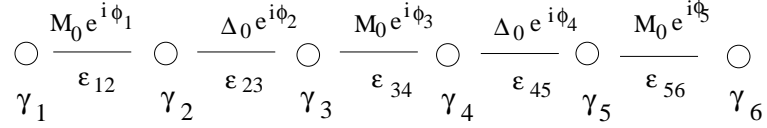
Figure 2.1: Nearest-neighbor interactions of the Majorana chain. The value of $t_{2j-1,2j}$ is determined by the phases of the SC regions and the sizes of the FM regions, and vice versa for $t_{2j,2j+1}$.

exchanged. The hybridization energy can be written so that it captures SC-FM-SC as well as FM-SC-FM pairs:

$$t_{i,i+1} = 2e^{-2L/\ell_i} \frac{M_0 \Delta_0}{M_0 + \Delta_0} \cos \frac{\Delta\phi_i}{2} \tag{2.32}$$

with $\Delta\phi_i = \phi_{m_i} - \phi_{m_{i+2}}$ and $\ell_i = v/\Delta_0$ describing a FM-SC-FM sequence, and $\Delta\phi_{2j} = \phi_{s_i} - \phi_{s_{i+2}}$ and $\ell_i = v/M_0$ describing a SC-FM-SC sequence.

Since the interaction between Majorana fermions decays exponentially with the distance, we keep only the nearest-neighbor interactions, so the Hamiltonian of the chain is

$$H = i \sum_i t_{i,i+i} \ \gamma_i \gamma_{i+1}. \tag{2.33}$$

In the numbering convention shown in Fig. 2.1, γ_{2j-1} and γ_{2j} are separated by an FM region, while γ_{2j} and γ_{2j+1} are separated by an SC region. The interactions $t_{2j-1,2j}$ ($t_{2j,2j+1}$) are related to the length of the FM (SC) regions and the phases of the pair potentials (magnetizations) in the SC (FM) regions.

Chapter 3

Mapping to the Transverse-Field Ising Model

In this chapter we study the critical properties of the Majorana fermion chain, Eq. 2.33, by mapping it to the transverse-field Ising spin chain [13]. An exact mapping between Majorana operators, which obey anticommutation relations, and spin-1/2 operators, which obey commutation relations, is possible in 1D. However, the transformation takes the form of string operators that make the relation highly non-local. In this chapter, we review a real space renormalization group (RSRG) that was developed to study the random quantum spin chain and generalize it to study the properties of the random Majorana chain.

The Jordan-Wigner transformation maps the fermion operators to spin operators:

$$\gamma_{2j-1} = \sigma_j^x \sum_{k=1}^{j-1} \sigma_k^z, \quad \gamma_{2j} = \sigma_j^y \sum_{k=1}^{j-1} \sigma_k^z \tag{3.1}$$

where σ^α are Pauli matrices that obey the usual commutation relations $[\sigma_j^\alpha, \sigma_j^\beta] = i\epsilon^{\alpha\beta\gamma}\sigma_j^\gamma$. Applying this transformation to Eq. 2.33, and renaming the interactions $t_{2j-1,2j} \equiv h_j$ and $t_{2j,2j+1} \equiv J_j$, we obtain the Hamiltonian for the transverse-field Ising spin chain:

$$H = -\sum_j h_j \sigma_j^z + J_j \sigma_j^x \sigma_{j+1}^x \tag{3.2}$$

In the uniform case, $h_j \equiv h$ and $J_j \equiv J$, this system has a quantum critical point at $h = J$. Therefore the Majorana fermion chain also has a critical point when all the pairwise interactions $t_{2j-1,2j}$ and $t_{2j,2j+1}$ are equal. The uniform Majorana chain can be realized by requiring all the FM and SC regions be the same size and all second-neighbor FM and SC regions to have the same relative phase. Such excessive tuning of the FM and SC regions to reach the uniform critical point does not seem realistic, and we turn now to the non-uniform case.

3.1 Random Transverse Field Ising Model

In the random case, the values of h_j and J_j vary along the chain and occur with some probability distributions $P(J)$ and $R(h)$. The difficulty in studying such random systems analytically is that physical quantities such as the magnetization and spin-spin correlations do not converge to a single value, but rather occur with some probability distribution. Rare anomalous events may occur with very small probability and yet dominate disorder-averaged quantities. A systematic way to study the rare anomalous events that occur at low energy is a real-space RG method [20] developed for the transverse-field Ising model by Fisher [24]. Each step of this method consists of decimating the highest energy term in the Hamiltonian and replacing it with effective interactions of longer range.

3.1.1 Decimation of the Highest-Energy Term

For the random transverse-field Ising model, this prescription results in forming a ferromagnetic cluster if the strongest interaction is a bond J_j or decimating a spin if it is a field h_j. For example, if the largest energy is the field at site 2, h_2, we make the approximation that the spin at site 2 remains frozen in the ground state of the h_2 term of the Hamiltonian. To first order, quantum fluctuations through the exchange interactions with neighboring spins have the effect of flipping the spin at site 2 and can be neglected. To second order, however, two successive spin-flips can leave spin 2 in its ground state while introducing an effective interaction between spins 1 and 3. A second-order perturbation theory calculation gives the new exchange term

$$J_{13} = \frac{J_{12}J_{23}}{2h_2},\tag{3.3}$$

which is smaller than J_{12} or J_{23}. Thus the effect of the RG step is to replace spin 2's interactions with its neighbors by a weaker second-neighbor interaction and then decimate the spin at site 2. If the largest energy is the bond between sites 1 and 2, a similar process results in spins 1 and 2 frozen together in a ferromagnetic cluster with effective field $\tilde{h} = \frac{h_1 h_2}{2J_{12}}$.

These recursion relations can also be derived for decimation of Majorana pairs. We write the Hamiltonian of the Majorana chain in the following away:

$$H = \sum_j ih_j \ \gamma_{2j-1}\gamma_{2j} + iJ_j \ \gamma_{2j}\gamma_{2j+1}\tag{3.4}$$

Decimating Across Different Dirac fermions
We first find the effective Hamiltonian when the decimated term connects an even to an odd Majorana: $\Omega = J_2$. It is intuitively easier to convert the Majorana operators into Dirac operators via $c_j = \gamma_{2j-1} + i\gamma_{2j}$.

$$\begin{aligned} H_0 &= iJ_2 \ \gamma_4\gamma_5 \\ &= J_2(c_2c_3 + c_2c_3^\dagger - c_2^\dagger c_3 - c_2^\dagger c_3^\dagger) \end{aligned}\tag{3.5}$$
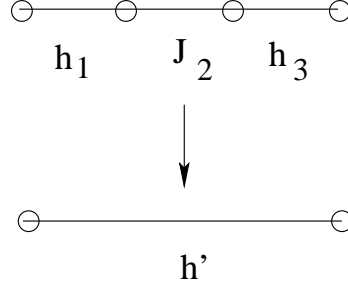
Figure 3.1: Decimation of the term connecting Majoranas forming different Dirac fermions.

In terms of electron operators, the term consists of hopping and pairing between nearest neighbors. The ground state of Eq. 3.5 is doubly degenerate, and the two states can be written in terms of the electron/hole vacuum, $|0\rangle$.

$$|s_1\rangle = c_2^\dagger|0\rangle + c_3^\dagger|0\rangle \tag{3.6a}$$

$$|s_2\rangle = |0\rangle - c_3^\dagger c_2^\dagger|0\rangle \tag{3.6b}$$

with ground state energy $E_s = -J_2$. We can simplify the notation in Eqs. 3.6a-3.6b by writing the solutions in terms of the electron occupation number at sites 2 and 3: $|s_1\rangle = |10\rangle + |01\rangle$ and $|s_2\rangle = |00\rangle - |11\rangle$. Note that $|s_1\rangle$ and $|s_2\rangle$ have odd and even fermion parity respectively.

The first excited states of Eq. 3.5 are similarly given by

$$|t_1\rangle = -c_2^\dagger|0\rangle + c_3^\dagger|0\rangle \tag{3.7a}$$

$$|t_2\rangle = |0\rangle + c_3^\dagger c_2^\dagger|0\rangle \tag{3.7b}$$

In terms of electron occupation number, the first excited states are:$|t_1\rangle = -|10\rangle + |01\rangle$ and $|t_2\rangle = |00\rangle + |11\rangle$, with $E_t = +J_2$. We now examine the effects of H_1, the term that connects the decimated Majorana pair to its nearest neighbors:

$$H_1 = ih_2\gamma_2^L\gamma_2^R + ih_3\gamma_3^L\gamma_3^R \tag{3.8}$$

To leading order, H_1 moves the system from a ground state into a first excited state:

$$H_1|s_1\rangle = h_2(|10\rangle - |01\rangle) + h_3(-|10\rangle - |01\rangle) = (h_3 - h_2)|t_1\rangle \tag{3.9}$$

$$H_1|s_2\rangle = h_2(-|00\rangle - |01\rangle) + h_3(-|10\rangle - |01\rangle) = -(h_2 + h_3)|t_2\rangle \tag{3.10}$$

In a perturbative expansion in terms of h_2/J_2 and h_3/J_2, the first order-terms thus vanish. The second-order terms, however, are given by

$$H_{\alpha\beta}^{eff} = \sum_i \frac{\langle s_\alpha|H_1|t_i\rangle\langle t_i|H_1|s_\beta\rangle}{E_s - E_t} \tag{3.11}$$

In the basis of $|s_1\rangle$ and $|s_2\rangle$, the effective coupling term becomes

$$H^{eff} = -\frac{1}{2J_2}\begin{pmatrix} (h_2 - h_3)^2 & 0 \\ 0 & (h_2 + h_3)^2 \end{pmatrix} \tag{3.12}$$

The effective coupling treats the even-parity and odd-parity states differently. In terms of second-quantized operators, Eq. 3.12 can be written as

$$\begin{aligned} H^{eff} &= -\frac{h_2^2 + h_3^2}{2J_2} + \frac{h_2 h_3}{J_2}(2\tilde{c}^\dagger \tilde{c} - 1) \\ &= -\frac{h_2^2 + h_3^2}{2J_2} + i\frac{h_2 h_3}{J_2}\gamma_3\gamma_6 \end{aligned} \tag{3.13}$$

where we define $\tilde{c} = \gamma_3 + i\gamma_6$. The decimation has induced an interaction between the Majoranas at sites 3 and 6; however these are now nearest neighbors in terms of active Majoranas remaining in the chain. The RSRG process thus preserves the form of the original Hamiltonian with couplings only between nearest neighbors. The first term in Eq. 3.13 represents a small shift in the overall ground state energy, which we can neglect.

Decimating within a Dirac fermion

We now consider a decimation of the other kind, when the the two Majoranas in question belong to the same Dirac fermion: $\Omega = h_2$.
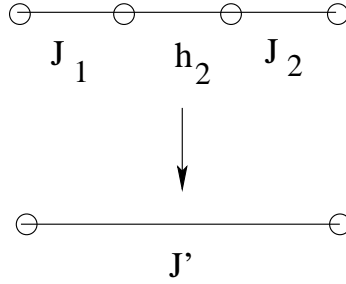
Figure 3.2: Decimation of the term connecting Majoranas from the same Dirac fermion.

$$\begin{aligned} H_0 &= ih_2\ \gamma_3\gamma_4 \\ &= h_2(2c_2^\dagger c_2 - 1) \end{aligned} \tag{3.14}$$

The ground state is 4-fold degenerate, and we again express the states in terms of the electron occupation number at each site. But first, it is helpful to define the following states:

$$|d_1\rangle = |0_1 0_3\rangle \quad , \quad |d_2\rangle = |0_1 1_3\rangle \tag{3.15a}$$

$$|d_3\rangle = |1_1 0_3\rangle \quad , \quad |d_4\rangle = |1_1 1_3\rangle \tag{3.15b}$$

where $|1_1 1_3\rangle = c_3^\dagger c_1^\dagger |0\rangle$, by convention. The ground states are then $|s_i\rangle = |0_2\rangle \times |d_i\rangle$ with energy $E_s = -h_2$. The first excited states are given by $|t_i\rangle = |1_2\rangle \times |d_i\rangle$ with $E_t = +h_2$.

The terms connecting the decimated Majoranas with their nearest neighbors are

$$H_1 = iJ_1\gamma_2\gamma_3 + iJ_2\gamma_4\gamma_5 \tag{3.16}$$

By calculating the effect of Eq. 3.16 on the ground state manifold, we can again find the effective coupling induced by decimating this pair:

$$H^{eff} = \frac{1}{h_2}\begin{pmatrix} -(J_1^2 + J_2^2)/2 & 0 & 0 & J_1 J_2 \\ 0 & -(J_1^2 + J_2^2)/2 & J_1 J_2 & 0 \\ 0 & J_1 J_2 & -(J_1^2 + J_2^2)/2 & 0 \\ J_1 J_2 & 0 & 0 & -(J_1^2 + J_2^2)/2 \end{pmatrix} \tag{3.17}$$

$$
\begin{aligned}
H^{eff} &= -\frac{J_1^2 + J_2^2}{2h_2}\mathcal{I} + \frac{J_1 J_2}{h_2}(c_1 c_3 - c_1^\dagger c_3^\dagger) + \frac{J_1 J_2}{h_2}(c_1 c_3^\dagger - c_1^\dagger c_3) \\
&= -\frac{J_1^2 + J_2^2}{2h_2} + i\frac{J_1 J_2}{h_2}\,\gamma_2\gamma_5. \tag{3.18}
\end{aligned}
$$

In this case, Majoranas 3 and 4 are decimating, inducing a new effective coupling between Majoranas 2 and 5.

3.1.2 Infinite Randomness Fixed Point

Applying the RG many times lowers the energy of the spin chain and creates exchange couplings and spin clusters spanning longer and longer distances. It has been shown [24] that the presence of disorder in the initial system causes the distributions to flow to the "infinite-randomness fixed point." Let Ω be the strongest coupling term in the chain at a given point in the RSRG. We can define a flow parameter for the RG process $\Gamma = \ln\Omega_I/\Omega$, where Ω_I is the strongest term in the original chain. Note that $\Gamma = 0$ at the beginning of the RG flow and increases as the strongest term in the chain is lowered. It is also useful to work in logarithmic energies, $\zeta_i = \ln\Omega/E_i$. The critical point was shown to occur when the probabilities are both equal to the infinitely broad random distribution:

$$P(\zeta) = R(\zeta) = \frac{1}{\Gamma}e^{-\zeta/\Gamma} \tag{3.19}$$

The ground state of the critical random transverse-field Ising spin chain has ferromagnetic clusters of all length scales, similar to the random-singlet phase of the Heisenberg spin chain. In terms of fermion operators, this means that the Majorana fermion chain is critical when the interactions $t_{2j-1,2j}$ and $t_{2j,2j+1}$ are drawn from essentially the same infinitely broad random distribution, with Majorana fermions coupled in pairs of all length scales.

3.2 Self-duality

Before looking at the robustness of the disordered critical point, we first discuss the importance of the pairing convention used to map the Majorana fermions to spins in Eq. 3.1. As shown in Fig. 3.3, there are two ways to group the Majorana fermions into
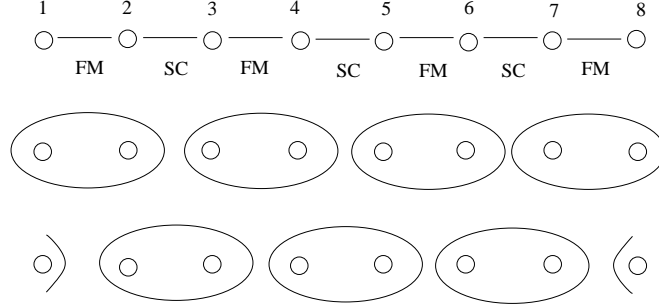
Figure 3.3: The Majorana fermions can be paired to form spins in two inequivalent ways: a given fermion can be either the left or right member of a pair. The duality of the transverse-field Ising model ensures that the physical properties of the system are independent of the pairing convention chosen.

pairs. The middle line corresponds to the convention chosen in Eq. 3.1; in the resulting spin chain, the values of $h_j(J_j)$ are determined by the phases of the SC (FM) regions. The lower line in Fig. 3.3 shows the other possible pairing convention,

$$\gamma_{2j} = \tau_j^x \sum_{k=1}^{j-1} \tau_k^z \ , \ \ \gamma_{2j+1} = \tau_j^y \sum_{k=1}^{j-1} \tau_k^z \tag{3.20}$$

where we write the Pauli matrices as τ^α to keep them distinct from the σ^α used above. Here the h_j's (J_j's) are determined the FM (SC) regions. Switching pairing conventions seemingly switches the spin chain from the paramagnetic phase to the ferromagnetic phase and vice versa.

The choice of how to pair the Majorana fermions is only a mathematical convention made in order to implement the Jordan-Wigner transformation, and the physical properties of the resulting spin chain should be independent of how the mapping is performed. The apparent unphysical consequence of the mapping is resolved by considering the duality properties of the transverse-field Ising chain. The system has the same properties when the roles of h and J are exchanged and spins are replaced by domain wall variables simultaneously. In the transformations given above, if we consider σ_j^α to be spin variables, then the τ_j^α's are domain wall variables. This can be shown, for example, by the following non-local duality transformation relating the two: $\sigma_j^x = \prod_{k<j} \tau_k^z$, $\sigma_j^z = \tau_{j-1}^x \tau_j^x$. Thus the two pairing conventions are related by switching spins/domain walls and values of h_j/J_j, which leads to two representations of the same system.

In addition to resolving the self-consistency problem of the fermion-to-spin mapping, this behavior also provides insight into the duality property of the original QSH edge with respect to the FM and SC regions. The properties of these regions enter the spin chain as h_j and J_j, and the duality of the transverse-field Ising model is translated to the Majorana chain as a duality under interchange of the FM and SC regions.

3.3 Critical point at $\delta = 0$

Now we consider the robustness of the infinite-randomness fixed point. To realize this critical point, the probability distributions of $\epsilon_{2j-1,2j}$ and $\epsilon_{2j,2j+1}$ must both be equal to the infinitely broad random distribution. Constructing FM and SC regions at the QSH edge to satisfy this condition – although not as stringent as for the uniform critical point – is still difficult as it restricts the forms of both distributions. A weaker condition for criticality parameterizes the distance to the critical point by

$$\delta = \frac{\overline{lnh} \; - \; \overline{lnJ}}{var(ln\ h) + var(ln\ J)}.$$
(3.21)

where the bar denotes averaging. Now the critical point, given by $\delta = 0$, occurs whenever the two distributions have the same log-average. In particular, given any distribution for say h_j, one can tune the system through the critical point by adjusting the distribution for J_j. The Majorana chain can be made critical for any distribution of the SC regions by tuning the FM regions to $\delta = 0$ or vice versa.

3.4 Robust to Coulomb repulsion

Another potential difficulty to realizing the critical point is Coulomb repulsion between fermions. While the Majorana fermions themselves are charge-neutral, two neighboring Majorana fermions can combine to form a Dirac fermion that has charge. We model the short-range Coulomb repulsion between two neighboring Dirac fermions as

$$H^{(2)} = \sum_j J^{(2)} \gamma_{2j} \gamma_{2j+1} \gamma_{2j+2} \gamma_{2j+3}.$$
(3.22)

Under the Jordan-Wigner transformation, Eq. 3.22 is mapped to a second-neighbor spin interaction

$$H^{(2)} = -\sum_j J^{(2)} \sigma_j^x \sigma_{j+2}^x.$$
(3.23)

The interaction term could also have been written as $\tilde{J}^{(2)} \gamma_{2j-1} \gamma_{2j} \gamma_{2j+1} \gamma_{2j+2}$, which corresponds to the second way to group four neighboring Majorana fermions for a given pairing convention. This term maps to $\tilde{J}^{(2)} \sigma_j^z \sigma_{j+1}^z$, which under a duality transformation goes to Eq. 3.23. Using the real-space RG methods outlined above, Eq. 3.23 was shown to be an irrelevant perturbation to the disordered critical point [16]. Thus the presence of short-range Coulomb repulsion between Dirac fermions arising from combinations of Majorana degrees of freedom does not affect the critical properties of the Majorana chain.

Chapter 4

The RSRG as Unitary Transformations

The effect of the RSRG on the Majorana chain, by design, is to reduce the chain to a set of decoupled pairs. However the density of states and transport quantities are measured by coupling the chain to an STM leads biased at voltage V relative to the chain. The combined Hamiltonian for the Majorana chain and a probing tip coupled to one end is:

$$H = -i\sum_{i=1}^{\infty} t_{i,i+1}\gamma_i\gamma_{i+1} + it_0\gamma_1\left(\psi^\dagger e^{-ieVt/\hbar} + \psi e^{ieVt/\hbar}\right) \tag{4.1}$$

where ψ is the annihilation operator of tip electrons [11]. We already know how the first term in Eq. 4.1 transforms under successive transformation; in this chapter, we derive what happens to the second term that describes the coupling of the chain at one end to the STM tip.

4.1 Unitary Transformations

We will use the RSRG to reduce the semi-infinite chain and STM to a problem of a tip interacting with independent Majorana pairs:

$$H_{eff} \approx -i\sum_{n=1}^{\infty} \left[a_n\gamma_{n,a}\left(\psi^\dagger e^{-ieVt/\hbar} + \psi e^{ieVt/\hbar}\right) + \epsilon_n\gamma_{n,a}\gamma_{n,b}\right]. \tag{4.2}$$

The decoupled Majorana pairs correspond to the so-called random-singlets formation that was investigated in random Heisenberg chains [23] and in random hopping fermions [42]. The $I - V$ characteristics of this Hamiltonian are as follows: whenever the voltage of the tip is at resonance with $\pm\epsilon_n$ a step appears in the $I - V$ curve, with an amplitude proportional to the tunneling rate, a_n^2:

$$\frac{dI}{dV} \sim \sum_n a_n^2 \left[\delta(eV + \epsilon_n) - \delta(eV - \epsilon_n)\right]. \tag{4.3}$$

The two opposite sign delta-functions are due to the special coupling term $\propto \psi + \psi^\dagger$; if at a positive resonance, $V = |\epsilon_n|$, ψ is responsible for a current flowing *into* the chain, and when $V = -|\epsilon_n|$, $\psi^\dagger$ will produce the current, which flows *out of* the chain to the tip.

The measured LDOS, Eq. (4.3), will provide not only the chain's density of states, but also the probe's overlap a_n with the edge Majorana. Therefore it reveals both the energy and spatial structure of the random Majorana chain. We can find both the energy levels ϵ_n and the edge overlap, a_n using the RSRG method applied as a series of unitary transformations on Eq. 4.1 [73]. This method has two main advantages: it allows us to keep track of the evolution of other operators, and provides a straightforward way to reconstruct the ground-state wave function.

Consider a Hamiltonian $\mathcal{H}$ with ground-state solution $|\psi\rangle$ and energy E_0: $\mathcal{H}|\psi\rangle = E_0|\psi\rangle$. For the Majorana chain or random transverse-field Ising model, $|\psi\rangle$ will be a complicated many-body wave function. We can make progress towards simplifying the solution by applying a unitary transformation that decouples the strongest term from the rest of the chain: $e^{iS}\mathcal{H}e^{-iS}\left(e^{iS}|\psi\rangle\right) = E_0\left(e^{iS}|\psi\rangle\right)$. The transformed Hamiltonian and wave function can be written as

$$\tilde{\mathcal{H}} = e^{iS}\mathcal{H}e^{-iS} \tag{4.4a}$$

$$|\psi_{eff}\rangle = e^{iS}|\psi\rangle \tag{4.4b}$$

Many successive unitary transformations leave the chain in a state whose ground state wavefunction we can write down simply: it is the product of many spin singlets. The ground state of the original Hamiltonian can be recovered by applying the inverse transformations, in reverse order, to the product state. The effective form of other operators is similarly found by applying the unitary transformations: $\tilde{A} = e^{iS}Ae^{-iS}$.

It will be helpful to decompose the Hamiltonian into three parts: $\mathcal{H} = H_0 + V' + H_1$. Let H_0 be the largest-energy term that will be decimated. V' consists of the terms that connect the decimated Majorana pair to the rest of the chain. H_1 describes the remainder of the chain, which should be left unchanged by this step. The unitary transformation becomes

$$\tilde{\mathcal{H}} = e^{iS}\mathcal{H}e^{-iS} = e^{iS}\left(H_0 + V' + H_1\right)e^{-iS}$$
$$= H_0 + V' + H_1 + i\left[S, H_0 + V' + H_1\right] - \frac{1}{2}\left[S, [S, H_0]\right] \tag{4.5}$$

where we have only kept terms up to $O(S^2)$. An appropriate generator S can be chosen so that the first-order terms cancel out: $i[S, H_0] = -V'$. The second term in the commutator will give the new effective bond created between the nearest neighbors of the decimated pair, as well as a shift in the ground state energy due to integrating out the decimated pair. The third term in the commutator introduces a longer-ranged interaction involving one of the decimated Majoranas. However this new interaction term can be eliminated by applying an additional unitary transformation simultaneously. We give a detailed calculation of the generators of these transformations below.

4.2 Generators of the Unitary Transformations

As an example, we find the generators for the decimation of the Majorana pair connected by h_1, ie $H_0 = ih_1\gamma_1\gamma_2$. The generators for the decimation of $J_2\gamma_2\gamma_3$ follow analogously. The terms connecting this pair to the rest of the chain are $V' = iJ_0\gamma_0\gamma_1 + iJ_2\gamma_2\gamma_3$. These are the nearest-neighbor terms that will be canceled as a result of the unitary transformation. Consider the generator

$$S_a^{(1)} = i\frac{J_0}{2h_1}\gamma_2\gamma_0 + i\frac{J_2}{2h_1}\gamma_1\gamma_3. \tag{4.6}$$

It is straight-forward to show that $i[S_a^{(1)}, H_0] = -V'$, so that after the transformation, the Hamiltonian does not contain terms connecting the decimated pair to its nearest neighbors. The second term of the commutator in Eq. 4.5 gives

$$i[S_a^{(1)}, V'] = i\frac{J_0^2 + J_2^2}{2h_1}\gamma_1\gamma_2 + i\frac{J_0 J_2}{h_1}\gamma_0\gamma_3. \tag{4.7}$$

The first term in Eq. 4.7 represents a small shift in the ground state energy, while the second term is the new effective interaction between the nearest neighbors of the decimated Majoranas. Since h_1 is the strongest term in the chain, the effective interaction $\tilde{J} = \frac{J_0 J_2}{h_1}$ is weaker than any of the three eliminated terms J_0, h_1, or J_2.

We now turn to the final term of commutator in Eq. 4.5. The only non-zero contributions come from the second-nearest neighbors of the decimated pair:

$$i[S_a^{(1)}, H_1] = -i\frac{J_0 h_{-1}}{2h_1}\gamma_{-1}\gamma_2 - i\frac{J_2 h_3}{2h_1}\gamma_1\gamma_4 \equiv V''. \tag{4.8}$$

Although the transformation decouples Majoranas 1 and 2 from their nearest neighbors, Eq. 4.8 shows that it also introduces new interactions connecting them to their third-neighbors. This interaction can be eliminated by applying a second unitary transformation $S_b^{(2)}$ such that $i[S_b^{(2)}, H_0] = -V''$. This can be done using the generator

$$S_b^{(2)} = i\frac{J_0 h_{-1}}{2h_1^2}\gamma_1\gamma_{-1} + i\frac{J_2 h_3}{2h_1^2}\gamma_2\gamma_4. \tag{4.9}$$

The transformation generated by $S_b^{(2)}$ will also introduce a new type of long-range interaction which we have to eliminate via $S_a^{(3)} = i\frac{J_0 h_{-1} J_{-2}}{2h_1^3}\gamma_2\gamma_{-2} + i\frac{J_2 h_3 J_4}{2h_1^3}\gamma_1\gamma_5$, which in turn necessitates $S_b^{(4)}$, and so on. Briefly, S_a-type generators connect γ_1 to odd-numbered Majoranas in a way that straddles the decimated pair, while S_b-type generators do not straddle the decimated pair.

For the decimation of a general term $iE_j\gamma_j\gamma_{j+1}$, the full expressions for generators of arbitrary order are given by

$$S_a^{(2n-1)} = \frac{i}{2}\left(\prod_{k=j+1-2n}^{k=j-1}\frac{E_k}{E_j}\right)\gamma_{j+1}\gamma_{j+1-2n}$$

$$+ \frac{i}{2}\left(\prod_{k=j+1}^{j-1+2n}\frac{E_k}{E_j}\right)\gamma_j\gamma_{j+2n} \tag{4.10a}$$

$$S_b^{(2n)} = \frac{i}{2} \left(\prod_{k=j-2n}^{k=j-1} \frac{E_k}{E_j} \right) \gamma_j \gamma_{j-2n}$$

$$+ \frac{i}{2} \left(\prod_{k=j+1}^{2n+j} \frac{E_k}{E_j} \right) \gamma_{j+1} \gamma_{j+1+2n} \tag{4.10b}$$

where E_k is the coupling between Majoranas k and $k+1$. The superscript on $S^{(m)}$ indicates that the generator is of order m in $\frac{E_k}{h_1}$.

4.3 Effective Coupling Term

We are now ready to calculate the effect of a unitary transformation, with generators given by Eqs. 4.10a-4.10b, on the Majorana coupled to the probe, Eq. 4.1:

$$\tilde{\gamma}_1 = e^{iS} \gamma_1 e^{-iS}$$

$$= \gamma_1 + i[S, \gamma_1] - \frac{1}{2}[S, [S, \gamma_1]] \tag{4.11}$$

$$S = \sum_n S_a^{(2n-1)} + S_b^{(2n)} \tag{4.12}$$

The edge Majorana operator will be transformed to a linear combination of odd-numbered Majorana operators, with coefficients that in general decrease with distance from the edge.

Before writing expressions for the evolution of the coefficients, let us look at how the decimation proceeds. In a typical chain, the first decimation will most likely be in the bulk, say J_j. At this point, the only Majorana connected to the probe is γ_1. According to Eq. 4.11, a change in the coupling coefficients is caused by generators that don't commute with γ_1, ie those that contain γ_1. The transformation that eliminates J_j has generators that connect γ_j or γ_{j+1} to the rest of the chain. Therefore there is only one generator we need to worry about: the one between γ_{j+1} and γ_1. The edge Majorana transforms as

$$\gamma_1 \to \gamma_1 + \left(\prod_{k=1}^{j-1} \frac{E_k}{J_j} \right) \gamma_{j+1} \tag{4.13}$$

The probe is now coupled to γ_{j+1} as well as to the edge, but γ_{j+1} is part of the decimated Majorana pair and drops out of the chain. Its coupling coefficient remains the same as the RG proceeds. The same story holds for successive bulk decimations: the probe becomes coupled to a bulk Majorana that then drops out of the chain.

Things become complex when the decimated Majorana is the one on the edge. All orders of generators of this decimation contain a Majorana coupled to the probe (in this case, the edge Majorana). So the transformed edge Majorana will contain terms from all the bulk Majoranas, though the coefficients for Majoranas farther away are higher in order:

$$\gamma_1 \to \gamma_1 + \sum_{n=2}^{N} \left(\prod_{k}^{2n-2} \frac{E_k}{h_1} \right) \gamma_{2n-1} \tag{4.14}$$

After the decimation, γ_1 drops out of the chain, leaving the probe coupled to all odd-numbered Majoranas. For subsequent decimations, we have to consider the commutations of the generators with every odd-numbered Majorana.

We now examine how the coupling coefficients change under a generic decimation of the term E_j. Assuming there has already been at least one edge decimation, the probe is coupled to all odd-numbered Majoranas:

$$\tilde{\gamma}_1 = \sum_{i\ odd} a_i \gamma_i. \tag{4.15}$$

Substituting Eq. 4.15 for γ_1 into Eq. 4.11 gives the effective coupling coefficients.

$$i < j: \ \tilde{a}_i = a_i + a_j \prod_{k=i}^{j-1} \frac{E_k}{E_j} \tag{4.16a}$$

$$i = j: \ \tilde{a}_j = a_j + \sum_{i<j} a_i \left(\prod_{k=i}^{j-1} \frac{E_k}{E_j} \right)$$
$$+ \sum_{i>j} a_i \left(\prod_{k=j+1}^{i-1} \frac{E_k}{E_j} \right) \tag{4.16b}$$

$$i > j: \ \tilde{a}_i = a_i + a_j \prod_{k=j+1}^{i-1} \frac{E_k}{E_j} \tag{4.16c}$$

When j is odd (*ie*, the decimated energy is h_j), γ_j picks up some complicated factor and drops out of the chain. All the other odd-numbered Majoranas pick up a simpler factor, and we must keep following their evolution. If j is even, it is γ_{j+1} (the odd-numbered member of the decimated pair) that picks up a complicated coupling coefficient.

Chapter 5

Single Lead: Energy Levels and Coupling

In this chapter, we consider a semi-infinite Majorana chain coupled to an STM probe at one end. As shown in the previous chapter, at low energies the Majorana chain decouples into a series of Majorana pairs, each of which is coupled to the probe. We compute the joint probability distribution for a Majorana pair to have energy splitting E_M and coupling to the probe a. The main result is that the tunneling dI/dV has strong spikes corresponding to decimations of Majorana pairs on the edge, between which bulk decimations yield additional weaker spikes.

5.1 Probability distribution calculation

In this section we calculate the probability distribution for the energy of decimated Majorana pairs, as well as their coupling to the probe. A chain initially coupled to an STM probe at the left end develops couplings to *all* odd-numbered Majoranas under the RG flow. As seen in the previous chapter, the magnitude of the coupling decreases sharply with distance along the chain, and we expect edge decimations to be the dominant processes. As a check, this will be proven explicitly below.

Define $u_n(\tau, \ell; \Gamma)$ as the probability that after n edge decimations, the Majorana currently on the edge is located a distance ℓ from the probe with a coupling $a \equiv e^{-\tau}$ at RG scale Γ. The integer n marks how many previous edge decimations occurred before the edge ended up at the Majorana we're looking at now. This counting scheme doesn't include decimations within the bulk; rather, the decimation process is divided into "eras" separated by edge decimations. The evolution of bulk couplings can be accounted for from the edge decimations in a controlled way. The flow equation for u_n is given by:

$$\frac{du_n}{d\Gamma} = -\int d\ell_1 P\left(0, \ell_1\right) u_n\left(\tau, \ell; \Gamma\right) \tag{5.1}$$

$$+ \int d\ell_1 d\ell_2 d\ell' d\tau' d\zeta_2 P\left(0, \ell_1\right) P\left(\zeta_2, \ell_2\right) u_{n-1}\left(\tau', \ell'; \Gamma\right) \delta\left(\tau - \tau' - \zeta_2\right) \delta\left(\ell - \ell' - \ell_1 - \ell_2\right)$$

Eq. 5.1 accounts for two ways the probability can change: 1) The Majorana is on the edge

and gets decimated. This is the first term on the RHS: the probability is reduced if the edge is decimated. 2) The Majorana is in the second-to-last pair, and the edge pair is decimated, leaving the Majorana in question at the new edge. This source term is the second term on the RHS: the distance from the probe to the edge shifts to the position of the new edge Majorana, and its coupling is calculated from the old edge's coupling. Here $P(\zeta, \ell)$ is the critical probability distribution of nearest-neighbor log-energies, ζ.

Before continuing with the calculation of $du_n/d\Gamma$, we note some useful facts about $P(\zeta, \ell)$ from the study of the transverse-field Ising model. It will be easier to carry out the calculation in the Laplace conjugate of ℓ and τ, which we define to be y and λ respectively. The bond probability distribution becomes

$$P(\zeta, y) = \int d\ell P(\zeta, \ell) e^{-y\ell} = \frac{\sqrt{y}}{\sinh\left(\sqrt{y}\Gamma\right)} e^{-\sqrt{y}\coth(\sqrt{y}\Gamma)\zeta} \tag{5.2}$$

It will be useful later to evaluate this function at $y = 0$:

$$\lim_{y \to 0} \frac{\sqrt{y}}{\sinh(\sqrt{y}\Gamma)} = \frac{1}{\Gamma}$$

$$P(\zeta, y = 0) = 1/\Gamma. \tag{5.3}$$

After carrying out the Laplace transform in τ, the probability distribution becomes

$$P(\lambda, y) = \int d\zeta P(\zeta, y) e^{-\lambda\zeta} = \frac{\sqrt{y}}{\sinh(\sqrt{y}\Gamma)} \frac{1}{\lambda + \sqrt{y}\coth(\sqrt{y}\Gamma)}. \tag{5.4}$$

$$P(\lambda, y = 0) = \frac{1}{1 + \lambda\Gamma} \tag{5.5}$$

To make progress on simplifying the flow equation, we carry out a Laplace transform on Eq. 5.1 in ℓ and τ. The LHS of Eq. 5.1 becomes

$$\int d\ell d\tau e^{-y\ell} e^{-\lambda\tau} \frac{du_n(\tau, \ell; \Gamma)}{d\Gamma} = \frac{du_n(\lambda, y; \Gamma)}{d\Gamma}$$

The first term on the RHS of Eq. 5.1 becomes

$$-\int d\ell_1 P(0, \ell_1) u_n(\lambda, y; \Gamma) = -P(\zeta = 0, y = 0) u_n(\lambda, y; \Gamma) \tag{5.6}$$

The second term on the RHS of Eq. 5.1 is given by

$$\int d\ell_1 d\ell_2 d\ell' d\zeta_2 d\tau' e^{-y(\ell' + \ell_1 + \ell_2)} e^{-\lambda(\tau' + \zeta_2)} P(\zeta = 0, \ell_1) P(\zeta, \ell_2) u_{n-1}(\tau', \ell'; \Gamma)$$

$$= u_{n-1}(\lambda, y; \Gamma) P(\zeta = 0, y) P(\lambda, y) \tag{5.7}$$

Combining Eqs. 5.6-5.7, the flow equation becomes

$$\frac{du_n}{d\Gamma} = -P\left(\zeta = 0, y = 0\right) u_n + P\left(\zeta = 0, y\right) P\left(\lambda, y\right) u_{n-1}\left(\lambda, y; \Gamma\right) \tag{5.8}$$

$$= -\frac{1}{\Gamma} u_n + \frac{y}{\sinh^2(\sqrt{y}\Gamma)} \frac{u_{n-1}}{\lambda + \sqrt{y}\coth(\sqrt{y}\Gamma)} \tag{5.9}$$

where in Eq. 5.9, we have substituted in the appropriate forms of the probability distributions. The problem of solving for u_n is made simpler by the following two substitutions for the variables x and w:

$$x = \sqrt{y}\coth(\sqrt{y}\Gamma) \tag{5.10a}$$

$$\frac{dx}{d\Gamma} = -\frac{y}{\sinh^2(\sqrt{y}\Gamma)}$$

$$w_n = \Gamma u_n \tag{5.10b}$$

$$\frac{du_n}{d\Gamma} = \frac{1}{\Gamma}\frac{dw_n}{d\Gamma} - \frac{1}{\Gamma^2}w_n$$

Now the flow equation, Eq. 5.9 becomes

$$\frac{dw_n}{d\Gamma} = -w_{n-1}\frac{dx}{d\Gamma}\frac{1}{x+\lambda} \tag{5.11}$$

This has the solution

$$w_n = \frac{\Gamma_0}{n!}\ln^n\frac{x_0+\lambda}{x+\lambda} \tag{5.12}$$

Summing over the edge decimations n, and switching variables back to u, we arrive at an expression for the probability distribution of energy and coupling:

$$u(\lambda, x; \Gamma) = \frac{\Gamma_0}{\Gamma}\frac{x_0+\lambda}{x+\lambda}. \tag{5.13}$$

This is the main result of this section: u_n gives the probability that after n edge decimations, the Majorana currently at the edge is at a distance ℓ to the probe, with coupling $e^{-\tau}$. Note getting the τ- and ℓ-dependence requires doing an inverse Laplace transform on Eq. 5.13. Below, we use this result to calculate joint probability distributions involving coupling to one or two probes.

5.2   Single-Lead geometry

To find the energies of the chain, we consider an STM lead that allows electrons to tunnel into one end of the chain. The single-lead case is equivalent to a semi-infinite chain, where the length of the chain is not an important parameter. To find the energies of the Majorana pairs, or equivalently the RG scales at which Majorana pairs were decimated, we need a joint probability describing the coupling and energy. Consider

$$\frac{dJ_n^{(edge)}(\tau; \Gamma)}{d\Gamma} = P(\zeta = 0)u_n(\tau, y = 0; \Gamma), \tag{5.14}$$

$$= \frac{\Gamma_0}{\Gamma^2}\frac{1}{n!}\ln^n\left(\frac{\lambda+1/\Gamma_0}{\lambda+1/\Gamma}\right). \tag{5.15}$$

We don't need to worry about the effective length of the chain, related to ℓ, in the semi-infinite chain, so set $y = 0$ here. $dJ_n/d\Gamma$ is the the probability density that a Majorana

survived n edge decimations, then got decimated at the edge at Γ with coupling $e^{-\tau}$. Note that this is a density, not a probability, since $P(\zeta = 0)$ gives the probability density that the Majorana is decimated. For fixed n, the probability density first increases with Γ, as expected since the Majorana survived the first $n-1$ decimations. The probability density reaches a peak at some value of Γ, then decreases as a subsequent edge decimation reduces the chance of the Majorana's survival.

The discussion so far has involved successive edge decimations, but in between edge decimations there are bulk pairs decimations as well. Let $dJ_n^{(bulk)}/d\Gamma$ be the probability density that after n edge decimations, a bulk Majorana pair is decimated while coupled to the probe with $e^{-\tau}$. We can calculate its frozen coupling from the coupling of the edge and the values of the bonds in between:

$$\frac{dJ_n^{(bulk)}(\lambda, \Gamma)}{d\Gamma} = \sum_{m=1}^{\infty} \int d\ell d\tau d\zeta_0...d\zeta_{m-1} d\ell_0...d\ell_m e^{-y\ell} \; e^{\tau\lambda} u_n(\tau', \ell'; \gamma) \tag{5.16}$$

$$\cdot P(\zeta_m = 0, \ell_m) P(\zeta_0, \ell_0)...P(\zeta_{m-1}, \ell_{m-1}) \delta\left(\tau - \tau' - \sum_{i=0}^{m-1} \zeta_i\right) \delta(\ell - \ell')$$

We saw in Eq. 4.16c that the coupling picks up multiplicative factors of the energies between the edge and the decimated Majorana. The delta function in τ in Eq. 5.16 reflects the fact that the logarithmic couplings pick up additive factors of the log energies. Evaluating the integrals gives

$$\frac{dJ_n^{(bulk)}(\lambda, \Gamma)}{d\Gamma} = \sum_{m=1}^{\infty} u_n(\lambda, y; \Gamma) P(\zeta = 0, y = 0) P(\lambda, y = 0)^m \tag{5.17}$$

Using the fact that the first two factors in Eq. 5.17 are equal to the edge probability density, and carrying out the sum over sites m,

$$\frac{dJ_n^{(bulk)}(\lambda, \Gamma)}{d\Gamma} = \frac{dJ^{(edge)}}{d\Gamma} \sum_{m=1}^{\infty} P(\lambda, y = 0)^m$$

$$= \frac{1}{\Gamma} u_n(\lambda, y = 0) \sum_{m=1}^{\infty} \frac{1}{(1 + \lambda\Gamma)^m}$$

$$= \frac{1}{\lambda\Gamma^2} u_n(\lambda, y = 0). \tag{5.18}$$

5.2.1 Aside on Laplace Transform tricks

In the previous section, we have found the Laplace transforms of various probability densities. Calculating average or typical values seems to require the tedious matter of inverse Laplace transforming, followed by integrating over relevant terms. However we review here some ways to get around the inverse Laplace transform.

1. For quantities involving only the energy, without regard to coupling, we use the marginal distribution for $dJ/d\Gamma$ with τ integrated out. Rather than inverse Laplace

transforming $dJ(\lambda; \Gamma)/d\Gamma$ and then integrating over τ, it is equivalent to substitute $\lambda = 0$ into the Laplace transform:

$$\frac{dJ(\Gamma)}{d\Gamma} = \int_0^\infty d\tau \frac{dJ(\tau; \Gamma)}{d\Gamma}$$
$$= \int_0^\infty d\tau \frac{dJ(\tau; \Gamma)}{d\Gamma} e^{-\lambda\tau}|_{\lambda=0}$$
$$= \frac{dJ(\lambda; \Gamma)}{d\Gamma}|_{\lambda=0} \qquad (5.19)$$

2. For the average value of $e^{-2\tau}$, which is useful for average couplings to the probe, we evaluate the Laplace transform at $\lambda = 2$:

$$\langle e^{-2\tau} \rangle = \int_0^\infty d\tau \frac{dJ(\tau; \Gamma)}{d\Gamma} e^{-2\tau}$$
$$= \frac{dJ(\lambda; \Gamma)}{d\Gamma}|_{\lambda=2} \qquad (5.20)$$

3. As we describe below, it is sometimes necessary to average τ rather than $e^{-2\tau}$. To do this, we differentiate and then set $\lambda = 0$:

$$\langle \tau \rangle = -\frac{d}{d\lambda} \int_0^\infty d\tau \frac{dJ(\tau; \Gamma)}{d\Gamma} e^{-\tau\lambda}|_{\lambda=0}$$
$$= -\left(\frac{d}{d\lambda} \frac{dJ(\lambda; \Gamma)}{d\Gamma} \right)|_{\lambda=0} \qquad (5.21)$$

5.2.2 Location of edge peaks

We can use Eq. 5.15 to find the RG scales, or equivalently the energies, where edge decimations occur. Here we are interested only in the Γ-dependence, and the coupling can be integrated out by setting $\lambda = 0$. First it is instructive to check the normalization. A Majorana that becomes the edge after n edge decimations can itself be eliminated only as an edge decimation, *ie* with probability 1.

$$\int_{\Gamma_0}^\infty \frac{dJ_n^{(edge)}(\lambda = 0)}{d\Gamma} d\Gamma = \int_{\Gamma_0}^\infty \frac{d\Gamma}{\Gamma_0} \frac{\Gamma_0^2}{\Gamma^2} \frac{1}{n!} \ln^n \left(\frac{\Gamma}{\Gamma_0} \right)$$
$$= \int_0^\infty dz e^z e^{-2z} \frac{1}{n!} z^n$$
$$= 1$$

where we have used the substitution $z = \ln(\Gamma/\Gamma_0)$. As expected, this to be normalized to one.

The quantity we'd most reasonably be interested in, the average value of Γ for a given n, doesn't converge. Let's instead average $z = ln(\Gamma/\Gamma_0)$ and then exponentiate:

$$\langle \ln \left(\frac{\Gamma}{\Gamma_0} \right) \rangle = \int_0^\infty d\ell e^{-\ell} \frac{1}{n!} \ell^{n+1}$$
$$= n + 1$$
$$\Gamma_n(av) = \Gamma_0 e^{n+1} \qquad (5.22)$$

dJ/dΓ

ln(ln(1/E))
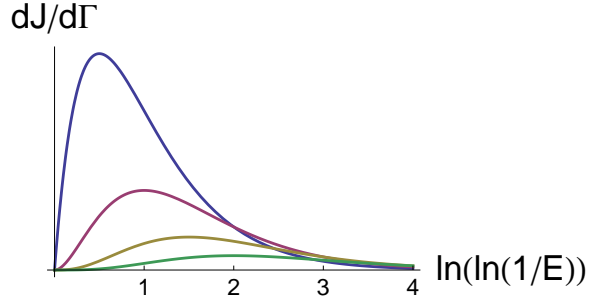
Figure 5.1: Marginal distribution of edge energies for $n = 1$-4. The n'th peak has a maximum at $\ln(\ln(1/E)) = n/2$. dI/dV thus has peaks at regular intervals in $\ln(\ln(1/V))$.

Alternatively, the most probable location of the n-th peak is found by differentiating $dJ_n^{(edge)}/d\Gamma$:

$$\frac{d}{d\Gamma} \frac{dJ_n^{(edge)}(\lambda = 0)}{d\Gamma} = -2\frac{\Gamma_0}{\Gamma^3}\frac{1}{n!} \ln^n\left(\frac{\Gamma}{\Gamma_0}\right) + \frac{\Gamma_0}{\Gamma^3}\frac{1}{(n-1)!} \ln^{n-1}\left(\frac{\Gamma}{\Gamma_0}\right)$$

$$\Gamma_n(mp) = \Gamma_0 e^{n/2} \tag{5.23}$$

Either way, we see that $\ln \Gamma_n$ scales as n. The corresponding energy, $E_n \sim e^{-\Gamma_n}$, then scales as $e^{-\Gamma_0 e^n}$. On a plot of STM tunneling data, strong peaks in dI/dV will appear at these values of V, corresponding to Majorana pairs decimated at the edge. Plotting the data against $\ln(\ln(1/V))$ rather than V gives peaks at regular intervals (Fig. 5.1).

5.2.3 Strength of peaks

One immediate question is, what about peaks from bulk decimations? The edge decimations are the dominant ones since they have much stronger coupling to the probe, but we'd like to show that the bulk contributions can be neglected. For this, we need average or typical values of the coupling. The typical values are more experimentally feasible, since average values require measurements on a large number of samples. The dI/dV curve depends on the coupling, therefore the relevant quantity to consider is not $\langle\tau\rangle$ but $e^{-\langle\tau\rangle}$.

n-th Edge decimation

The typical and average coupling of an edge peak, $a = e^{-\tau}$, are given by $e^{-2\langle\tau\rangle}$ and $\langle e^{-2\tau}\rangle$ respectively. The distinction between these two expressions is rather subtle and relies on the fact that disorder-averages are dominated by rare events. In most realizations of disorder the bulk pairs, which make up the majority of decimated pairs, will be very weakly coupled to the probe. A small value of the coupling a is equivalent to a large value of $\tau = -\ln a$. The average coupling ($\langle e^{-2\tau}\rangle$) is dominated by terms with small τ: most of the terms in the sum are vanishingly small, and rare terms with strong coupling will have a large effect. On the other hand, calculating $e^{-2\langle\tau\rangle}$ reverses the order of operations by

finding the average of τ first and then exponentiating. Unlike the average coupling, $e^{-2\langle\tau\rangle}$ protects against domination by rare anomalous terms because the sum is over τ itself rather than $e^{-2\tau}$. Most terms are enormous, and the rare cases with strong coupling/small τ get washed out in the sum. So this is the expression that gives a typical value of coupling.

$$a_{typ} = e^{-2\langle\tau\rangle} \tag{5.24a}$$

$$a_{av} = \langle e^{-2\tau}\rangle \tag{5.24b}$$

Lastly, the average τ at a particular value of Γ is calculated *given that* an edge decimation took place at Γ. The conditional is necessary to separate out the effect of where the decimations occur in the first place. To calculate $e^{-2\langle\tau\rangle}$, we use the trick outlined in Eq. 5.21 of differentiating and setting $\lambda = 0$:

$$\langle\tau\rangle_n^{(edge)} = \frac{1}{dJ_n/d\Gamma}\frac{d}{d\lambda}\frac{dJ_n^{(bulk)}}{d\Gamma}\Big|_{\lambda=0} = \frac{n}{\ln(\Gamma/\Gamma_0)}(\Gamma_0 - \Gamma) \tag{5.25}$$

This result says typical values of τ increase with Γ, *ie* Majorana pairs decimated later in the RG flow have smaller couplings to the probe. Physically, this is because as the decimations proceed, the couplings have longer to accumulate higher order coefficients, each of which is less than unity. Using the result from Eq. 5.23, $\Gamma \sim e^{n/2}$ for a typical edge decimation, the typical coupling of the n-th decimated edge pair scales as

$$e^{-2\langle\tau\rangle_n^{(edge)}} \sim e^{-4\Gamma_0 e^{n/2}} \tag{5.26}$$

All bulk contributions

We now address bulk decimations and their contributions to the IV curve, which – unlike dI/dV – shows represents the integrated sum of all peaks up to a certain energy scale. We show here that the sum of all bulk contributions in a particular era between two edge decimations is negligible compared to the edge peak and can safely be neglected.

The probability density for a bulk decimation at position m in the chain following n bulk decimations is given by

$$dJ_n^{(m)}/d\Gamma = dJ_n^{(edge)}/d\Gamma P(\lambda)^{m-1}\left[1 + P(\lambda)\right] \tag{5.27}$$

The typical correlation of a bulk decimation is found to be

$$e^{-2\langle\tau\rangle_n^{(m)}} = e^{-2\langle\tau\rangle_n^{(edge)}} \cdot e^{-(2m-1)\Gamma_0 e^{n/2}} \tag{5.28}$$

The typical strength of a peak coming from the m-th site along the chain after n edge decimations is suppressed compared to the n-th edge peak by a factor of $\sim e^{-(2m-1)\Gamma_0 e^{n/2}}$. For a given n, the bulk peaks from further along the chain get strongly suppressed.

In summing up the bulk contributions, we must again decide which order to exponentiate τ and sum over sites along the chain. Adding up all the bulk values of τ will make it diverge since the bulk couplings typically very small. On the other hand, the average value of bulk couplings a does not diverge because it is dominated by the rare events when some
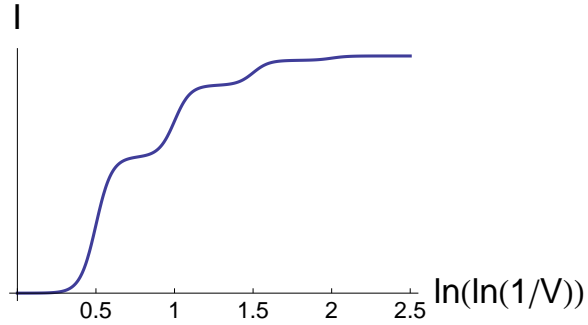
Figure 5.2: Typical IV curve obtained by integrating dI/dV from high voltage down to V. A sharp rise in current occurs at values of V corresponding to typical energies of edge pairs.

bulk pairs have anomalously strong coupling. The latter is also the experimentally relevant order of operations: between edge decimations, the IV curve shows the coupling of each bulk decimation, summed over sites along the chain. We take this to be the appropriate order of operations for this step and find the typical bulk contributions to be

$$\sum_{m\ even} e^{-2\langle\tau\rangle_n^{(m)}} \sim e^{-2\langle\tau\rangle_n^{(edge)}} e^{-3\Gamma_0 e^{n/2}} \tag{5.29}$$

This result shows that the contribution from the peaks due to all the bulk decimations between two successive edge decimations is suppressed compared the edge contributions by a factor of $e^{-3e^{\Gamma_0 n/2}}$, and thus can safely be neglected.

Fig. 5.2 shows the predicted current plotted vs. $\ln(\ln(1/V))$. Each time the voltage crosses an edge peak from above, there is a sharp rise in the current as the probe couples to a decimated Majorana pair. For higher n, i.e., edge decimations at lower energies, the typical coupling and current jumps decrease sharply.

Chapter 6

Two-Lead Transport Measurements

At low energies the random Majorana chain behaves like a set of decoupled Majorana pairs. Physical properties can be calculated from contributions from each pair, weighted by an appropriate probability distribution. In this chapter, we consider a finite chain with each end coupled to an STM probe. The two-lead geometry is useful for studying electrical and thermal transport, and we calculate these quantities below.

6.1 2-Lead Scattering Matrix

In this section, we set up the calculation of conductance as a scattering problem: incoming electrons from two leads scatter off the Majorana pair to produce outgoing electrons and holes. We examine the case where both leads are biased at the same voltage V, with the superconducting region grounded. The scattering matrix is written in the basis $(\psi_{e,1}, \psi_{e,2}, \psi_{h,1}, \psi_{h,2})$ of electron and hole states in the leads. Following the derivation in [65], the scattering matrix can be written as

$$S(E) = 1 + 2\pi i W^\dagger (H_M - E - i\pi W W^\dagger)^{-1} W \tag{6.1}$$

where H_M is the Hamiltonian for the Majorana splitting, and W is the coupling between the Majoranas and the leads:

$$H_M = \begin{pmatrix} 0 & iE_M \\ -iE_M & 0 \end{pmatrix}, \tag{6.2a}$$

$$W = \begin{pmatrix} w_1 & 0 & w_1^* & 0 \\ 0 & w_2 & 0 & w_2^* \end{pmatrix}. \tag{6.2b}$$

E_M is the coupling between Majoranas, and $a_i = 2\pi w_i^2$ give the coupling to each lead. Substituting these forms for H_M and W into Eq. 6.1 gives

$$S(E) = \begin{pmatrix} 1+A & A \\ A & 1+A \end{pmatrix} \tag{6.3}$$

where

$$A = \frac{1}{Z} \begin{pmatrix} ia_1(E + ia_2) & -E_M\sqrt{a_1 a_2} \\ E_M\sqrt{a_1 a_2} & ia_2(E + ia_1) \end{pmatrix} \qquad (6.4)$$

and $Z = E_M^2 - (E + ia_1)(E + ia_2)$.

$S(E)$ must be a unitary matrix, which given the form of Eq. 6.3, imposes the following constraint on the matrix A:

$$A + A^\dagger + 2AA^\dagger = 0. \qquad (6.5)$$

It is straightforward to show that the expression for A found in Eq. 6.4 satisfies this constraint. The matrix elements of the scattering matrix must also reflect the symmetries of the system, which in this case is only particle-hole symmetry. This imposes the following constraint on the reflection and transmission coefficients r and t, which are in general functions of energy:

$$r_{ee}(E) = r_{hh}^*(-E) \quad , \quad r_{eh}(E) = r_{he}^*(-E) \qquad (6.6a)$$

$$t_{ee}(E) = t_{hh}^*(-E) \quad , \quad t_{eh}(E) = t_{he}^*(-E) \qquad (6.6b)$$

Our choice of basis means that the scattering matrix can be expressed as

$$S = \begin{pmatrix} r_{ee} & t_{ee}' & r_{he} & t_{he}' \\ t_{ee} & r_{ee}' & t_{he} & r_{he}' \\ r_{eh} & t_{eh}' & r_{hh} & t_{hh}' \\ t_{eh} & r_{eh}' & t_{hh} & r_{hh}' \end{pmatrix} \qquad (6.7)$$

Comparing Eqs. 6.7 and 6.3, we see that $r_{ee} = 1 + A_{11}$. The expression for A_{11} found in Eq, 6.4 satisfies $A_{11}(E) = A_{11}^*(-E)$, which implies that $r_{ee}(E) = r_{ee}^*(-E)$. Finally we use the fact that $r_{hh} = 1 + A_{11} = r_{ee}$ to get $r_{ee}^*(-E) = r_{hh}(E)$, as required by particle-hole symmetry. The same argument holds for the other matrix elements.

6.2 Electrical Current

6.2.1 Single Majorana Pair

We derive an expression for the current at arbitrary voltage and temperature. At zero-temperature and very low voltage, this expression agrees with previously found results. In addition, we show that the expression can be evaluated exactly when the voltage is much higher than the Majorana coupling. In this limit, the current is proportional to the sum of the STM couplings to the pair.

Following Ref. [7], the charge current in each lead is given by

$$I_1 = \frac{e}{h} \int_0^\infty dE\ f(E) \left(1 - |r_{ee}|^2 - |t_{ee}'|^2 + |r_{eh}|^2 + |t_{eh}'|^2\right) \qquad (6.8a)$$

$$I_2 = \frac{e}{h} \int_0^\infty dE\ f(E) \left(1 - |r_{ee}'|^2 - |t_{ee}|^2 + |r_{eh}'|^2 + |t_{eh}|^2\right) \qquad (6.8b)$$

where $f(E) = (1 + e^{(E-V)/k_B T})^{-1}$. In the $T = 0$ limit, the expression simplifies to

$$I_1 = \frac{e}{h} \int_0^V dE \ (1 - \det r - \det t') \tag{6.9}$$

where the last line follows from particle-hole symmetry. Alternatively, we can simplify Eq. 6.8a using unitarity, which requires $|r_{ee}|^2 + |r_{eh}|^2 + |t'_{ee}|^2 + |t'_{eh}|^2 = 1$. This allows the current to be written as

$$I_1 = \frac{2e}{h} \int_0^\infty dE \ f(E) \left(|r_{eh}|^2 + |t'_{eh}|^2 \right) \tag{6.10}$$

At zero temperature, when the voltage difference between the left and right leads is V, the expression for current becomes

$$I_1 = \frac{2e}{h} \int_0^V dE \ \frac{E^2 a_1^2 + a_1 a_2 (E_M^2 + a_1 a_2)}{(E^2 - E_M^2 - a_1 a_2)^2 + E^2 (a_1 + a_2)^2} \tag{6.11}$$

We can find the current at non-zero values of temperature by restoring the factor of $f(E)$ in the integrand.

Previous works have examined the current in the low-voltage, strong-coupling limit: $E_M \gg eV, a_i$ [65, 55]. In this case, the integrand in Eq. 6.11 is greatly reduced to $a_1 a_2 / E_M^2$, and the current is simply

$$I_1 = I_2 = \frac{2e^2}{h} \frac{a_1 a_2}{E_M^2} V \tag{6.12}$$

This agrees with previously found expressions [65].

It is also interesting to consider the high-voltage regime, which as far as we know has not been previously investigated. dI/dV, given by the integrand of Eq. 6.11, reaches a maximum at $E = E_M$, leading to a sharp rise in the current as the voltage is ramped through the Majorana splitting strength. At this voltage, electrons from either lead can tunnel resonantly through the Majorana pair by populating the effective electron state formed from the two Majorana states. When $V \gg E_M$, the integral in Eq. 6.11 can be evaluated analytically to give

$$I_i = \frac{2e}{h} \frac{\pi}{2} a_i \tag{6.13}$$

The current flowing into the superconductor, $I = I_1 + I_2$, is therefore proportional to the sum of the couplings $a_1 + a_2$.

6.2.2 Extending to Majorana Chain

Since the current due to a single Majorana pair depends on the sum of the couplings, a dominant contribution occurs when either coupling is strong. We make use of the fact that edge decimations are coupled much more strongly to the lead than decimations occurring in the bulk of the chain, so that only edge contributions to the current need to be considered.
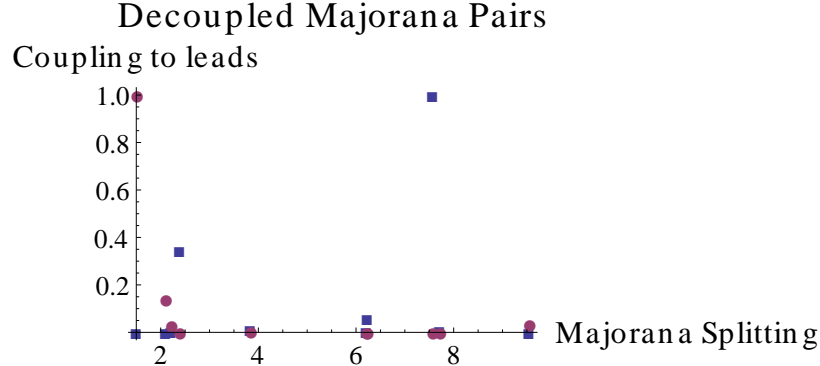
Figure 6.1: Typical distribution of Majorana splitting and coupling to the two leads (see explanation in text). The coupling is shown here as a fraction of the original coupling to the chain. The chain in this figure has five edge decimations, three of which are visible as strong coupling to a lead.

A decimation on, say the left edge, results in a large value for a_1 and a negligible value for a_2. In the high-voltage regime, where the current is proportional to $a_1 + a_2$, this leads to a dominant contribution to the current. By contrast, in the low-voltage limit the current is proportional to $a_1 a_2$. In this case, dominant contributions arise from decimations with non-trivial values of both a_1 and a_2, *ie* bulk pairs. We assume that the two edges are independent, which is reasonable for the earlier eras that have the strongest couplings.

We study the current numerically with a chain of 20 Majorana fermions. The nearest neighbor bonds are taken randomly from a log-normal distribution, and a metallic lead is coupled to the Majorana at each end. The effect of the RSRG described in Chp. 4 is to transform this system to a set of 10 Majorana pairs, each coupled to the two leads. Fig. 6.1 shows the calculated distribution for the Majorana splitting as well as the coupling to each lead for one particular realization of disorder. The horizontal axis indicates the Majorana splitting. At each value of energy where a Majorana pair was decimated, there are two data points. The blue square represents the odd-numbered Majorana of the pair, with the vertical position indicating its coupling to the left lead. The purple circle indicates the coupling of the even-numbered Majorana in the pair to the right lead.

The evolution of the chain with the RG flow is found by starting at the high energy or right end of the plot and reading leftward. In the previous chapter, we found analytically that Majorana pairs decimated at the active edge of the chain have the strongest coupling to the leads. This particular chain has five left edge decimations occurring at splittings of 7.6, 2.4, 2.2, 2.1, and 1.5. The pair with splitting 1.5 is the last pair to be decimated and also represents the only right edge decimation for this chain. Fig. 6.1 shows that the majority of Majoranas are very weakly coupled to a lead; however the pairs at 7.6, 2.4, and 1.5 have non-trivial coupling. As predicted, these pairs that were decimated while on the edge have strong coupling to a lead, while bulk decimations result in weaker coupling.

Given the splitting and couplings of each of the 10 Majorana pairs, we compute the total current due to the chain by evaluating Eq. 6.11 for each pair and then summing.
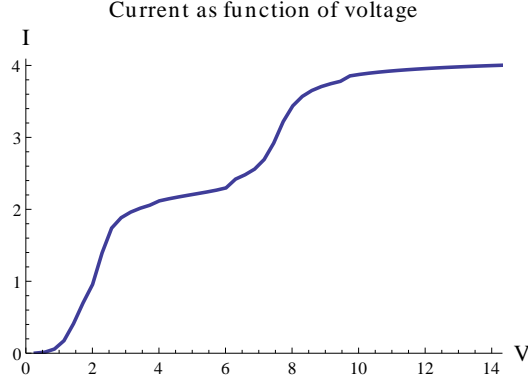
Figure 6.2: Typical IV-curve for the Majorana chain connected to two leads. Sharp increases occur at the Majorana splitting energies of the decimated pairs, with the strength of the jump determined by the coupling to the leads.

The result is shown in Fig. 6.11. The current shows a sharp increase each time the voltage is ramped through a Majorana splitting, with an amplitude given by the sum of the couplings to the leads. The biggest jumps occur at 2.4 and 7.6, corresponding to the Majorana pairs most strongly coupled to the left lead, while smaller jumps at 3.8, 6.2, and 9.5 are due to bulk decimations between successive edge decimations.

6.3 Heat Current

6.3.1 Single Majorana Pair

We derive an expression for the heat current in terms of the transmission eigenvalues found above. The main difference from the electrical current is that the contributions from the electrons and holes have the same sign [19].

$$
\begin{aligned}
Q_1 &= \frac{T - T_1}{hT} \int_0^\infty dE \ E^2 \left(\frac{-\partial f}{\partial E} \right) \left(1 - |r_{ee}|^2 - |r_{eh}|^2 \right) \\
&+ \frac{T - T_2}{hT} \int_0^\infty dE \ E^2 \left(\frac{-\partial f}{\partial E} \right) \left(-|t'_{ee}|^2 - |t'_{eh}|^2 \right) \\
&= \frac{\Delta T}{hT} \int_0^\infty dE \ \frac{E^2}{2k_b T \cosh^2 \frac{E}{2k_B T}} \left(|t'_{ee}|^2 + |t'_{eh}|^2 \right)
\end{aligned} \tag{6.14}
$$

where $\Delta T = T_2 - T_1$. We evaluate this expression by substituting the following form of the transmission coefficients,

$$
|t'_{ee}|^2 + |t'_{eh}|^2 = \frac{2E_M^2 a_1 a_2}{E^4 + E^2(a_1^2 + a_2^2 - 2E_M^2) + (E_M^2 + a_1 a_2)^2} \tag{6.15}
$$

Numerical evaluation of the heat current shows that it reaches a maximum at $T \approx 0.4 E_M$, where the peaks of $Tr \ tt^\dagger$ and the derivative of the Fermi-Dirac distribution are equal.
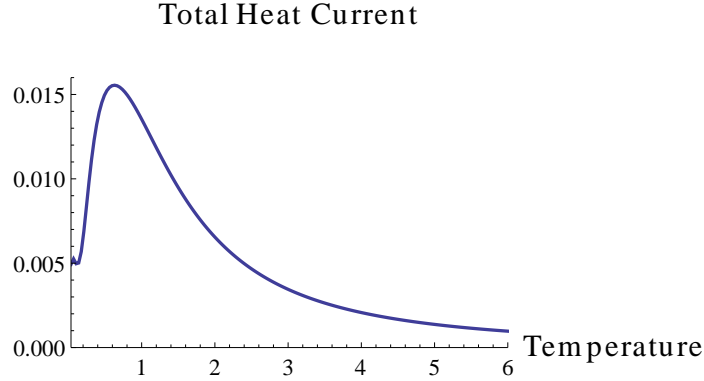
Total Heat Current

Figure 6.3: Typical heat current of the chain as a function of temperature. The current displays a peak each time the temperature is increased through 0.4 times a Majorana splitting; however, separate peaks are difficult to distinguish unless at very low temperatures.

For very low temperatures ($T < 0.05\ E_M$), $Tr\ tt^\dagger(E)$ can be replaced by $Tr\ tt^\dagger(0)$ and the thermal conductance Q_1/T becomes constant. We find that the thermal conductance reaches a maximum value of $\frac{k_b^2 T \pi^2}{6h}$ when $E_m^2 = a_1 a_2$. It can also be shown that for this relation between the Majorana splitting and the couplings to the leads, det $r = 0$, This result is in agreement with a previous result that the thermal conductance is quantized at this value when det $r = 0$ [2].

6.3.2   Extending to Majorana Chain

We again consider a chain of 20 Majorana fermions with nearest neighbors chosen from a log-normal distribution and two couplings to a metallic lead at either end. Similar to the calculation in Sec. 6.2.2, we first implement the RSRG to reduce the chain to a set of 10 Majorana pairs. This gives the splittings of each Majorana pair as well as its couplings to the leads. The heat current is found by evaluating Eqs. 6.14- 6.15 for each pair and then summing the contributions. Fig. 6.3 shows the result for a typical chain as a function of temperature. We expect peaks located at $T \approx 0.4 E_M$ for each of the decimated Majorana pairs, although thermal broadening makes the contributions from different pairs much harder to distinguish than in the electrical current. For the chain shown in Fig. 6.3, the heat current mainly comes from the Majorana pairs with splitting 1.2, 2.4, and 2.7, but these contributions merge into the single large peak shown in the figure. Distinct peaks may occur if the splittings are well separated from one another, as seen with the feature at low temperature that is due to a Majorana pair with splitting 0.32.

In the previous section, the charge current was found to mainly arise from edge decimations. In contrast, the biggest contributions to the thermal current come from pairs decimated near the midpoint of the chain. The thermal current shown in Fig. 6.3 is mainly due to Majorana pairs at splittings 1.2, 2.4, and 2.7, which are all bulk decimations. This suggests that the heat current is proportional to the product of the couplings – rather than

Contributions to Thermal Current
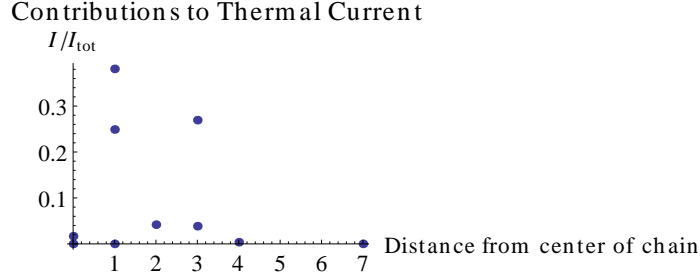
Figure 6.4: Contributions of each Majorana pair to the heat current, plotted against the distance from the center of the chain. Dominant contributions are due to Majorana pairs decimated near the effective center of the chain.
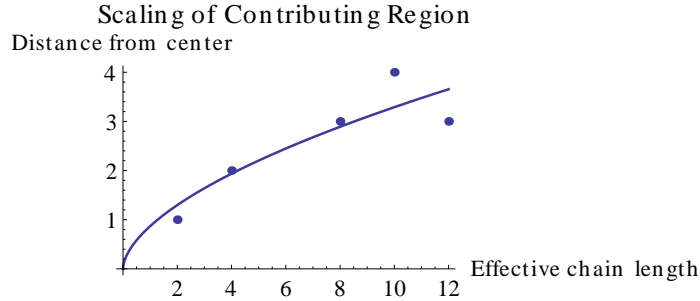
Figure 6.5: Size of the contributing region as a function of the effective chain length. A fit of the points to the function aL^b yielded $a = 0.87$ and $b = 0.42$, hence at least 0.995 of the current comes from a central region of size $L^{0.42}$ for this particular chain.

the sum, as for the electrical current. Fig. 6.4 shows the heat current due to each Majorana pair as a function of its distance to the effective chain center when decimated.

We hypothesize that at any stage of the RSRG with effective chain length L, only a fraction $1/L^{0.46}$ centered about the middle is responsible for 0.995 of the thermal current. To determine this, we study how the size of the contributing region scales with the effective length of the chain. Only the pairs whose thermal current is greater than 0.001 of the total are included in the plot, and we set an upper estimate of the contribution from remaining pairs at 0.005 of the total current. Fig. 6.5 shows the distance of a contributing pair from the center as a function of the effective length of the chain. For this particular chain, we find that the size of the central region scales as $L^{0.58}$. This implies that the fraction of the chain contributing to the heat current scales as $L^{0.42}$. Similar studies of several different realizations of disorder show a typical scaling of $L^{0.46}$. In addition the average scaling may deviate from the typical scaling found here, though this requires some knowledge of the probability distribution of these quantities and is still being investigated.

It is important to note that this method underestimates the size of the contributing region since we are only studying it through the pairs that were decimated. In practice, there

may have been more distant pairs which could have contributed but were not decimated in this particular realization of disorder.

Part II

Bulk-Boundary Correspondence

Chapter 7

Edge State and Bulk-boundary Theorems

7.1   Edge Modes and Topological Invariants

In light of recent interest in topological insulators and superconductors, it would be useful to formalize the relation between bulk topological quantities and properties of mid-gap edge states. This connection has been proven specifically for IQH states on a square lattice by deriving a winding number for the edge states. [37] Another approach using twisted boundary conditions has the advantage of including interactions and disorder, but cannot prove that the states exist at an open boundary. [68]

There has also been recent progress on analytic solutions of edge states in topological insulators [59, 97, 82] and topological superconductors. [78] These calculations are based on models using a specific Dirac Hamiltonian. Dirac systems are ubiquitous in condensed matter and particle physics systems and give rise to many exotic states. For example, every single-particle topologically ordered system can be realized with a Dirac Hamiltonian. [52, 76] They are used to model a variety of systems including polyacetylene, graphene, topological insulators and superconductors, *etc.* [44, 86, 34, 48, 71, 31, 17]

In this part we deepen the understanding of surface states by deriving their dispersion, effective theory, and chiral properties in terms of bulk quantities. Our work applies specifically to tight-binding Dirac Hamiltonians with nearest-layer interaction. For these systems we present a prescription for the edge states spectrum and prove the bulk-boundary correspondence. In addition, we derive a simple geometric method to calculate the energies and penetration depth of the edge states analytically.

7.2   Characterization of the nearest-layer Hamiltonian

To study a system with edges, consider a 2D/3D crystal that terminates on a line/surface. Translational symmetry is thus broken in the direction normal to the edges. However, we assume it is unbroken parallel to the surface, and the corresponding momentum $\mathbf{k}_\parallel$ is a good quantum number. In this way, any higher dimensional system can be decoupled into a family of one-dimension (1D) problems parameterized by $\mathbf{k}_\parallel$.

The Dirac Hamiltonian in momentum space $H(\mathbf{k})$ can always be expressed as a linear combination of g gamma matrices, $H(\mathbf{k}) = \mathbf{h}(\mathbf{k}) \cdot \mathbf{\Gamma}$. Here $\mathbf{\Gamma}$ is a vector of the hermitian gamma matrices (independent of $\mathbf{k}$) which satisfy the Clifford algebra $\Gamma^i \Gamma^j + \Gamma^j \Gamma^i = 2\delta^{ij}$. $\mathbf{h}$ is a real vector that maps the Brillouin zone to a closed curve in a g-dimensional vector space. Squaring the Hamiltonian gives $H^2 = (\mathbf{h} \cdot \mathbf{\Gamma})^2 = |\mathbf{h}|^2$. The eigenvalues of H, given by $E(\mathbf{k}) = \pm|\mathbf{h}(\mathbf{k})|$, can be thought of as the distance of the vector $\mathbf{h}$ to the origin. If $H(\mathbf{k})$ describes a band insulator with a bulk gap, then the locus of points traced by $\mathbf{h}(\mathbf{k})$ never intersects the origin.

Let us consider Dirac Hamiltonians with coupling between neighboring layers:

$$\mathcal{H} = \sum_{n,\mathbf{k}_\parallel} \Psi^\dagger_{n,\mathbf{k}_\parallel} \mathbf{\Gamma} \cdot \left[\mathbf{b} \, \Psi_{n-1,\mathbf{k}_\parallel} + \mathbf{b}^0 \, \Psi_{n,\mathbf{k}_\parallel} + \mathbf{b}^* \, \Psi_{n+1,\mathbf{k}_\parallel} \right], \tag{7.1}$$

where n labels the layers. Both $\mathbf{b}$ and $\mathbf{b}^0$ are dependent on $\mathbf{k}_\parallel$ but we will not write this dependence explicitly. $\Psi_{n,\mathbf{k}_\parallel}$ is a vector of quasiparticle annihilation operators at layer n that captures all the degrees of freedom (*i.e.* spin, pseudospin) at every site. Fourier transforming ($n \to k_\perp$) in the direction away from the edge, the bulk Hamiltonian becomes

$$\mathcal{H} = \sum_{k_\perp,\mathbf{k}_\parallel} \Psi^\dagger_{\mathbf{k}} \left[\mathbf{h}(\mathbf{k}) \cdot \mathbf{\Gamma}\right] \Psi_{\mathbf{k}}, \tag{7.2}$$

with

$$\begin{aligned} \mathbf{h}(\mathbf{k}) &= \mathbf{b}e^{-ik_\perp} + \mathbf{b}^0 + \mathbf{b}e^{ik_\perp} \\ &= \mathbf{b}^0 + 2\mathbf{b}^r \cos k_\perp + 2\mathbf{b}^i \sin k_\perp, \end{aligned} \tag{7.3}$$

where $\mathbf{b}^r$ and $\mathbf{b}^i$ are the real and imaginary components of the vector $\mathbf{b}$ respectively. We point out that $\mathbf{b}$ and $\mathbf{b}^0$ are independent of $k_\perp$

The curve traced out by $\mathbf{h}(\mathbf{k})$ for fixed $\mathbf{k}_\parallel$ is an ellipse living in the plane spanned by $\mathbf{b}^r$ and $\mathbf{b}^i$. $\mathbf{b}^0$ can be decomposed into a component $\mathbf{b}^0_\perp$ that is normal to this plane, and $\mathbf{b}^0_\parallel$ that lies within it. $\mathbf{b}^0_\parallel$ shifts the ellipse within the plane, while $\mathbf{b}^0_\perp$ lifts it uniformly. It will be useful to define

$$\mathbf{h}_\parallel(\mathbf{k}) = \mathbf{b}^0_\parallel + 2\mathbf{b}^r \cos k_\perp + 2\mathbf{b}^i \sin k_\perp \tag{7.4}$$

as the projection of $\mathbf{h}(\mathbf{k})$ on to the 2D plane spanned by $\mathbf{b}^r$ and $\mathbf{b}^i$. Note that this plane contains the origin, while the plane containing $\mathbf{h}$ is offset from the origin by the vector $\mathbf{b}^0_\perp$. Since $\mathbf{h}_\parallel$ maps the Brillouin zone to closed curves, it can be divided into two classes: ellipses that enclose the origin, and ellipses that do not.

As we shall see in the following section, the behavior of $\mathbf{h}(k_\perp)$ completely determines the topological nature of the system and holds the key to understanding the relation between existence of edge states and bulk topological invariants. This section contains the main result of the paper, where we prove two theorems, one relating the spectrum of edge states to $\mathbf{h}$, the other connecting $\mathbf{h}$ to a bulk topological invariant.
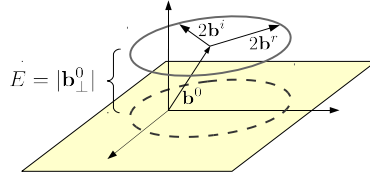
Figure 7.1: An illustration of Theorem 1. The gray ellipse is traced out by $\mathbf{h}(k_\perp) = \mathbf{b}^0 + 2\mathbf{b}^r \cos k_\perp + 2\mathbf{b}^i \sin k_\perp$ for a fixed parallel momentum $\mathbf{k}_\parallel$ [Eq. (7.3)]. The dotted ellipse ($\mathbf{h}_\parallel$) is $\mathbf{h}$ projected on to the plane spanned by $\mathbf{b}^r$ and $\mathbf{b}^i$. The displacement of the ellipse $\mathbf{h}$ from the dotted ellipse $\mathbf{h}_\parallel$ is given by $\mathbf{b}^0_\perp$, the component of $\mathbf{b}^0$ perpendicular to this plane. Theorem 1 says that an edge state exists if and only if the dotted ellipse encloses the origin (which holds true for the diagram above), and its energy is determined by the displacement $|\mathbf{b}^0_\perp|$.

7.3 Edge state energy

Theorem 1a. *The system has mid-gap edge states if and only if* $\mathbf{h}_\parallel(k_\perp)$ *encloses the origin.*

Theorem 1b. *The energies of the edge states are given by the distance from the origin to the plane containing* $\mathbf{h}$, *i.e.* $E_s = \pm|\mathbf{b}^0_\perp|$. *When the gamma matrices are the Pauli matrices, the energy of the left edge state (semi-infinite slab with $n > 0$) is given by:* $E_s = \mathbf{b}^0 \cdot \frac{\mathbf{b}^r \times \mathbf{b}^i}{|\mathbf{b}^r \times \mathbf{b}^i|}$.

Here we only sketch the main ideas behind two equivalent proofs of the theorem, leaving the full details to the Appendices. We present two approaches to this problem: a proof utilizing Green's functions [33] (*c.f.* Chp. 9) and a proof via transfer matrices [56] (*c.f.* Chp. 10). In this chapter, we consider one block of the decoupled system corresponding to fixed $\mathbf{k}_\parallel$.

We begin by writing the Green's function of the system without edges, where the full translational invariance makes a momentum space representation possible. A system with edges is then created from the fully periodic system by deleting the couplings between one pair of neighboring sites. The poles in the Green's function $G(E)$ at mid-gap energies E indicate the presence of edge states.

The bulk Green's function is given by

$$G_0\left(E; k_\perp\right) = \sum_i \frac{|\psi_i\rangle\langle\psi_i|}{E - E_i} \tag{7.5}$$

where i sums over the energy eigenstates of $H(k_\perp)$. Since we are interested in a boundary localized in real space, it is necessary to Fourier transform the bulk Green's function. For a system of size L this results in a $L \times L$ block matrix $G_0(E; y_i, y_j)$, where each block corresponds to mixing between the lattice sites y_i and y_j.

Next we write an expression V for the terms in the Hamiltonian that create the boundary by subtracting the hopping terms between sites y_{left} and y_{right}. For models with nearest neighbor interactions, the only non-zero matrix elements of V are those between y_{left}

and y_{right}. The Dyson equation gives an exact expression for the open boundary Green's function G in terms of the bulk Green's function G_0 and the cuts V needed to take the system from one geometry to the other:

$$G(E) = (I - G_0(E)V)^{-1}G_0(E). \tag{7.6}$$

The poles of $G(E)$ occur when the edge state energy satisfies $\text{Det}\,[I - G_0(E)V] = 0$. If an edge state exists with wavefunction u, it must satisfy $(I - G_0V)u = 0$. We note that this is the same as the Schrödinger equation $(E - H_0 - V)u = 0$. The benefit of the Green's function formalism is that it reduces the problem to only edge degrees of freedom and enables an analytic solution. This implies the following two statements:

$$\int dk_\perp \frac{\mathbf{h}_\parallel}{|\mathbf{h}_\parallel|^2} = 0, \tag{7.7a}$$

$$\int dk_\perp \, e^{ik_\perp} \frac{\mathbf{h}_\parallel \cdot \mathbf{b}^*}{|\mathbf{h}_\parallel|^2} = \pi. \tag{7.7b}$$

These conditions are satisfied if and only if $\mathbf{h}_\parallel$ encloses the origin, and the edge mode energy is given by $\pm|\mathbf{b}_\perp^0|$, where the sign is given by the orientation of $\mathbf{h}_\parallel$.

To prove Thm. 1 using transfer matrices, we consider a semi-infinite system with unit cells labeled by $n = 1, 2, 3$, *etc.* We seek a solution ψ_n to the single-particle Schrödinger equation:

$$\mathbf{b} \cdot \mathbf{\Gamma}\psi_{n-1} + \mathbf{b}^0 \cdot \mathbf{\Gamma}\psi_n + \mathbf{b}^* \cdot \mathbf{\Gamma}\psi_{n+1} = E\psi_n \tag{7.8}$$

for $n > 1$. At the edge site $n = 1$, we have $\mathbf{b}^0 \cdot \mathbf{\Gamma}\psi_1 + \mathbf{b}^* \cdot \mathbf{\Gamma}\psi_2 = E\psi_1$. This condition is enforced by applying Eq. (7.8) for $n = 1$ but stipulating that $\psi_0 = 0$. The recursion relation (7.8) relates ψ_{n+1} to ψ_n and ψ_{n-1}. Hence given ψ_1 (and $\psi_0 = 0$), we can recursively calculate all of ψ_n and construct the wavefunction.

An edge state requires ψ_n to be exponentially decaying as n increases, hence the solution ψ takes the form:

$$\psi_n = u_a\lambda_a^n + u_b\lambda_b^n, \tag{7.9}$$

where $u_a = -u_b$, and λ_a, λ_b are complex with $|\lambda_a|, |\lambda_b| < 1$. Algebraically, this is equivalent to having $E = \pm|\mathbf{b}_\perp^0|$ and finding two roots within the unit circle of the functions $L(\lambda)$ or $\bar{L}(\lambda)$, defined as

$$\begin{aligned} L(\lambda) &= \mathbf{h}_\parallel(-i\ln\lambda) \cdot (\hat{\mathbf{v}}_1 + i\hat{\mathbf{v}}_2), \\ \bar{L}(\lambda) &= \mathbf{h}_\parallel(-i\ln\lambda) \cdot (\hat{\mathbf{v}}_1 - i\hat{\mathbf{v}}_2), \end{aligned} \tag{7.10}$$

where $\hat{\mathbf{v}}_1, \hat{\mathbf{v}}_2$ are two orthonormal vectors that live in the plane of $\mathbf{h}_\parallel$. When $\lambda = e^{ik_\perp}$ lies on the unit circle, $L(\lambda)$ and $\bar{L}(\lambda)$ trace out the ellipse $\mathbf{h}(k_\perp)$ in the complex plane clockwise and counterclockwise, respectively. Because of this property, the number of times $\mathbf{h}(k_\perp)$ wraps the origin determines the number of zeroes of $L(\lambda)$ and whether the two solutions $\lambda_{a,b}$ in (7.9) exists. In Chp. 10, we provide the full details bridging these steps, and also compute the sign of the edge state energy as well as their penetration depth.

7.4 Bulk Chern number and chiral edge correspondence

In this section we prove Theorem 2, relating the bulk Chern number ν with the number of chiral edge modes for 2×2 Hamiltonians.

Theorem 2. *A chiral edge mode exists for a 2D bulk insulator if the bulk has a non-zero Chern number, i.e.* $\mathbf{h}(\mathbf{k})$ *wraps the origin. The number of chiral edge modes, counterclockwise minus clockwise, is given precisely by the Chern number.*

When the irreducible representation of $\boldsymbol{\Gamma}$ are 4×4 or larger, it can be shown that the Chern number is always zero. The edge states of any surface always appear in pairs with energy $+E_s$ and $-E_s$ and so the number of clockwise and counterclockwise chiral modes are always equal. We are particularly interested in 2×2 Hamiltonians because they can have nonzero Chern numbers and support chiral modes.

Consider an insulator in two dimensions whose Hamiltonian is written as a 2×2 traceless matrix: $H(k_x, k_y) = \mathbf{h}(k_x, k_y) \cdot \boldsymbol{\sigma}$. Because the bulk gap of an insulator is non-zero, $\mathbf{h}$ is non-zero at all points in the Brillouin zone. Hence $H(\mathbf{k})$ is a map from the Brillouin zone (torus) to a set of non-zero vectors with 3 components (sphere), and such maps can be characterized by a $\nu \in \mathbb{Z}$ topological invariant, known as the Chern number. [1] Hamiltonians with different Chern numbers ν cannot be deformed into one another without closing the bulk gap. In this context, the invariant ν determines the number of times the torus $\mathbf{h}(\mathbf{k})$ wraps around the origin.

To examine the edge states for an arbitrary edge, say one parallel to $\hat{y}$, we analyze the spectrum as a function of $k_\parallel = k_y$. The torus $\mathbf{h}(\mathbf{k})$ can be divided into a family of loops $\mathbf{h}(k_x)|_{k_y}$, each at a fixed value of k_y and giving information of the edge state at that momentum.

Before proceeding to the technical proof, we present a geometric argument with the aid of Fig. 7.2, which shows an example of a bulk insulator with Chern number $\nu = 1$. The important loops of fixed k_y are highlighted in black. Since ν is nonzero and the torus wraps the origin, it is always possible to find two loops that are coplanar with the origin, one of which encloses the origin and one that does not. In this example, the latter case occurs at $k_y = 0$, indicating no mid-gap edge states at this k_y. As we scan through different values of k_y, the loop moves out of this plane. At some critical momentum k_c (given by $\frac{\pi}{3}$ in Fig. 7.2), the projection of the loop onto this plane intersects the origin and an edge state emerges from the bulk conduction bands. At $k_y = \pi$, the loop is coplanar with the origin and encloses the origin, indicating zero-energy edge states at this value of k_y. As the plane of the loop passes through the origin, the energy of the edge state changes sign. The presence of edge modes for this range of momentum is shown as orange shading in Fig. 7.2. Eventually at some critical momentum k_v (given here by $\frac{5\pi}{3}$), the loop moves away from the origin and the edge state disappears in to the bulk valence band. Since the edge state energies at k_v and k_c have opposite signs, the edge band connects the bulk valence and the bulk conduction bands.

---

[1]Technically the Chern number is not defined for the map $\mathbf{h} : T^2 \to \mathbb{R}^3 - \{0\}$. However, we can compose $\mathbf{h}$ with the deformation retract $r : \mathbb{R}^3 - \{0\} \to S^2 = \mathbb{C}\mathrm{P}^1$ and the inclusion map $i : \mathbb{C}\mathrm{P}^1 \to \mathbb{C}\mathrm{P}^\infty$ to make the Chern number (first Chern class) well defined: $\varphi = i \circ r \circ \mathbf{h} : T^2 \to \mathbb{C}\mathrm{P}^\infty$. What it boils down to is that we are calling the induced map between the cohomology classes $\mathbf{h}^* : H^2(\mathbb{R} - \{0\}) \to H^2(T^2)$ the Chern number.

(a)   (b)
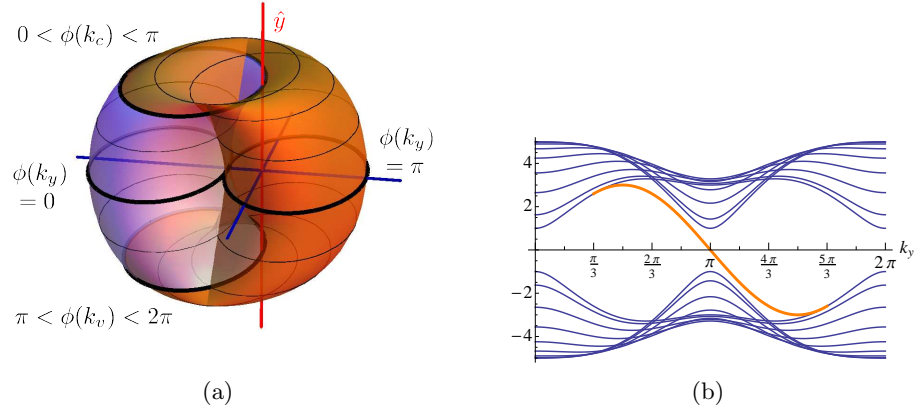
Figure 7.2: Illustration of bulk-boundary correspondence. Figure 7.2(a) shows the torus traced out by $\mathbf{h}(k_x, k_y)$ for a bulk insulator with Chern number $\nu = 1$. Each black loop maps out $\mathbf{h}(k_x)|_{k_y}$ for fixed values of k_y, the thick black lines guiding the eye to important loops. Setting $k_y = \pi$ gives the black loop on the right that encloses the origin, meaning there are zero-energy edge modes at this value of k_y. At $k_y = 0$, the black loop on the left lies in the plane of the origin without containing it, indicating no edge mode at $k_y = 0$. The black loops on the top and bottom ($k_v = \frac{5\pi}{3}, k_c = \frac{\pi}{3}$) have projections which intersect the origin, indicating the values of k_y where the edge band merges with the bulk bands. Figure 7.2(b) shows the band structure of the system with the edge mode drawn in orange. The model presented here is a $p + ip$ superconductor described in section 8.2 (see Eq. (8.4)) with parameters: $t = 1, \Delta_0 = 3, \mu = 1$.

Formally, we can describe each loop $\mathbf{h}(k_x)|_{k_y}$ by the Berry phase $\phi(k_y)$ living in a circle $[0, 2\pi]$ with $0 \sim 2\pi$. [10] The Berry phase can be formulated in various ways

$$\phi(k_y) = -\int_0^{2\pi} dk_x \, A_x(k_x, k_y) \tag{7.11a}$$

$$= \int_0^{k_y} dk_y' \int_0^{2\pi} dk_x \, F(k_x, k_y') \tag{7.11b}$$

$$= \frac{1}{2}\Omega(\mathbf{h}), \tag{7.11c}$$

where $A_j(\mathbf{k}) = \langle \psi_{\mathbf{k}} | i\partial_j | \psi_{\mathbf{k}} \rangle$ is the Berry connection of the filled energy states of $H(\mathbf{k})$, $F = \partial_x A_y - \partial_y A_x$ is the Berry curvature. Geometrically, ϕ is half the oriented solid angle $\Omega(\mathbf{h})$ subtended by the loop $\mathbf{h}(k_x)$ as seen from the origin. The integral of $\frac{1}{2\pi}F$ over the entire Brillouin zone gives the Chern number: $\frac{1}{2\pi}\oint_{\text{BZ}} F = \nu$. Both ϕ and k_y live on a circle, and from Eq. (7.11b), $\phi(k_y)$ is a map $S^1 \to S^1$ with winding number ν.

At the values of $\phi(k_y) = 0$ or π, the origin is in the plane of the ellipse $\mathbf{h}(k_x)|_{k_y}$, and lies outside or inside the ellipse respectively. Hence there is a zero energy edge state when $\phi(k_y) = \pi$, and no edge state if $\phi(k_y) = 0$ (or 2π). The family of loops as k_y is varied connects these two special cases smoothly. For example, the upper critical momentum k_c

has Berry phase $0 \leq \phi(k_c) < \pi$, while the lower critical momentum k_v has Berry phase $\pi < \phi(k_v) \leq 2\pi$. Thm. 1b says that if an edge state exists, $0 < \phi < \pi$ implies it has energy $E_s > 0$, and $\pi < \phi < 2\pi$ implies $E_s < 0$. Therefore in between $k_c < k_y < k_v$, a gapless (counterclockwise) chiral mode must exist connecting the bulk bands.

For an insulator with Chern number ν, the Berry phase $\phi(k_y)$ goes from 0 to $2\pi\nu$ as k_y is varied from 0 to 2π. Each time the phase $\phi(k_y)$ winds around the circle, $2\pi\alpha \to 2\pi(\alpha + 1)$, a pair of critical momenta $(k_{c\alpha}, k_{v\alpha})$ defines a range in which a chiral mode connects the bulk valence and conduction band, $k_{c\alpha} < k_y < k_{v\alpha}$. This chiral mode is counterclockwise as the phase ϕ increases by 2π. Similarly, there is a clockwise chiral mode as ϕ decreases by 2π. Therefore, the total number of chiral edge modes (counterclockwise − clockwise) is given by the Chern number of the bulk Hamiltonian.

7.5   Discussion

Theorem 1 gives a simple way to compute the spectrum of edge states from properties of the bulk Hamiltonian. The existence of zero-energy edge states is determined by whether or not the ellipse traced by $\mathbf{h}_\parallel$ encloses the origin. Intuitively, the size of the ellipse is a measure of the coupling strength $\mathbf{b}$ between neighboring layers, while the in-plane displacement of the ellipse $\mathbf{b}_\parallel^0$ is a measure of coupling within the layers. From this perspective, Thm. 1a says that an edge state exists if the nearest-layer coupling is 'stronger' than the intra-layer coupling. This is a straightforward extension of the edge states of polyacetylene, a 1D chain with alternating bond strengths $t \neq t'$, which supports an edge state if the chain terminates on the weaker bond. [86]

The geometric argument presented above can also be used to calculate the penetration depth ξ of the surface states:

$$\xi = \frac{a}{2\ln(1/|\lambda|)}. \tag{7.12}$$

a is the distance between layers, λ is the characteristic decay parameter such that the wavefunction decays as $\psi_n \sim \lambda^n$ in the bulk. $|\lambda|$ is the larger of $|\lambda_a|, |\lambda_b|$ [defined in Eq. (7.9)]. $|\lambda|$ is always less than one and is determined by the location of the origin inside the ellipse $\mathbf{h}_\parallel(k_\perp)$. When the origin touches the edge of the ellipse, λ has unit modulus and ξ tends to infinity, indicating a bulk propagating mode. At this point the surface spectrum ends and merges with the bulk bands. Figure 7.3 explains how $|\lambda|$ may be computed from properties of the ellipse $\mathbf{h}_\parallel(k_\perp)$.
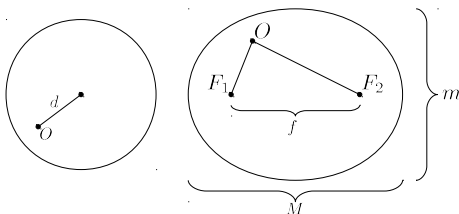
Figure 7.3: Determining the penetration depth from the ellipse $\mathbf{h}_\parallel$. The distances from the foci of the ellipse $\mathbf{h}_\parallel(k_\perp)$ to the origin determine the characteristic decay parameter λ, which in turns gives the penetration depth $\xi = -a/2\ln|\lambda|$. In the case where $\mathbf{h}_\parallel$ traces a circle, $|\lambda| = d/r$, where d is the distance of the origin to the center of the circle, and r is the radius of the circle. In the general case $\mathbf{h}_\parallel$ traces an ellipse, $|\lambda| = \frac{l+\sqrt{l^2-f^2}}{M+m}$, where M and m are the major and minor diameters, $f = \sqrt{M^2 - m^2}$ is the distance between the foci $|F_1F_2|$, and l is the sum of distances from the origin to the two foci $|OF_1| + |OF_2|$.

Chapter 8

Applications of Theorem 1

In this chapter, we illustrate how Theorem 1 may be used the edge state dispersion in various systems.

8.1 Example: graphene

As an illustration of how Thm. 1 can be used to calculate edge state energies, we examine the zigzag edge of graphene. Because the bulk energy bands are degenerate at two inequivalent points in the Brillouin zone, there is no well-defined topological invariant and Thm. 2 does not apply.

Consider the tight-binding model for graphene on a honeycomb lattice with primitive translational vectors $\mathbf{a}_1$ and $\mathbf{a}_2$ taken to be $120°$ apart. The zigzag boundary parallel to either $\mathbf{a}_1$ or $\mathbf{a}_2$ is known to support edge modes, while the armchair boundary parallel to $\mathbf{a}_1 - \mathbf{a}_2$ has no edge modes. Using the reciprocal space coordinates $k_1 = \mathbf{k} \cdot \mathbf{a}_1, k_2 = \mathbf{k} \cdot \mathbf{a}_2$, the tight-binding Hamiltonian takes the form

$$H = t \begin{bmatrix} 0 & 1 + e^{ik_1} + e^{-ik_2} \\ 1 + e^{-ik_1} + e^{ik_2} & 0 \end{bmatrix}, \tag{8.1}$$

written in the (A, B) basis, where A and B are the inequivalent sublattices. The Hamiltonian can be written in terms of the Pauli matrices as $H = \mathbf{h} \cdot \boldsymbol{\sigma}$ with

$$\mathbf{h}(\mathbf{k}) = t(1 + \cos k_1 + \cos k_2, -\sin k_1 + \sin k_2, 0). \tag{8.2}$$

For a zigzag edge parallel to $\mathbf{a}_1$, we examine the curves traced by $\mathbf{h}$ for fixed k_1. [1] The k_2-dependent terms in $\mathbf{h}$ are written as

$$2\mathbf{b}^r \cos k_2 = (t, 0, 0) \cos k_2,$$
$$2\mathbf{b}^i \sin k_2 = (0, t, 0) \sin k_2,$$

---

[1]Despite our notation, the basis vector $\mathbf{a}$ corresponding to $k_\perp$ doesn't have to be perpendicular to the surface, it just has to be a displacement that takes one layer parallel to the surface to the next.

while the remaining k_2-independent terms become

$$\mathbf{b}_\parallel^0 = (t + t\cos k_1, -t\sin k_1, 0), \quad \mathbf{b}_\perp^0 = 0.$$

$\mathbf{h}_\parallel$ lies in the plane spanned by $\mathbf{b}^r$ and $\mathbf{b}^i$, and for this system is a circle in the xy-plane. It encloses the origin only if the magnitude of $\mathbf{b}^0$ is less than t, $i.e.$ when $|1 + e^{ik_1}| < 1$ or equivalently when $2(1 + \cos k_1) < 1$. Thus for $\frac{2\pi}{3} < k_1 < \frac{4\pi}{3}$, $\mathbf{h}_\parallel$ encloses the origin and the system has mid-gap edge modes. According to Thm. 1b, the energies of these edge modes are given by $\pm|\mathbf{b}_\perp^0|$, which is zero. We have shown that the zigzag boundary supports zero energy edge states when $\frac{2\pi}{3} < k_1 < \frac{4\pi}{3}$, in agreement with previous work. [1, 17]

To see why such edge modes do not exist at armchair boundaries, consider the edge parallel to $\mathbf{a}_1 - \mathbf{a}_2$. By rewriting the Hamiltonian in terms of $k_\parallel \equiv k_1 - k_2$ and $k_\perp = k_1$, we can again examine the behavior of $\mathbf{h}_\parallel$ at fixed $k_\parallel$. In this case, it is possible to show that $\mathbf{h}_\parallel$ never encloses the origin, and thus never satisfies the condition for mid-gap edge states.

8.2   Example: $p + ip$ superconductor

We study a $p + ip$ system, which in the weak-pairing phase is characterized by chiral Majorana modes at the edge. [71] We consider a model on a square lattice with p-wave pairing between spinless electrons, shown in Fig. 7.2. The bulk Hamiltonian is given by

$$H(\mathbf{k}) = \begin{bmatrix} -2t(\cos k_x + \cos k_y) - \mu & \Delta_0(\sin k_y + i\sin k_x) \\ \Delta_0(\sin k_y - i\sin k_x) & 2t(\cos k_x + \cos k_y) + \mu \end{bmatrix}, \quad (8.3)$$

where H is written in the $(c_\mathbf{k}, c_{-\mathbf{k}}^\dagger)^T$ basis. The pair potential is given by $\Delta_0(\sin k_y - i\sin k_x)$, where Δ_0 is real. Eq. (8.3) can be expressed as $H = \mathbf{h} \cdot \boldsymbol{\tau}$ for

$$\mathbf{h}(k_x, k_y) = (\Delta_0\sin k_y, -\Delta_0\sin k_x, -2t\cos k_x - 2t\cos k_y - \mu). \quad (8.4)$$

For a system with edges parallel to $\hat{x}$, we examine the ellipses traced by $\mathbf{h}(k_y)$ for fixed values of k_x. Following Eq. (7.3), the k_y-dependence of $\mathbf{h}$ is decomposed as

$$2\mathbf{b}^r \cos k_y = (0, 0, -2t)\cos k_y,$$
$$2\mathbf{b}^i \sin k_y = (\Delta_0, 0, 0)\sin k_y.$$

The remaining k_y-independent term is decomposed as

$$\mathbf{b}_\parallel^0 = (0, 0, -2t\cos k_x - \mu),$$
$$\mathbf{b}_\perp^0 = (0, -\Delta_0\sin k_x, 0).$$

For this model $\mathbf{h}_\parallel(k_y)$, which lies the plane spanned by $\mathbf{b}^r$ and $\mathbf{b}^i$, is an ellipse in the xz-plane. The condition for the ellipse to enclose the origin is $|2t\cos k_x + \mu| < |2t|$, which is only possible for the range of chemical potential $|\mu| < 4|t|$. According to Theorem 1, when this condition is satisfied, the system has mid-gap states at the left edge with energy

$$E_s = \mathbf{b}_\perp^0 \cdot \frac{\mathbf{b}^r \times \mathbf{b}^i}{|\mathbf{b}^r \times \mathbf{b}^i|} = \mathbf{b}_\perp^0 \cdot (-\hat{y})$$
$$= \Delta_0\sin k_x,$$

assuming $t\Delta_0 > 0$. The right edge state energy is given by $-E_s = -\Delta_0 \sin k_x$. The two edge states can become degenerate at $E_s = 0$ at either $k_x = 0$ or π for an appropriate range of μ: the degeneracy occurs at $k_x = 0$ when $-4 < \mu/t < 0$, and at $k_x = \pi$ when $0 < \mu/t < 4$. The bulk gap closes and there is a transition at $\mu/t = 0$ or ± 4.

8.3 Example: 3D topological insulator

In this section we show that the surface states of a strong topological insulator have an odd number of Dirac cones, and derive an effective surface theory. As an example of a topological insulator, we use a model on a cubic lattice: [40]

$$H = v\tau^z \left(\sum_\mu \sigma^\mu \sin k_\mu \right) + \left(M - t \sum_\mu \cos k_\mu \right) \tau^x \tag{8.5}$$

for $\mu = x, y, z$. In the basis of Dirac matrices $\mathbf{\Gamma} = (\tau^z \sigma^x, \tau^z \sigma^y, \tau^z \sigma^z, \tau^x)$, we can write $H = \mathbf{h} \cdot \mathbf{\Gamma}$, with

$$\mathbf{h}(\mathbf{k}) = (v \sin k_x, v \sin k_y, v \sin k_z, m(\mathbf{k})), \tag{8.6}$$

where the "mass" is given by $m(\mathbf{k}) = M - t \sum \cos k_\mu$. (The 'fifth' Dirac matrix is τ^y, but it is never used in this model.) For the (001) surface parallel to $\hat{x}$ and $\hat{y}$, we solve for the edge states as a function of k_x, k_y:

$$\mathbf{h}(k_z)\big|_{k_x,k_y} = (v \sin k_x, v \sin k_y, 0, M - t \cos k_x - t \cos k_y)$$
$$+ (0, 0, 0, -t) \cos k_z + (0, 0, v, 0) \sin k_z$$

which lies on the *34*-plane (in Γ space) displaced by $v(\sin k_x, \sin k_y)$ from the origin. An edge state exists if and only if $|M - t \cos k_x - t \cos k_y| < |t|$ with Dirac cone spectrum $E_s = \pm v \sqrt{\sin^2 k_x + \sin^2 k_y}$.

The ellipse $\mathbf{h}_\parallel(k_z)\big|_{k_x,k_y}$ has one of its diameters stretching from $m(k_x, k_y, 0)$ to $m(k_x, k_y, \pi)$ along the Γ^4 axis. This ellipse encloses the origin if and only if the two endpoints straddles the origin; equivalently, a Dirac cone appears at the surface time-reversal invariant momenta (TRIM) (k_x, k_y) if the mass in the bulk Hamiltonian changes sign: $m(k_x, k_y, 0) m(k_x, k_y, \pi) < 0$. [87]

In this basis the time-reversal operator has the form $\Theta = -i\sigma^y \mathcal{K}$, where $\mathcal{K}$ is the complex conjugation operator. The spatial inversion operator is $\Pi = \Gamma^4 = \tau^x$. At the eight bulk TRIM, the Hamiltonian commutes with the inversion operator: $[H(\mathbf{k}_{\mathrm{TRIM}}), \Pi] = 0$. In fact, H is a multiple of Π:

$$H(\mathbf{k}_{\mathrm{TRIM}}) = m(\mathbf{k}_{\mathrm{TRIM}})\Pi. \tag{8.7}$$

Hence, the sign of the mass determines the parity eigenvalue of the pair of filled states. The strong $\mathbb{Z}_2$ topological invariant is the product of the parity eigenvalues at these TRIM, and hence $\nu_0 = \prod_{\mathrm{TRIM}} \operatorname{sgn} m(\mathbf{k})$. [29] It is clear that the bulk $\mathbb{Z}_2$ invariant dictates whether there are an even or odd number of Dirac cones on the surface. [31, 87]

Generically, all TRI topological insulators written in 4×4 Dirac matrices take on a similar form to (8.5), and most importantly they satisfy (8.7) at the eight TRIM points. Hence it is straightforward to establish the bulk-boundary correspondence for 3D TRI topological insulators.

We now proceed to examine the surface eigenstates following the derivation from Sec. 10.7. When $1 < m/t < 3$, the model is in the strong topological insulating phase with a single Dirac cone at $(k_x, k_y) = (0, 0)$. The surface Hamiltonian is of the form $H_s = (\mathbf{b}_\perp^0 \cdot \boldsymbol{\Gamma}) P_s$ where P_s is the projector of the two surface states: $P_s = \frac{1}{2}(1 - i(-\Gamma^4)\Gamma^3) = \frac{1}{2}(1 + \tau^y \sigma^z)$. To examine the Hamiltonian in the reduced vector space, it is useful to apply a unitary transformation $\bar{H} = UHU^{-1}$ where $U = \exp(-i\frac{\pi}{4}\tau^x)$. The projector becomes diagonal in the new basis

$$\bar{P}_s = U P_s U^{-1} = \frac{1}{2}(1 + \tau^z \sigma^z),$$

projecting onto the first and last row. The "edge energy" term $\mathbf{b}_\perp^0 \cdot \boldsymbol{\Gamma}$ transforms as

$$\bar{V}_\perp^0 = U(\mathbf{b}_\perp^0 \cdot \boldsymbol{\Gamma})U^{-1} = -v\tau^y(\sigma^x \sin k_x + \sigma^y \sin k_y)$$
$$\approx -v\tau^y(\sigma^x k_x + \sigma^y k_y).$$

Since $\bar{P}_s$ is diagonal with entries $(1, 0, 0, 1)$, it suffices to examine only the four corners of $\bar{V}_\perp^0$. The effective surface Hamiltonian can be computed: [2]

$$\bar{H}_s = \bar{V}_\perp^0 \bar{P}_s \approx v \begin{bmatrix} 0 & k_y + ik_x \\ k_y - ik_x & 0 \end{bmatrix}$$
$$= v(\boldsymbol{\sigma} \times \mathbf{k}) \cdot \hat{z}. \tag{8.8}$$

The basis of the surface Hamiltonian $\bar{H}_s$ is, in terms of the basis of H, $(1, 0, i, 0)^T/\sqrt{2}$ and $(0, 1, 0, i)^T/\sqrt{2}$ (The first and last columns of $U^\dagger$). The spin degrees of freedom ($\boldsymbol{\sigma}$) and the orbital degree of freedom ($\boldsymbol{\tau}$) are entangled in the surface states.

8.4 Continuum Hamiltonians quadratic in momentum

The bulk-edge correspondence stated in Sec. 7.2 may also be extended to Hamiltonians in the continuum. Given a translationally invariant Dirac Hamiltonian quadratic in momentum $\mathbf{p} = -i\nabla$, of the form:

$$H(p; \mathbf{p}_\parallel) = C^0(\mathbf{p}_\parallel) + C^1(\mathbf{p}_\parallel)p + C^2(\mathbf{p}_\parallel)p^2$$
$$= \left[\mathbf{c}^0(\mathbf{p}_\parallel) + \mathbf{c}^1(\mathbf{p}_\parallel)p + \mathbf{c}^2(\mathbf{p}_\parallel)p^2\right] \cdot \boldsymbol{\Gamma} \tag{8.9}$$

where $\mathbf{p}_\parallel$ and p are, respectively, the momentum parallel and perpendicular to the edge/surface. For a fixed momentum $\mathbf{p}_\parallel$, the vector

$$\mathbf{h}(p)\big|_{\mathbf{p}_\parallel} = \mathbf{c}^0 + \mathbf{c}^1 p + \mathbf{c}^2 p^2 \tag{8.10}$$

---

[2]The Rashba coupling results from our choice of U. It is also possible to arrive at the surface Hamiltonian of the form $\boldsymbol{\sigma} \cdot \mathbf{k}$.

traces a parabola. This parabola lies on some 2D plane spanned by $\mathbf{c}^1$ and $\mathbf{c}^2$, and we can always decompose $\mathbf{c}^0$ and $\mathbf{h}$ into in-plane and out-of-plane components: $\mathbf{c}^0 = \mathbf{c}^0_\perp + \mathbf{c}^0_\parallel$ and $\mathbf{h}(p) = \mathbf{c}^0_\perp + \mathbf{h}_\parallel(p)$. In this section we state the main theorem:

Theorem 3a. *An edge state (with zero Dirichlet or Neumann boundary condition) exists if and only if the origin is within the concave side of the parabola $\mathbf{h}_\parallel(p)$.*

Theorem 3b. *The energy of the edge state is given by the distance of the plane to the origin, i.e. $E_s = \pm|\mathbf{c}^0_\perp|$. When the gamma matrices are the Pauli matrices, the left edge (semi-infinite slab with $n > 0$) energy is given by: $E_s = \mathbf{c}^0 \cdot \frac{\mathbf{c}^1 \times \mathbf{c}^2}{|\mathbf{c}^1 \times \mathbf{c}^2|}$.*

The proof of Theorem 3 is given in Section 10.8.

8.4.1   Discussion

The proof of Thm. 3 uses the ansatz $\psi(x) = u_a e^{i\kappa_a x} + u_b e^{i\kappa_b x}$ and derives the condition when $\mathrm{Im}\,\kappa_{a,b} > 0$ for edge states. Physically, $\xi = (\mathrm{Im}\,\kappa)^{-1}$ gives the penetration depth of the edge modes. We may think of the continuum as a limiting case of the lattice as the lattice spacing a goes to zero. The ellipse $\mathbf{h}_\parallel$ becomes a parabola for vanishing a as the quantities $\mathbf{c}^0 = \mathbf{b}^0 + 2\mathbf{b}^r$, $\mathbf{c}^1 = 2\mathbf{b}^i a$, $\mathbf{c}^2 = \mathbf{b}^r a^2$ are held constant. Theorem 2 also extends to the continuum case as the paraboloid $\mathbf{h}(k_x, k_y)$ determines the number of chiral edge states.

In addition to Dirichlet and Neumann boundary conditions, there is also a mixed type with $\psi'(0) = \eta\psi(0)$ for a positive number η. The origin of this boundary condition comes from requiring the wavefunction outside $(x < 0)$ to satisfy $H_{\mathrm{vac}} = W + \frac{p^2}{2m}$, where $W > E_s$ is the work function. Our analysis and result holds even for this boundary condition.

Notice that the quadratic term $C^2 p^2$ is crucial for the existence of edge states. Without it, the polynomial (10.21) will be quadratic and there can only be one solution for κ in the upper half plane. The form of the solution $\psi = u e^{i\kappa x}$ makes it impossible to satisfy either type of boundary condition.

In the lattice model, we can compute the edge spectrum only for certain surfaces because of the nearest-layer requirement. For example, we can only compute the {100}, {110} and {111} surface dispersion of the TI model on a cubic lattice. In the continuum case when the Hamiltonian is bilinear in momentum, any surface cut will still yield a Hamiltonian quadratic in $p_\perp$. Consequently, we can compute the surface excitation spectrum and wavefunctions of the Hamiltonian for all linear surfaces.

8.4.2   Example: $p + ip$ superconductor

We use the simplest model of a $p + ip$ superconductor: [71]

$$H(p_x, p_y) = \begin{bmatrix} \frac{p^2}{2m^*} - \mu & \Delta_0(p_x - ip_y) \\ \Delta_0(p_x + ip_y) & \mu - \frac{p^2}{2m^*} \end{bmatrix}. \tag{8.11}$$

Equivalently, with $H(\mathbf{p}) = \mathbf{h}(\mathbf{p})\cdot\boldsymbol{\tau}$, where τ^i are the Pauli matrices in Bogoliubov-de Gennes (BdG) space:

$$\mathbf{h}(\mathbf{p}) = \left(\Delta_0 p_x, \Delta_0 p_y, \frac{p^2}{2m^*} - \mu\right). \tag{8.12}$$

This model is isotropic, and without loss of generality, we take a semi-infinite plane $x \geq 0$ with $\hat{y}$ parallel to the edge. At a fixed p_y, the $\mathbf{h}$ vector becomes:

$$\mathbf{h}(p_x) = \left(0, \Delta_0 p_y, \frac{p_y^2}{2m^*} - \mu\right) + (\Delta_0, 0, 0)p_x + \left(0, 0, \frac{1}{2m^*}\right)p_x^2 \tag{8.13}$$

which lies in the xz-plane with $y = \Delta_0 p_y$. The parabola is concave towards the $+\hat{z}$ direction, and hence an edge state exists if and only if $\frac{p_y^2}{2m^*} - \mu < 0$. Edge states can only exist when μ is positive, or in other words in the 'weak pairing phase' of $p + ip$ superconductors.

The edge state energy dispersion is given by Thm. 3b.

$$\begin{aligned} E_s &= \mathbf{c}^0 \cdot \frac{\mathbf{c}^1 \times \mathbf{c}^2}{|\mathbf{c}^1 \times \mathbf{c}^2|} \\ &= \Delta_0 p_y \hat{y} \cdot (\hat{x} \times \hat{z}) \\ &= -\Delta_0 p_y. \end{aligned}$$

Referring to Eq. (10.17), the edge state wavefunction is given by the projector $P_s = \frac{1}{2}(1 - i\tau^x\tau^z) = \frac{1}{2}(1 - \tau^y)$. Hence the edge states parallel to the y-axis are eigenstates of τ^y.

8.5 Outlook

In this part, we provided two main results. Theorem 1 gives a general prescription for finding edge states of Dirac Hamiltonians (with nearest-layer coupling) on a lattice. Its range of applicability includes "accidental edge states" which may not be topologically protected, such as boron nitride. Theorem 2 relates the bulk Chern number of a 2D insulator to the number of chiral edge modes. This establishes the bulk-boundary correspondence for a class of quantum Hall insulators.

For 3D time-reversal invariant insulators, we demonstrated in Sec. 8.3 how the $\mathbb{Z}_2$ strong topological invariant determines whether there is an odd or even number of Dirac cones in the surface spectrum. Although we have used a specific TI model in the example, the argument is easily generalizable for all TRI Dirac Hamiltonians.

This work can be extended beyond quantum Hall insulators (class A) and TRI topological insulators (class AII) to other insulators within the Altand and Zirnbauer classification. [6, 38] The periodic table of topological insulators and superconductors provide an exhaustive topological classification of non-interacting electronic systems. [79, 52] As there are model Dirac Hamiltonians [47, 31, 40, 76] in each class, our work provides the machinery to relate the bulk topological invariants [52] to the surface properties [79] of these systems.

Chapter 9

Proof by Green's functions

It is difficult to study a system with edges because of the broken translational invariance. We begin by writing the Green's function for an easier problem: a periodic system with no boundary. [33] The full translational invariance allows us to work in momentum space, reducing the dimension of the Hamiltonian in momentum space. Next, the geometry of the system is changed from a periodic to an open system by subtracting all interactions between a particular pair of nearest neighbors. We use the Dyson equation to calculate the Green's function for the open geometry and show that there are poles – and thus bound states – at mid-gap energies. The form of the potential required to cut the periodic system greatly reduces the degrees of freedom in the problem and enables an analytic solution.

We prove Theorem 1 for the case of 2×2 Dirac Hamiltonians, which can be decomposed in terms of the Pauli matrices σ^i. For higher dimensional Hamiltonians, it is always possible to find three gamma matrices Γ^i that whose sub-blocks are the Pauli matrices, $e.g.$ $\tau^z \sigma^x, \tau^z \sigma^y, \tau^z \sigma^z$. A suitable unitary transformation rotates the Hamiltonian so that it is a linear combination of these three gamma matrices, and the arguments of this section apply to each sub-block.

9.1 Bulk Green's function

We prove Theorem 1 for 2×2 Hamiltonians, which can be expressed in the following form:

$$H(k) = E_k \begin{bmatrix} \cos\theta & \sin\theta \, e^{-i\phi} \\ \sin\theta \, e^{i\phi} & -\cos\theta \end{bmatrix} \tag{9.1}$$

Decomposing H into the Pauli matrices σ^i gives $H = \mathbf{h} \cdot \boldsymbol{\sigma}$ for

$$\mathbf{h} = E_k(\sin\theta\cos\phi, \sin\theta\sin\phi, \cos\theta) \tag{9.2}$$

The eigenstates are given by

$$|\psi_-\rangle = \begin{pmatrix} \sin\frac{\theta}{2} \\ -\cos\frac{\theta}{2}e^{i\phi} \end{pmatrix}$$
$$|\psi_+\rangle = \begin{pmatrix} \cos\frac{\theta}{2} \\ \sin\frac{\theta}{2}e^{i\phi} \end{pmatrix} \tag{9.3}$$

To express $\mathbf{h}$ in terms of the parameters defined in Section 7.2, we assume $\mathbf{b}^r$ and $\mathbf{b}^i$ lie along $\hat{x}$ and $\hat{y}$ respectively, with $\mathbf{b}_\perp^0$ along $\hat{z}$. The Hamiltonian takes the form

$$E_k \sin\theta\cos\phi\ \hat{x} = 2\mathbf{b}^r\cos k + (\mathbf{b}_\parallel^0 \cdot \hat{x})\ \hat{x}$$
$$E_k \sin\theta\sin\phi\ \hat{y} = 2\mathbf{b}^i\sin k + (\mathbf{b}_\parallel^0 \cdot \hat{y})\ \hat{y} \tag{9.4}$$
$$E_k \cos\theta\ \hat{z} = \mathbf{b}_\perp^0$$

Here $\mathbf{h}_\parallel$ lies in the xy-plane. For the remainder of this section, we will use the notation $b_r = |\mathbf{b}^r|$ and $b_i = |\mathbf{b}^i|$. Note that any Hamiltonian may be brought to this form by an appropriate gauge transformation.

The first step in calculating the edge mode energies is to write the Green's function for the fully periodic system. Utilizing the full translational invariance, we work for now in the momentum representation. The $\alpha\beta$ matrix element of the bulk Green's function is given by

$$G_0^{\alpha\beta}(E;k) = \sum_i \frac{|\psi_i\rangle_\alpha \langle\psi_i|_\beta}{E - E_i} \tag{9.5}$$

where i sums over the energy eigenstates of $\mathcal{H}$. The four matrix elements are given by

$$G_0^{11}(E;k) = \frac{E + E_k\cos\theta}{E^2 - E_k^2}, \tag{9.6a}$$

$$G_0^{22}(E;k) = \frac{E - E_k\cos\theta}{E^2 - E_k^2}, \tag{9.6b}$$

$$G_0^{12}(E;k) = E_k\frac{\sin\theta\cos\phi - i\sin\theta\sin\phi}{E^2 - E_k^2}, \tag{9.6c}$$

$$G_0^{21}(E;k) = E_k\frac{\sin\theta\cos\phi + i\sin\theta\sin\phi}{E^2 - E_k^2}. \tag{9.6d}$$

In order to include the effects of a boundary that is localized in real space, the bulk Green's function is written in real space via a Fourier transformation.

$$G_0(E;y) = \begin{bmatrix} B^0 & B^\dagger & \cdots & & B \\ B & B^0 & B^\dagger & & \\ \vdots & B & B^0 & B^\dagger & \\ & & B & B^0 \\ B^\dagger & & & & \ddots \end{bmatrix} \tag{9.7}$$

for

$$B^0 = \int \frac{dk}{2\pi} iG_0(E; k), \; B = \int \frac{dk}{2\pi} e^{ik} G_0(E; k). \tag{9.8}$$

There are of course more non-zero matrix elements, corresponding to the mixing of matrix elements separated by more than one lattice constant. However, for systems with nearest-neighbor interaction, the matrix elements contained in B^0 and B are the only ones needed to prove the existence of zero energy states.

9.2   Green's function of the open system

Next we write an expression V that deletes the coupling terms to create a system with edges. In a system with nearest-layer interactions, the only non-zero matrix elements are those between a single pair of neighboring layers:

$$V = \begin{bmatrix} 0 & \cdots & & V_b \\ \vdots & 0 & & \\ & & \ddots & \\ V_b^{\dagger} & & & 0 \end{bmatrix}. \tag{9.9}$$

$V_b = -\mathbf{b} \cdot \mathbf{\Gamma}$, and for the Hamiltonian described in Eq. (9.4) takes the form

$$V_b = \begin{bmatrix} 0 & -b_r - b_i \\ -b_r + b_i & 0 \end{bmatrix}. \tag{9.10}$$

We are now ready to compute the Green's function for the open system. The Dyson equation gives an exact expression for the open Green's function G in terms of the periodic Green's function G_0 and the cuts V needed to take the system from one geometry to the other:

$$G(E; y) = (I - G_0(E; y)V)^{-1} G_0(E; y). \tag{9.11}$$

Substituting Eq. (9.9) and (9.7) into Eq. (9.11) gives the following condition for an edge state wavevector u:

$$(1 - G_0 V)u = \begin{bmatrix} I - BV_b^{\dagger} & & & & -B^0 V_b \\ & I & & & \\ \vdots & & \ddots & & \vdots \\ & & & I & \\ -B^0 V_b^{\dagger} & & & & I - B^{\dagger} V_b \end{bmatrix} u = 0. \tag{9.12}$$

The ellipses indicate the only non-zero sub-blocks: the first and last columns, and copies of the identity along the diagonal.

9.3 Existence and spectrum of edge modes

Since an edge state wavevector u has non-zero components in the sub-block corresponding to one of the edges, Eq. (9.12) can be satisfied in two ways. There is an edge mode on the left edge when the first two columns of Eq. (9.12) are linearly dependent, and on the right edge when the last two columns are linearly dependent. Recalling the expressions for the bulk Green's functions, Eq. (9.6), we introduce some notation for the open Green's function:

$$a_0 = \int \frac{dk}{2\pi} \frac{E}{E^2 - E_k^2}, \tag{9.13a}$$

$$a_x = \int \frac{dk}{2\pi} \frac{E_k \sin\theta \cos\phi}{E^2 - E_k^2}, \tag{9.13b}$$

$$a_y = \int \frac{dk}{2\pi} \frac{E_k \sin\theta \sin\phi}{E^2 - E_k^2}, \tag{9.13c}$$

$$a_z = \int \frac{dk}{2\pi} \frac{E_k \cos\theta}{E^2 - E_k^2}. \tag{9.13d}$$

$c_0 = \int \frac{dk}{2\pi} e^{ik} \frac{E}{E^2 - E_k^2}$, and similar for c_x, c_y, and c_z. Let us first examine the conditions required for a left edge mode. Collapsing Eq. (9.12) to the subspace corresponding to the two edges, the first two columns can be written as

$$L_1 = \begin{bmatrix} 1 + (b_r + b_i)(c_x - ic_y) \\ (b_r + b_i)(c_0 - c_z) \\ (b_r + b_i)(a_x - ia_y) \\ (b_r + b_i)(a_0 - a_z) \end{bmatrix}, \tag{9.14}$$

$$L_2 = \begin{bmatrix} (b_r - b_i)(c_0 + c_z) \\ 1 + (b_r - b_i)(c_x + ic_y) \\ (b_r - b_i)(a_0 + a_z) \\ (b_r - b_i)(a_x + ia_y) \end{bmatrix}. \tag{9.15}$$

Now we examine the conditions required for the system to have a left edge state, *i.e.* when the columns L_1 and L_2 are linearly dependent. This is done by writing L_1 and L_2 as a 4×2 matrix M and requiring that the determinant of any 2×2 sub-block vanish. This constraint takes on the following form for the sub-blocks of M created by the bottom two rows, the top two rows, and the second and fourth rows, respectively:

$$0 = (b_r^2 - b_i^2)(a_x^2 + a_y^2 - a_0^2 + a_z^2), \tag{9.16a}$$

$$0 = 1 + 2(b_r c_x - ib_i c_y)$$
$$+ (b_r^2 - b_i^2)(c_x^2 + c_y^2 - c_0^2 + c_z^2), \tag{9.16b}$$

$$0 = (b_r^2 - b_i^2)(c_0 - c_z)(a_x + ia_y)$$
$$- (b_r^2 - b_i^2)(c_x + ic_y)(a_0 - a_z) - (b_r + b_i)(a_0 - a_z). \tag{9.16c}$$

The conditions are equivalent to $B^0 V_b^\dagger u_L = 0$ and $(I - BV_b^\dagger)u_L = 0$, which together require $\text{Det}\left[B^0\right] = 0$. To see this, note that although the first condition is satisfied when either $\text{Det}\left[B^0\right] = 0$ or $V_b^\dagger u_L = 0$, the second case cannot satisfy $(I - BV_b^\dagger)u_L = 0$.

9.4   Constraints on $\mathbf{h}_\parallel$ and E^2

We begin by showing that

$$\text{Det}\left[B^0\right] = a_0^2 - a_x^2 - a_y^2 - a_z^2 \tag{9.17}$$

is zero if and only if $\mathbf{h}_\parallel$ encloses the origin and the edge state energy is given by $E = \pm|\mathbf{b}_\perp^0|$. For a geometric view of the variables a_0, a_+, *etc.*, note that $E_k(\sin\theta\cos\phi, \sin\theta\sin\phi)$ are the (x, y) coordinates of $\mathbf{h}_\parallel$, and $E_k\cos\theta = \mathbf{b}_\perp^0 \cdot \hat{z}$. E_k^2 is given by $|\mathbf{b}_\perp^0|^2 + |\mathbf{h}_\parallel|^2$, and $E^2 - E_k^2 < 0$ for a mid-gap state. We examine two cases, when $\mathbf{h}_\parallel$ encloses the origin and when it does not.

Suppose the ellipse does not enclose the origin. Let $\mathbf{h}_\parallel^{\min}$ be the point on the ellipse $\mathbf{h}_\parallel$ closest to the origin. Because the ellipse is convex and does not contain the origin, it must lie in the half of the plane (spanned by $\mathbf{b}^r, \mathbf{b}^i$) for which $\mathbf{r} \cdot \mathbf{h}_\parallel^{\min}$ is positive. In other words, $\mathbf{h}_\parallel(k) \cdot \mathbf{h}_\parallel^{\min}$ is positive definite. Moreover, $\mathbf{h}_\parallel(k) \cdot \mathbf{h}_\parallel^{\min} \geq |\mathbf{h}_\parallel^{\min}|^2$ from its definition. The Cauchy-Schwarz inequality says that

$$\left|(a_x\hat{x} + a_y\hat{y}) \cdot \mathbf{h}_\parallel^{\min}\right| \leq |a_x\hat{x} + a_y\hat{y}|\,|\mathbf{h}_\parallel^{\min}|, \tag{9.18}$$

therefore

$$|a_x\hat{x} + a_y\hat{y}| \geq \frac{1}{|\mathbf{h}_\parallel^{\min}|} \int \frac{dk}{2\pi} \frac{\mathbf{h}_\parallel \cdot \mathbf{h}_\parallel^{\min}}{E_k^2 - E^2}$$

$$\geq \frac{1}{|\mathbf{h}_\parallel^{\min}|} \int \frac{dk}{2\pi} \frac{|\mathbf{h}_\parallel^{\min}|^2}{E_k^2 - E^2}. \tag{9.19}$$

This sets an upper bound to $\text{Det}\left[B^0\right]$:

$$a_0^2 - a_z^2 - a_x^2 - a_y^2 \leq \left(E^2 - |\mathbf{b}_\perp^0|^2\right)\mathcal{I}^2 - |\mathbf{h}_\parallel^{\min}|^2\mathcal{I}^2, \tag{9.20}$$

where $\mathcal{I} = \int \frac{dk}{2\pi} \frac{1}{E_k^2 - E^2}$. Since $|\mathbf{b}_\perp^0|^2 + |\mathbf{h}_\parallel^{\min}|^2 > E^2$, the expression is always negative and never zero. Hence no edge states can exist when the ellipse $\mathbf{h}_\parallel$ fails to enclose the origin.

Now we consider the case when the ellipse $\mathbf{h}_\parallel$ encloses the origin and show that an edge state exists only when $E^2 = |\mathbf{b}_\perp^0|^2$. First, when $E^2 = |\mathbf{b}_\perp^0|^2$, the integrals a_x and a_y are both zero. Because $E = |\mathbf{b}_\perp^0|$, $a_0^2 - a_z^2 = 0$ and the determinant is zero.

To see why $a_x = a_y = 0$ in this case, note that the denominator of $\mathcal{I}$ becomes $|\mathbf{h}_\parallel|^2$, and we can express the conditions geometrically. Here we use Gauss's law in 2D to show that $\int dk \frac{\mathbf{h}_\parallel}{|\mathbf{h}_\parallel|^2}$ is zero if and only if $\mathbf{h}_\parallel$ encloses the origin. We can visualize the expression from an electrostatics point of view: for a charged ellipse in 2D with a charge distribution $\int dk\,\delta(\mathbf{r} - \mathbf{h}_\parallel)$, the electric field ($\propto \frac{1}{r}$ in 2D) at the origin is given by $\int dk \frac{\mathbf{h}_\parallel}{|\mathbf{h}_\parallel|^2}$. Analogous to a uniformly charged circle, the charges are distributed such that the electric field is vanishing in the interior but nonzero in the exterior:

$$a_x\hat{x} + a_y\hat{y} = -\int dk \frac{\mathbf{h}_\parallel}{|\mathbf{h}_\parallel|^2} = 0. \tag{9.21}$$

Now we show that $\text{Det}\left[B^0\right] = 0$ is not satisfied for any other value of E^2. If $E^2 < |\mathbf{b}_\perp^0|^2$ then $|E| < |\mathbf{b}_\perp^0| = |E_k \sin\theta\sin\phi|$. It follows that $a_0^2 - a_z^2 = (E^2 - |\mathbf{b}_\perp^0|^2)\mathcal{I}^2 < 0$, hence there are no edge states.

If $E^2 > |\mathbf{b}_\perp^0|^2$, we let $E^2 = \epsilon^2 + |\mathbf{b}_\perp^0|^2$, such that $E_k^2 - E^2 = |\mathbf{h}_\parallel|^2 - \epsilon^2 > 0$. a_0 and a_z can be written as:

$$-a_0 = \int \frac{dk}{2\pi} \frac{E}{|\mathbf{h}_\parallel|^2 - \epsilon^2}, \tag{9.22a}$$

$$-a_z = \int \frac{dk}{2\pi} \frac{|\mathbf{b}_\perp^0|}{|\mathbf{h}_\parallel|^2 - \epsilon^2}, \tag{9.22b}$$

which combine to give:

$$a_0^2 - a_z^2 = (|E^2 - \mathbf{b}_\perp^0|^2)\mathcal{I}^2 = \epsilon^2\mathcal{I}^2. \tag{9.22c}$$

For a_x and a_y, we use the manipulation

$$\frac{1}{|\mathbf{h}_\parallel|^2 - \epsilon^2} - \frac{1}{|\mathbf{h}_\parallel|^2} = \frac{\epsilon^2}{(|\mathbf{h}_\parallel|^2 - \epsilon^2)|\mathbf{h}_\parallel|^2}$$

to get:

$$-a_x\hat{x} - a_y\hat{y} = \epsilon\int \frac{dk}{2\pi} \frac{\mathbf{h}_\parallel\epsilon}{(|\mathbf{h}_\parallel|^2 - \epsilon^2)|\mathbf{h}_\parallel|^2}. \tag{9.22d}$$

By the triangle inequality: $\left|\int dk\,\mathbf{u}(k)\right| \le \int dk\,|\mathbf{u}(k)|$, we can put an upper bound

$$
\begin{aligned}
|a_x\hat{x} + a_y\hat{y}| &\le \epsilon\int \frac{dk}{2\pi} \frac{|\mathbf{h}_\parallel|\epsilon}{(|\mathbf{h}_\parallel|^2 - \epsilon^2)|\mathbf{h}_\parallel|^2} \\
&= \epsilon\int \frac{dk}{2\pi} \frac{\epsilon}{(|\mathbf{h}_\parallel|^2 - \epsilon^2)|\mathbf{h}_\parallel|} \\
&< \epsilon\int \frac{dk}{2\pi} \frac{1}{(|\mathbf{h}_\parallel|^2 - \epsilon^2)} \\
&= \epsilon\mathcal{I}. \tag{9.23}
\end{aligned}
$$

We have used the fact that $|\mathbf{h}_\parallel| > \epsilon$ to go from the second to third line. This implies $a_x^2 + a_y^2 < \epsilon^2\mathcal{I}^2$ and sets a lower bound to Eq. (9.17): $a_0^2 - a_z^2 - a_x^2 - a_y^2 > 0$ for $|E| > |\mathbf{b}_\perp^0|$.

Hence we have shown that $\text{Det}\left[B^0\right] = 0$ if and only if $E^2 = |\mathbf{b}_\perp^0|$ and the ellipse $\mathbf{h}_\parallel$ encloses the origin.

Turning now to the second constraint, Eq. (9.16b), we note that $E = \pm|\mathbf{b}_\perp^0|$ implies that $c_0^2 = c_z^2$. In the following, we use the fact that $c_x = -ic_y$. Substituting this into Eq. (9.16b) gives the constraint $1 + 2(b_r c_x - ib_i c_y) = 0$, which may be expressed as

$$1 - 2\int \frac{dk}{2\pi} e^{ik} \frac{\mathbf{h}_\parallel \cdot \mathbf{b}^*}{|\mathbf{h}_\parallel|^2} = 0. \tag{9.24}$$

In order to satisfy Eq. (9.16a) and Eq. (9.16b) simultaneously, Eq. (9.24) must be true if and only if $\mathbf{h}_\parallel$ encloses the origin. This can be shown for an arbitrary ellipse centered at $\mathbf{b}_\parallel^0$ and with semimajor and semiminor axes given by $2\mathbf{b}^r$ and $2\mathbf{b}^i$.

9.5 Sign of the energy

The final constraint, Eq. (9.16c), determines the sign of the edge state energy. Note that the first two terms vanish because $a_x = a_y = 0$ and $c_x = -ic_y$. Getting rid of the remaining term requires choosing a particular sign for the energy. The condition is satisfied with the choice $a_0 = a_z$.

The constraints for the left edge can be summarized as

1a. $E = +\mathbf{b}_\perp^0 \cdot \hat{z}$

1b. $1 + 2(b_r c_x - ib_i c_y) = 0$.

A similar calculation for the right edge, using the last two columns of Eq. (9.12), gives the following conditions:

2a. $E = -\mathbf{b}_\perp^0 \cdot \hat{z}$

2b. $1 + 2(b_r c_x + ib_i c_y) = 0$.

Condition 2b. can be expressed as $1 - 2\int \frac{dk}{2\pi} e^{-ik}\frac{\mathbf{h}_\parallel \cdot \mathbf{b}}{|\mathbf{h}_\parallel|^2} = 0$. Hence it is also satisfied when $\mathbf{h}_\parallel$ encloses the origin, but with opposite orientation as for the left edge. The conditions for edge modes are now equivalent to two statements:

1. The function $\mathbf{h}_\parallel$ must enclose the origin,

2. The energy is given by $E = \pm\mathbf{b}_\perp^0 \cdot \hat{z}$, with the sign determined by the orientation of loop $\mathbf{h}_\parallel$.

We have succeeded in analytically deriving the condition for the $2L \times 2L$ matrix representing the Hamiltonian for an open system to have zero eigenvalues. The power of the method lies in the fact that V has non-zero matrix elements only in the 4×4 subspace of electron operators at the two edges. Thus the effect of the boundary can be seen by examining the 4×4 subspace, which can be handled analytically.

Chapter 10

Proof by transfer matrices

In this section, we prove Theorem 1 for a hard-edge at a fixed $\mathbf{k}_\parallel$. We begin by defining a new function $\boldsymbol{\beta}$ (which is like a complex extension of $\mathbf{h}$), and the form of our edge states.

In the Hamiltonian (7.1), $\mathbf{b} \cdot \boldsymbol{\Gamma}, \mathbf{b}^0 \cdot \boldsymbol{\Gamma}, \mathbf{b}^* \cdot \boldsymbol{\Gamma}$ are the hopping matrices from the previous, same, and next layers respectively. We consider a semi-infinite system where the layers are labeled by positive integers with $n = 1$ denoting the layer at the surface. Hence we ignore the terms $\Psi_1^\dagger \Psi_0$ and $\Psi_0^\dagger \Psi_1$ in considering our semi-infinite system. Consequently, an excitation $\psi^\dagger = \sum_n \Psi_n^\dagger \psi_n$ of the Hamiltonian (7.1) satisfies the following properties:

$$\mathbf{b} \cdot \boldsymbol{\Gamma}\psi_{n-1} + \mathbf{b}^0 \cdot \boldsymbol{\Gamma}\psi_n + \mathbf{b}^* \cdot \boldsymbol{\Gamma}\psi_{n+1} = E\psi_n \qquad n \geq 1, \qquad (10.1a)$$

$$\psi_0 = 0. \qquad (10.1b)$$

An edge state ψ is one for which ψ_n is exponentially decreasing as a function of n. Due to the translational invariance in the bulk, we use the ansatz

$$\psi_n = \sum_\mu u_\mu \lambda_\mu^n \qquad (10.2)$$

in our solutions. [56] [1] An edge solution requires that $|\lambda_\mu| < 1$ for all μ and that $\sum_\mu u_\mu = 0$.

For each decaying mode (λ, u) we have: [2]

$$\lambda \left[\boldsymbol{\beta}(\lambda) \cdot \boldsymbol{\Gamma} - E \right] u = 0, \qquad (10.3)$$

where we have defined

$$\boldsymbol{\beta}(\lambda) \equiv \lambda^{-1}\mathbf{b} + \mathbf{b}^0 + \lambda\mathbf{b}^*. \qquad (10.4)$$

Notice that when λ has unit modulus, we recover the Bloch equation for the bulk (propagating) modes of the system:

$$\boldsymbol{\beta}\left(e^{ik_\perp}\right) = \mathbf{h}(k_\perp). \qquad (10.5)$$

---

[1] A solution of the form $u_\mu n\lambda_\mu^{n-1}$ is also possible, when λ_μ is a double root of (10.6). In such situation, we can tackle the problem as a limiting case of two roots approaching each other: $\lambda_\mu' \to \lambda_\mu$.

[2] We cannot cross off λ on both sides because $\lambda = 0$ is a valid solution when $Bu_\mu = 0$.

Hence we need to find an energy E and a set of λ's all within the unit circle, such that their corresponding "null vector" u defined by (10.3) sum to zero [Eq. (10.1b)].

The outline of the proof is as follows. First, we will derive the particle-hole relationship between left edge and right edge modes. Second, we will establish the algebraic relations between the λ's and E of an edge state [Eq. (10.8)]. Third, we find complex functions $L, \bar{L}$ which represents the ellipse traced out by $\boldsymbol{\beta}(e^{ik})$. Next, we will show (assuming an edge state exists) that the energy of an edge state is given by the displacement of the plane of ellipse. We then proceed to prove Thm. 1a, the condition which governs the existence of an edge state (*i.e.* when all $|\lambda_\mu| < 1$). Finally, we will compute the edge states projectors [Eq. (10.15)] and determine the sign of the edge state energies, which completes the proof for Thm. 1b.

10.1   Relation between left-right boundaries

Lemma. *For every left edge state with energy E, there is a corresponding right edge state with energy $-E$, and vice versa.*

The recursion relation (10.1a) and boundary condition (10.1b) describe a semi-infinite system with a "left" edge. We can write a similar system for the "right" edge simply changing the condition in (10.1a) to $n \leq -1$ xor swapping $\mathbf{b}$ with $\mathbf{b}^*$ in the equation. The first transformation amounts to finding a set of λ's outside the unit circle, *i.e.* $|\lambda_\mu| > 1$, such that the edge wavefunction ψ_n decays with decreasing n. The second transformation is equivalent to taking the complex conjugate of $\mathbf{b}$, and the two transformation are the same owing to the fact that $\boldsymbol{\beta}^*(\lambda) = \boldsymbol{\beta}(1/\lambda^*)$.

When the gamma matrices are the Pauli matrices, there is a charge conjugation operator $C = -i\sigma^y \mathcal{K}$ which takes $\mathbf{b} \cdot \boldsymbol{\sigma} \to -\mathbf{b}^* \cdot \boldsymbol{\sigma}$, where $\mathcal{K}$ is the complex conjugation operator. Since $C\boldsymbol{\beta}(\lambda) \cdot \boldsymbol{\sigma} C^{-1} = -\boldsymbol{\beta}^*(\lambda^*) \cdot \boldsymbol{\sigma}$, C turns a left edge state with energy E into a right edge state with energy $-E$ and vice versa.

When the Dirac matrices are larger then 2×2, such a C operator still exists, as it is always possible to find an antiunitary operator which flips the sign of three of the gamma matrices. This operator C will depend on what $\mathbf{b}$ and $\mathbf{b}^0$ are, meaning that C is a function of $\mathbf{k}_\parallel$, making it a non-local operator. However, the conclusion remains the same.

For the remainder of the proof, we will only be focused on left edge states.

10.2   Algebraic relation between λ_a, λ_b and E

For any E, there are (at most) four possible λ's satisfying (10.3), evident from squaring $\lambda\boldsymbol{\beta}(\lambda) \cdot \boldsymbol{\Gamma}$ to get the quartic equation

$$\lambda\boldsymbol{\beta}(\lambda) \cdot \lambda\boldsymbol{\beta}(\lambda) - E^2\lambda^2 = 0. \tag{10.6}$$

Note that if λ is a root to this equation, then so is $1/\lambda^*$. Hence there can be at most two solutions of for λ within the unit circle, which we call λ_a and λ_b.

The edge wavefunction takes the form $\psi_n = u_a\lambda_a^n + u_b\lambda_b^n$ with $u_a = -u_b$ to satisfy the hard-edge boundary condition (10.1b), where the coefficient u_a is a (right) null vector of

the matrix $\lambda_a(\boldsymbol{\beta}(\lambda_a) \cdot \boldsymbol{\Gamma} - E)$ and similarly for u_b. It follows that the matrices $\lambda_a(\boldsymbol{\beta}(\lambda_a) - E)$ and $\lambda_b(\boldsymbol{\beta}(\lambda_b) - E)$ must share a non-zero null vector, or equivalently, any linear combinations of the two matrices must be non-invertible. In other words, an edge state at energy E exists only if the following conditions [3] are satisfied:

$$\text{Det}\left[\lambda_a(\boldsymbol{\beta}(\lambda_a) \cdot \boldsymbol{\Gamma} - E)\right] = 0, \tag{10.7a}$$

$$\text{Det}\left[\lambda_b(\boldsymbol{\beta}(\lambda_b) \cdot \boldsymbol{\Gamma} - E)\right] = 0, \tag{10.7b}$$

$$\text{Det}\left[c_a\lambda_a(\boldsymbol{\beta}(\lambda_a) \cdot \boldsymbol{\Gamma} - E) + c_b\lambda_b(\boldsymbol{\beta}(\lambda_b) \cdot \boldsymbol{\Gamma} - E)\right] = 0, \tag{10.7c}$$

for arbitrary c_a, c_b and for $|\lambda_a|, |\lambda_b| < 1$. The converse statement is also true, as (10.7a) and (10.7b) implies that the ranks of the matrices $\lambda_{a,b}(\boldsymbol{\beta}(\lambda_{a,b}) \cdot \boldsymbol{\Gamma} - E)$ are at most half their dimension (a property of gamma matrices). The last equation (10.7c) means that the two matrices must share a right null vector or a left null vector. In the former case we have a left edge state at energy E, and in the latter case we have a right edge state at energy E, which by our lemma implies a left edge state at energy $-E$.

We may rewrite the equations in a more useful form:

$$\lambda_a^2 E^2 = \lambda_a^2 \boldsymbol{\beta}(\lambda_a) \cdot \boldsymbol{\beta}(\lambda_a), \tag{10.8a}$$

$$\lambda_b^2 E^2 = \lambda_b^2 \boldsymbol{\beta}(\lambda_b) \cdot \boldsymbol{\beta}(\lambda_b), \tag{10.8b}$$

$$\lambda_a\lambda_b E^2 = \lambda_a\lambda_b \boldsymbol{\beta}(\lambda_a) \cdot \boldsymbol{\beta}(\lambda_b). \tag{10.8c}$$

10.3 Introducing functions $L, \bar{L}$

Similar to $\mathbf{b}^0 = \mathbf{b}_{\parallel}^0 + \mathbf{b}_{\perp}^0$ and $\mathbf{h} = \mathbf{h}_{\parallel} + \mathbf{b}_{\perp}^0$, we decompose $\boldsymbol{\beta}$ into components parallel and perpendicular to the 2D plane (1D if the ellipse is degenerate) spanned by $\{\mathbf{b}^r, \mathbf{b}^i\}$: $\boldsymbol{\beta}(\lambda) = \boldsymbol{\beta}_{\parallel}(\lambda) + \mathbf{b}_{\perp}^0$ Keep in mind that while $\mathbf{b}_{\perp}^0$ is a real vector, $\boldsymbol{\beta}_{\parallel}(\lambda) = \lambda^{-1}\mathbf{b} + \mathbf{b}_{\parallel}^0 + \lambda\mathbf{b}^*$ is generally a complex vector, unless $\lambda = e^{ik}$ has unit modulus.

We want to find complex functions which trace out the same ellipse as $\boldsymbol{\beta}_{\parallel}(e^{ik})$ in the complex plane. We first choose two real orthogonal unit vectors $\hat{\mathbf{v}}_1, \hat{\mathbf{v}}_2$ as a coordinate basis[4] of the 2D plane. Let

$$\begin{aligned} L(\lambda) &= \boldsymbol{\beta}_{\parallel}(\lambda) \cdot \hat{\mathbf{v}}_1 + i\boldsymbol{\beta}_{\parallel}(\lambda) \cdot \hat{\mathbf{v}}_2, \\ \bar{L}(\lambda) &= \boldsymbol{\beta}_{\parallel}(\lambda) \cdot \hat{\mathbf{v}}_1 - i\boldsymbol{\beta}_{\parallel}(\lambda) \cdot \hat{\mathbf{v}}_2. \end{aligned} \tag{10.9}$$

The loci $L(e^{ik})$ and $\bar{L}(e^{ik})$ both trace out the ellipse in the complex plane identical to $\boldsymbol{\beta}_{\parallel}(e^{ik})$, but with different orientations. In general, $L(\lambda)$ and $\bar{L}(\lambda)$ are not conjugate pairs unless λ lies on the unit circle. Expanding their definitions, we can see that both $\lambda L(\lambda)$ and $\lambda\bar{L}(\lambda)$ are quadratic polynomials in λ:

$$\begin{aligned} L(\lambda) &= q\lambda + w + p\lambda^{-1}, \\ \bar{L}(\lambda) &= p^*\lambda + w^* + q^*\lambda^{-1}. \end{aligned} \tag{10.10}$$

---

[3]Equations (10.7a), (10.7b) are redundant, but useful to be written out explicitly.

[4]$\hat{\mathbf{v}}_1, \hat{\mathbf{v}}_2$ are a real coordinate basis such that we can always write $\boldsymbol{\beta}_{\parallel} = x_1\hat{\mathbf{v}}_1 + x_2\hat{\mathbf{v}}_2$, where x_1 and x_2 are complex numbers.

where $p = \mathbf{b} \cdot (\hat{\mathbf{v}}_1 + i\hat{\mathbf{v}}_2)$, $w = \mathbf{b}_\parallel^0 \cdot (\hat{\mathbf{v}}_1 + i\hat{\mathbf{v}}_2)$ and $q = \mathbf{b}^* \cdot (\hat{\mathbf{v}}_1 + i\hat{\mathbf{v}}_2)$.

It is straightforward to show from (10.9) that $\boldsymbol{\beta}_\parallel(\lambda_a) \cdot \boldsymbol{\beta}_\parallel(\lambda_b) = \frac{1}{2}(L_a\bar{L}_b + \bar{L}_aL_b)$, where $L(\lambda_a)$ is abbreviated as L_a, *etc.* Equations (10.8) become

$$\lambda_a^2(E^2 - \Delta^2) = \lambda_a^2 L_a\bar{L}_a, \tag{10.11a}$$

$$\lambda_b^2(E^2 - \Delta^2) = \lambda_b^2 L_b\bar{L}_b, \tag{10.11b}$$

$$\lambda_a\lambda_b(E^2 - \Delta^2) = \tfrac{\lambda_a\lambda_b}{2}(L_a\bar{L}_b + L_b\bar{L}_a), \tag{10.11c}$$

where $\Delta \equiv |\mathbf{b}_\perp^0|$.

10.4 Edge state energy

In this portion, we show that the existence of an edge state requires: $E = \pm\Delta$, $|\lambda_{a,b}| < 1$, and either $L_a = L_b = 0$ or $\bar{L}_a = \bar{L}_b = 0$. The converse statement is trivially true by inspecting Eq. (10.11). Hence if an edge state of the semi-infinite chain exists, we show here that it must have energy $E = \pm|\mathbf{b}_\perp^0|$. (First half of Thm. 1b.)

Assuming that neither λ_a or λ_b are zero, then

$$E^2 - \Delta^2 = L_a\bar{L}_a, \tag{10.12a}$$

$$E^2 - \Delta^2 = L_b\bar{L}_b, \tag{10.12b}$$

$$E^2 - \Delta^2 = \tfrac{1}{2}(L_a\bar{L}_b + L_b\bar{L}_a). \tag{10.12c}$$

which we can combine to get

$$(L_a - L_b)(\bar{L}_a - \bar{L}_b) = 0. \tag{10.13}$$

Equations (10.12) and (10.13) are simply reformulations of the recursion relation (10.1a) and boundary condition (10.1b). We now proceed to show that $E = \pm\Delta$.

Proof by contradiction Suppose that $E^2 - \Delta^2 \neq 0$. Then $L_a, L_b, \bar{L}_a, \bar{L}_b$ are all non-zero. Eq. (10.13) implies that $L_a = L_b$ or $\bar{L}_a = \bar{L}_b$. Eq. (10.12a) and (10.12b) together means that one equality implies the other, and hence $L_a = L_b$ and $\bar{L}_a = \bar{L}_b$ are both true. Here we have two polynomials with roots λ_a and λ_b:

$$q\lambda^2 + (w - L_a)\lambda + p = 0,$$

$$p^*\lambda^2 + (w^* - \bar{L}_a)\lambda + q^* = 0,$$

which means that $p/q = q^*/p^* = \lambda_a\lambda_b$. However, since $|\lambda_a\lambda_b| < 1$, we have a contradiction as $|p/q|$ cannot be less than one and greater than one at the same time. Hence we have shown, should an edge state exist, it must have energy $E = \pm\Delta$. Now (10.12a) tells us that either L_a or $\bar{L}_a$ is zero which combined with (10.13) leads to the desired result.

If one of λ_a, λ_b is zero, say $\lambda_b = 0$ (which happens when the ellipse is a circle), then the expressions simplify as $\lambda_b L_b = p$ and $\lambda_b \bar{L}_b = q^*$. From (10.11b), either $\lambda_b L_b$ or $\lambda_b \bar{L}_b$ is zero. From (10.11c) we have either $L_a = L_b = 0$ or $\bar{L}_a = \bar{L}_b = 0$, and in either case, (10.11a) implies that $E^2 - \Delta^2 = 0$.

If both λ_a and λ_b are zero (which happens when the circle is centered on the origin), then $\lambda = 0$ must be a double root to the polynomial (10.6). In this case, we have a flat band, and it is much easier to refer back to (10.1) and solve the system directly. One easily finds that the statement about edge states holds.

10.5 Existence of edge states

Finally, we use the fact that $|\lambda_a|, |\lambda_b| < 1$ to determine when an edge mode is present. Recall that there are four zeroes (and two poles) to the equation $L(\lambda)\bar{L}(\lambda) = 0$, and that at most two of the roots have modulus less than one. An edge mode exists if either $L(\lambda)$ or $\bar{L}(\lambda)$ has both roots λ within the unit circle. (No edge mode exists if each function $L, \bar{L}$ has one root within the unit circle.)

We can compute the number of zeroes (inside the unit circle) of the function L by the contour integral $\frac{1}{2\pi i} \oint \frac{L'(z)}{L(z)} dz$ along the unit circle, which computes the number of zeroes minus number of poles within the unit circle. As $L(\lambda)$ has one pole (at $\lambda = 0$), $L(\lambda)$ has two zeroes if and only if the ellipse $L(e^{ik})$ wraps around the origin counterclockwise, leading to an edge state. On the other hand, if L wraps around the origin clockwise, then $\bar{L}(e^{ik})$ wraps around the origin counterclockwise, and there are two zeroes for $\bar{L}(\lambda)$ within the unit circle which also leads to an edge state. In the case where the ellipse $\boldsymbol{\beta}_\parallel$ does not wrap the origin, then neither L or $\bar{L}$ has two roots within the unit circle, and an exponentially decaying solution to the semi-infinite system does not exist.

This completes the proof for Theorem 1a, which relates the presence of edge states to the properties of the ellipse $\boldsymbol{\beta}(e^{ik}) = \mathbf{h}(k)$.

10.6 Sign of edge state energy

In this section, we will determine whether the left edge state energy is $+\Delta$ or $-\Delta$, where $\Delta \equiv |\mathbf{b}_\perp^0| \geq 0$. This will complete the final statement of Thm. 1b.

Define $\hat{\mathbf{v}}_\perp$ as the unit vector parallel to $\mathbf{b}_\perp^0$ (assume $\Delta > 0$). Recall that $\hat{\mathbf{v}}_1, \hat{\mathbf{v}}_2$ are unit vectors used in the definitions of $L, \bar{L}$, and so the three unit vectors are mutually orthogonal. Define the corresponding gamma matrices $\Gamma^x = \hat{\mathbf{v}}_1 \cdot \boldsymbol{\Gamma}, \Gamma^y = \hat{\mathbf{v}}_2 \cdot \boldsymbol{\Gamma}, \Gamma^\perp = \hat{\mathbf{v}}_\perp \cdot \boldsymbol{\Gamma}$, which pairwise anticommute. As $\boldsymbol{\beta}_\parallel \cdot \hat{\mathbf{v}}_1 = \frac{1}{2}(L + \bar{L})$ and $\boldsymbol{\beta}_\parallel \cdot \hat{\mathbf{v}}_2 = \frac{1}{2i}(L - \bar{L})$,

$$\lambda(\boldsymbol{\beta}(\lambda) \cdot \boldsymbol{\Gamma} - E)) = \lambda(\Delta\Gamma^\perp - E) + \frac{\lambda L(\lambda)}{2}(\Gamma^x - i\Gamma^y) + \frac{\lambda \bar{L}(\lambda)}{2}(\Gamma^x + i\Gamma^y). \qquad (10.14)$$

The first term annihilates the projector $\frac{1}{2}(1 + \frac{E}{\Delta}\Gamma^\perp)$ while the second and third terms annihilate $\frac{1}{2}(1 + i\Gamma^x\Gamma^y)$ and $\frac{1}{2}(1 + i\Gamma^x\Gamma^y)$ respectively.

By inspection, the projector $P = \sum uu^\dagger$ on to the edge state depends on whether L or $\bar{L}$ has two zeroes inside the unit circle, as well as the energy E:

$$P_\pm = \begin{cases} \frac{1}{4}(1 \pm \Gamma^\perp)(1 - i\Gamma^x\Gamma^y) & L_a = L_b = 0 \\ \frac{1}{4}(1 \pm \Gamma^\perp)(1 + i\Gamma^x\Gamma^y) & \bar{L}_a = \bar{L}_b = 0 \end{cases}, \qquad (10.15)$$

where $P_\pm$ projects on to the edge states with energy $E = \pm\Delta$.

When the irreducible representations of $\boldsymbol{\Gamma}$ are 2×2, the product $i\Gamma^x\Gamma^y$ must equal either $\Gamma^\perp$ or $-\Gamma^\perp$, hence either P_+ or P_- must be zero. This implies that an edge state occurs only at Δ or $-\Delta$ but not both. For example, when $\Gamma^x\Gamma^y = i\Gamma^\perp$ and $L = 0$, then $P_+ = \frac{1}{2}(1 + \Gamma^\perp), P_- = 0$ and there is exactly one edge state at energy Δ. In general, we can determine E via the orientation of the ellipse $\mathbf{h}$:

$$E = \mathbf{b}^0 \cdot \frac{\mathbf{b}^r \times \mathbf{b}^i}{|\mathbf{b}^r \times \mathbf{b}^i|}, \tag{10.16}$$

where the cross product is defined from the commutation algebra $\mathbf{b}^r \times \mathbf{b}^i = -\frac{i}{4} \operatorname{Tr} \left\{ \boldsymbol{\sigma} \left[\mathbf{b}^r \cdot \boldsymbol{\sigma}, \mathbf{b}^i \cdot \boldsymbol{\sigma} \right] \right\}$. This result gives us Theorem 1b.

When the irreducible representations of $\boldsymbol{\Gamma}$ are $2^m \times 2^m$ with $m \geq 2$, there are edge states at both Δ and $-\Delta$. As $P_+ + P_- = \frac{1}{2}(1 \mp i\Gamma^x\Gamma^y)$, there are a total of 2^{m-1} left edge states. Notice that the projectors P_+ and P_- are related by the similarity transformation $P_+ = \Gamma^w P_- \Gamma^w$, where Γ^w anticommutes with $\Gamma^{x,y,\perp}$, and so there must be 2^{m-2} edge states at each energy.

10.7 Effective surface Hamiltonian

We can use the edge state projector to construct the effective surface Hamiltonian. The operator

$$P_s = P_+ + P_- = \tfrac{1}{2}(1 - i\Gamma^x\Gamma^y) \tag{10.17}$$

projects on to the edge states (assuming $\hat{\mathbf{v}}_1$ and $\hat{\mathbf{v}}_2$ are chosen such that $L = 0$). Notice that it only depends on $\mathbf{b} \cdot \boldsymbol{\Gamma}$, the nearest-neighbor coupling and not the on-site potential:

$$
\begin{aligned}
\tfrac{1}{2}(1 - i\Gamma^x\Gamma^y) &= \frac{1}{2}\left(1 - i\frac{[\mathbf{b}^r \cdot \boldsymbol{\Gamma}, \mathbf{b}^i \cdot \boldsymbol{\Gamma}]}{2|\mathbf{b}^r \times \mathbf{b}^i|}\right) \\
&= \frac{1}{2}\left(1 + \frac{[\mathbf{b} \cdot \boldsymbol{\Gamma}, \mathbf{b}^* \cdot \boldsymbol{\Gamma}]}{\frac{4}{\pi}(\text{Area of ellipse})}\right).
\end{aligned}
\tag{10.18}
$$

The effective surface Hamiltonian is

$$
\begin{aligned}
H_s &= EP_+ - EP_- + E_\infty(1 - P_s) \\
&= P_s(\mathbf{b}^0_\perp \cdot \boldsymbol{\Gamma}) + E_\infty(1 - P_s),
\end{aligned}
\tag{10.19}
$$

where $E_\infty \to \infty$ such that the low energy theory describes the surface states.

10.8 Proof for Continuum Hamiltonians

The proof of Theorem 3 is very similar to the proof of Theorem 1 using transfer matrices, and so we present here a condensed version of the proof.

Consider a semi-infinite system with $x \geq 0$, and either $\psi(0) = 0$ (Dirichlet) or $\psi'(0) = 0$ (Neumann) boundary condition. The momentum parallel to the surface is a good

quantum number, and so we fix $\mathbf{p}_\parallel$ to get an effective 1D problem. We seek a solution of the form[5] $\psi(x) = \sum_\mu e^{i\kappa_\mu x} u_\mu$, with $\operatorname{Im} \kappa_\mu > 0$. Each pair (κ, u) satisfies:

$$(C^0 + C^1\kappa + C^2\kappa^2 - E)u = (\mathbf{h}(\kappa) \cdot \mathbf{\Gamma} - E)u = 0. \tag{10.20}$$

Squaring $\mathbf{h} \cdot \mathbf{\Gamma}$ gives us the quartic equation

$$\mathbf{h}(\kappa) \cdot \mathbf{h}(\kappa) - E^2 = 0 \tag{10.21}$$

with real coefficients. Hence if κ is a root, then κ^* is also a root. Once again, we have at most two solutions for κ in the upper half of the complex plane, and so the wavefunction must take the form $\psi(x) = u_a e^{i\kappa_a x} + u_b e^{i\kappa_b x}$. With either Dirichlet ($u_a = -u_b$) or Neumann ($\kappa_a u_a = -\kappa_b u_b$) boundary condition, we have $u_a \propto u_b$ and so $\mathbf{h}(\kappa_a) \cdot \mathbf{\Gamma} - E$ and $\mathbf{h}(\kappa_b) \cdot \mathbf{\Gamma} - E$ share a null vector. By a similar argument to that in Sec. 10.2, the existence of an edge state is equivalent to

$$\operatorname{Det}\left[c_a(\mathbf{h}(\kappa_a) \cdot \mathbf{\Gamma} - E) + c_b(\mathbf{h}(\kappa_b) \cdot \mathbf{\Gamma} - E)\right] = 0, \tag{10.22a}$$

for all c_a, c_b and $\operatorname{Im} \kappa_a, \operatorname{Im} \kappa_b > 0$. Equivalently, we have

$$E^2 = \mathbf{h}(\kappa_a) \cdot \mathbf{h}(\kappa_a) = \mathbf{h}(\kappa_b) \cdot \mathbf{h}(\kappa_b) = \mathbf{h}(\kappa_a) \cdot \mathbf{h}(\kappa_b). \tag{10.23}$$

We introduce the functions $L(\kappa), \bar{L}(\kappa)$:

$$\begin{aligned} L(\kappa) &= \mathbf{h}_\parallel(\kappa) \cdot \hat{\mathbf{v}}_1 + i\mathbf{h}_\parallel(\kappa) \cdot \hat{\mathbf{v}}_2, \\ \bar{L}(\kappa) &= \mathbf{h}_\parallel(\kappa) \cdot \hat{\mathbf{v}}_1 - i\mathbf{h}_\parallel(\kappa) \cdot \hat{\mathbf{v}}_2, \end{aligned} \tag{10.24}$$

where $\hat{\mathbf{v}}_1, \hat{\mathbf{v}}_2$ form an orthonormal coordinate basis in the plane spanned by $\mathbf{c}^1$ and $\mathbf{c}^2$. $L(\kappa), \bar{L}(\kappa)$ are quadratic polynomials in κ:

$$\begin{aligned} L(\kappa) &= (c_x^0 + ic_y^0) + (c_x^1 + ic_y^1)\kappa + (c_x^2 + ic_y^2)\kappa^2 \\ \bar{L}(\kappa) &= (c_x^0 - ic_y^0) + (c_x^1 - ic_y^1)\kappa + (c_x^2 - ic_y^2)\kappa^2. \end{aligned} \tag{10.25}$$

When $\kappa = p$ is real, $L(p)$ and $\bar{L}(p)$ trace out the parabola $\mathbf{h}_\parallel(p)$ in the complex plane with opposite orientations. Using the relation $\mathbf{h}_\parallel(\kappa_a) \cdot \mathbf{h}_\parallel(\kappa_b) = \frac{1}{2}(L_a\bar{L}_b + \bar{L}_a L_b)$, where $\bar{L}(\kappa_a)$ is abbreviated as $\bar{L}_a$, *etc.*, Eq. (10.23) become

$$E^2 - \Delta^2 = L_a\bar{L}_a, \tag{10.26a}$$

$$E^2 - \Delta^2 = L_b\bar{L}_b, \tag{10.26b}$$

$$E^2 - \Delta^2 = \tfrac{1}{2}(L_a\bar{L}_b + L_b\bar{L}_a), \tag{10.26c}$$

where $\Delta \equiv |\mathbf{c}_\perp^0|$. The equations combine to get

$$(L_a - L_b)(\bar{L}_a - \bar{L}_b) = 0, \tag{10.27}$$

---

[5] A summand of the form $\kappa e^{i\kappa}$ is also permissible, provided κ is a double root of the polynomial (10.21).

Equations (10.26a), (10.26b) and (10.27) together with $\operatorname{Im}\kappa_{a,b} > 0$ are true if and only if an edge state exists at energy $\pm E$.

We construct a proof by contradiction showing that $E = \pm\Delta^2$. Suppose $E^2 \neq \Delta^2$, then all of $L_a, L_b, \bar{L}_a, \bar{L}_b$ are nonzero. Equating (10.26a) and (10.26b) gives $L_a/L_b = \bar{L}_a/\bar{L}_b$, and combining with (10.27) implies $L_a = L_b$ and $\bar{L}_a = \bar{L}_b$. Hence the polynomials $L(\kappa) - L_a$ and $\bar{L}(\kappa) - \bar{L}_a$ have identical roots (κ_a and κ_b). The sum of the roots $\kappa_a + \kappa_b$ must lie in the upper half plane, and it is equal to $(c_x^1 + ic_y^1)/(c_x^2 + ic_y^2)$ and $(c_x^1 - ic_y^1)/(c_x^2 - ic_y^2)$ from (10.25). This leads to a contradiction as the expressions are complex conjugate pairs. Therefore, an edge state requires $E = \pm\Delta$ and either $L_a = L_b = 0$ or $\bar{L}_a = \bar{L}_b = 0$.

Finally we impose the condition that $\operatorname{Im}\kappa_a, \operatorname{Im}\kappa_b > 0$. There are no poles in the function $L(\kappa)$, and so the number of zeroes in the upper half plane is given by $\frac{1}{2\pi i}\oint \frac{L'(z)}{L(z)}dz$, integrated along the real line from $-R$ to R and closed on the upper half plane $Re^{i\theta}$ for $0 \leq \theta \leq \pi$, where R is taken to infinity. Assuming that $\mathbf{c}^2$ is non-zero and so L is a quadratic function of z, the contour of $L(z)$ for $z = Re^{i\theta}$ always wraps the origin by 2π radians counterclockwise.

Hence $L(\kappa)$ has two roots in the upper half plane if and only if the parabola $L(p)$ wounds around the origin counterclockwise. Similarly, $L(\kappa)$ has zero roots (so $\bar{L}(\kappa)$ has two roots) in the upper half plane if the parabola wounds around the origin clockwise. An edge state exists in both these cases, which occur when the origin lies in the concave side of $\mathbf{h}_\parallel(p)$. If the origin is not in the concave side of the parabola $\mathbf{h}_\parallel(p)$, then $L(\kappa)$ and $\bar{L}(\kappa)$ only have one root in the upper half plane and the system has no edge states. This completes the proof for Theorem 3a.

To determine the sign of the edge states, we construct the projectors for $E = \pm\Delta$. The projectors in the continuum case is identical to that of the lattice case (10.15), hence by the same argument used for Thm. 1b, we can prove Theorem 3b.

$$E = \mathbf{c}^0 \cdot \frac{\mathbf{c}^1 \times \mathbf{c}^2}{|\mathbf{c}^1 \times \mathbf{c}^2|}. \tag{10.28}$$

In addition, one may also derive the effective surface Hamiltonian:

$$\begin{aligned} H_s &= EP_+ - EP_- + E_\infty(1 - P_s) \\ &= P_s(\mathbf{c}_\perp^0 \cdot \mathbf{\Gamma}) + E_\infty(1 - P_s), \end{aligned} \tag{10.29}$$

Bibliography

[1] A. R. Akhmerov and C. W. J. Beenakker. Boundary conditions for dirac fermions on a terminated honeycomb lattice. *Phys. Rev. B*, 77(8):085423, Feb 2008.

[2] A. R. Akhmerov, J. P. Dahlhaus, F. Hassler, M. Wimmer, and C. W. J. Beenakker. Quantized conductance at the majorana phase transition in a disordered superconducting wire. *Phys. Rev. Lett.*, 106(5):057001, Jan 2011.

[3] A. R. Akhmerov, Johan Nilsson, and C. W. J. Beenakker. Electrically detected interferometry of majorana fermions in a topological insulator. *Phys. Rev. Lett.*, 102(21):216404, May 2009.

[4] Jason Alicea. Majorana fermions in a tunable semiconductor device. *Phys. Rev. B*, 81(12):125318, Mar 2010.

[5] Jason Alicea, Yuval Oreg, Gil Refael, Felix von Oppen, and Matthew P. A. Fisher. Non-abelian statistics and topological quantum information processing in 1d wire networks. *Nature Physics*, 7:412–417, 2011.

[6] Alexander Altland and Martin R. Zirnbauer. Nonstandard symmetry classes in mesoscopic normal-superconducting hybrid structures. *Phys. Rev. B*, 55(2):1142–1161, Jan 1997.

[7] M. P. Anantram and S. Datta. Current fluctuations in mesoscopic systems with andreev scattering. *Phys. Rev. B*, 53(24):16390–16402, Jun 1996.

[8] J. E. Avron, R. Seiler, and B. Simon. Homotopy and quantization in condensed matter physics. *Phys. Rev. Lett.*, 51(1):51–53, Jul 1983.

[9] B. A. Bernevig, Taylor L. Hughes, and Shou-Cheng Zhang. Quantum Spin Hall Effect and Topological Phase Transition in HgTe Quantum Wells. *Science*, 314:1757–1761, December 2006.

[10] Michael V. Berry. Quantal phase-factors accompanying adiabatic changes. *Proc. Roy. Soc. Lond. A*, 392:45–57, March 1984.

[11] C. J. Bolech and Eugene Demler. Observing majorana bound states in p-wave superconductors using noise measurements in tunneling experiments. *Phys. Rev. Lett.*, 98(23):237002, Jun 2007.

[12] Parsa Bonderson, Sankar Das Sarma, Michael Freedman, and Chetan Nayak. A Blueprint for a Topologically Fault-tolerant Quantum Computer. unpublished, 2010.

[13] N. E. Bonesteel and Kun Yang. Infinite-randomness fixed points for chains of non-abelian quasiparticles. *Phys. Rev. Lett.*, 99(14):140405, Oct 2007.

[14] P. W. Brouwer, A. Furusaki, C. Mudry, and S. Ryu. Disorder-induced critical phenomena–new universality classes in Anderson localization. unpublished, 2005.

[15] Piet W. Brouwer, Mathias Duckheim, Alessandro Romito, and Felix von Oppen. Topological Superconducting Phases in disordered quantum wires with strong spin-orbit coupling. unpublished, 2011.

[16] David Carpentier, Pierre Pujol, and Kay-Uwe Giering. Random quantum ising chains with competing interactions. *Phys. Rev. E*, 72(6):066101, Dec 2005.

[17] A. H. Castro Neto, F. Guinea, N. M. R. Peres, K. S. Novoselov, and A. K. Geim. The electronic properties of graphene. *Rev. Mod. Phys.*, 81(1):109–162, January 2009.

[18] Y. L. Chen, J. G. Analytis, J. H. Chu, Z. K. Liu, S. K. Mo, X. L. Qi, H. J. Zhang, D. H. Lu, X. Dai, Z. Fang, S.-C. Zhang, I. R. Fisher, Z. Hussain, and Z.-X. Shen. Experimental Realization of a Three-Dimensional Topological Insulator, Bi_2Te_3. *Science*, 325:178–181, July 2009.

[19] N. R. Claughton and C. J. Lambert. Thermoelectric properties of mesoscopic superconductors. *Phys. Rev. B*, 53(10):6605–6612, Mar 1996.

[20] Chandan Dasgupta and Shang-keng Ma. Low-temperature properties of the random heisenberg antiferromagnetic chain. *Phys. Rev. B*, 22(3):1305–1319, Aug 1980.

[21] Andrew M. Essin, Joel E. Moore, and David Vanderbilt. Magnetoelectric Polarizability and Axion Electrodynamics in Crystalline Insulators. *Phys. Rev. Lett.*, 102(14):146805, April 2009.

[22] Daniel S. Fisher. Random transverse field ising spin chains. *Phys. Rev. Lett.*, 69(3):534–537, Jul 1992.

[23] Daniel S. Fisher. Random antiferromagnetic quantum spin chains. *Phys. Rev. B*, 50(6):3799–3821, Aug 1994.

[24] Daniel S. Fisher. Critical behavior of random transverse-field ising spin chains. *Phys. Rev. B*, 51(10):6411–6461, Mar 1995.

[25] Karsten Flensberg. Tunneling characteristics of a chain of majorana bound states. *Phys. Rev. B*, 82(18):180516, Nov 2010.

[26] Liang Fu and C. L. Kane. Josephson current and noise at a superconductor/quantum-spin-hall-insulator/superconductor junction. *Phys. Rev. B*, 79(16):161408, Apr 2009.

[27] Liang Fu and C. L. Kane. Probing neutral majorana fermion edge modes with charge transport. *Phys. Rev. Lett.*, 102(21):216403, May 2009.

[28] Liang Fu and Charles L. Kane. Time reversal polarization and a $\mathbb{Z}_2$ adiabatic spin pump. *Phys. Rev. B*, 74(19):195312, November 2006.

[29] Liang Fu and Charles L. Kane. Topological insulators with inversion symmetry. *Phys. Rev. B*, 76(4):045302, July 2007.

[30] Liang Fu and Charles L. Kane. Superconducting Proximity Effect and Majorana Fermions at the Surface of a Topological Insulator. *Phys. Rev. Lett.*, 100(9):096407, March 2008.

[31] Liang Fu, Charles L. Kane, and Eugene J. Mele. Topological Insulators in Three Dimensions. *Phys. Rev. Lett.*, 98(10):106803, March 2007.

[32] Martin Greiter, Xiao-Gang Wen, and Frank Wilczek. Paired hall state at half filling. *Phys. Rev. Lett.*, 66(24):3205–3208, Jun 1991.

[33] H. Büttner and E. Gerlach. On the extension of shockley surface states in metals. *Surface Science*, 32(3):687 – 693, September 1972.

[34] F. Duncan M. Haldane. Model for a quantum Hall effect without Landau levels: Condensed-matter realization of the "parity anomaly". *Phys. Rev. Lett.*, 61:2015–2018, October 1988.

[35] B. I. Halperin. Quantized hall conductance, current-carrying edge states, and the existence of extended states in a two-dimensional disordered potential. *Phys. Rev. B*, 25(4):2185–2190, February 1982.

[36] M. Z. Hasan and C. L. Kane. Colloquium: Topological insulators. *Rev. Mod. Phys.*, 82(4):3045–3067, Nov 2010.

[37] Yasuhiro Hatsugai. Chern number and edge states in the integer quantum hall effect. *Phys. Rev. Lett.*, 71(22):3697–3700, November 1993.

[38] P. Heinzner, A. Huckleberry, and M.R. Zirnbauer. Symmetry classes of disordered fermions. *Comm. in Math. Phys.*, 257:725–771, 2005.

[39] Pavan Hosur, Pouyan Ghaemi, Roger Mong, and Ashvin Vishwanath. Majorana modes at the ends of superconductor vortices in doped topological insulators. unpublished, 2010.

[40] Pavan Hosur, Shinsei Ryu, and Ashwin Vishwanath. Chiral topological insulators, superconductors, and other competing orders in three dimensions. *Phys. Rev. B*, 81(4):045120, January 2010.

[41] D. Hsieh, D. Qian, L. Wray, Y. Xia, Y. S. Hor, R. J. Cava, and M. Z. Hasan. A topological Dirac insulator in a quantum spin Hall phase. *Nature*, 452:970–974, April 2008.

[42] R. A. Hyman, Kun Yang, R. N. Bhatt, and S. M. Girvin. Random bonds and topological stability in gapped quantum spin chains. *Phys. Rev. Lett.*, 76(5):839–842, Jan 1996.

[43] D. A. Ivanov. Non-abelian statistics of half-quantum vortices in *p*-wave superconductors. *Phys. Rev. Lett.*, 86(2):268–271, January 2001.

[44] R. Jackiw and C. Rebbi. Solitons with fermion number $\frac{1}{2}$. *Phys. Rev. D*, 13(12):3398–3409, June 1976.

[45] R. Jackiw and J. R. Schrieffer. Solitons with fermion number $\frac{1}{2}$ in condensed matter and relativistic field theories. *Nuc. Phys. B*, 190(2):253–265, 1981.

[46] Charles L. Kane and Eugene J. Mele. $\mathbb{Z}_2$ Topological Order and the Quantum Spin Hall Effect. *Phys. Rev. Lett.*, 95:146802, September 2005.

[47] Charles L. Kane and Eugene J. Mele. Quantum Spin Hall Effect in Graphene. *Phys. Rev. Lett.*, 95:226801, November 2005.

[48] David B. Kaplan. A method for simulating chiral fermions on the lattice. *Phys. Rev. B*, 288:342–347, August 1992.

[49] J. R. Kirtley, C. Kallin, C. W. Hicks, E.-A. Kim, Y. Liu, K. A. Moler, Y. Maeno, and K. D. Nelson. Upper limit on spontaneous supercurrents in sr_2ruo_4. *Phys. Rev. B*, 76(1):014526, Jul 2007.

[50] A. Yu. Kitaev. Unpaired majorana fermions in quantum wires. *Phys. Usp.*, 44 (Suppl.)(131), 2001.

[51] Alexei Kitaev. Fault-tolerant quantum computation by anyons. *Ann. Phys. (N.Y.)*, 303:2–30, January 2003.

[52] Alexei Kitaev. Periodic table for topological insulators and superconductors. volume 1134, pages 22–30. L. D. Landau Memorial Conference "Advances in Theoretical Physics", AIP, May 2009.

[53] Markus König, Steffen Wiedmann, Christoph Brüne, Andreas Roth, Hartmut Buhmann, Laurens W. Molenkamp, Xiao-Liang Qi, and Shou-Cheng Zhang. Quantum Spin Hall Insulator State in HgTe Quantum Wells. *Science*, 318:766–770, November 2007.

[54] R. B. Laughlin. Quantized Hall conductivity in two dimensions. *Phys. Rev. B*, 23(10):5632–5633, May 1981.

[55] K. T. Law, Patrick A. Lee, and T. K. Ng. Majorana fermion induced resonant andreev reflection. *Phys. Rev. Lett.*, 103(23):237001, Dec 2009.

[56] D. H. Lee and J. D. Joannopoulos. Simple scheme for surface-band calculations. i. *Phys. Rev. B*, 23(10):4988–4996, May 1981.

[57] Andrew Peter Mackenzie and Yoshiteru Maeno. The superconductivity of $sr2ruo4$ and the physics of spin-triplet pairing. *Rev. Mod. Phys.*, 75(2):657–712, May 2003.

[58] E. Majorana. *Nuovo Cimento*, 5:171–184, 1938.

[59] Shijun Mao, Yoshio Kuramoto, Ken-Ichiro Imura, and Ai Yamakage. Analytic Theory of Edge Modes in Topological Insulators. unpublished, 2010.

[60] Roger S. K. Mong and Vasudha Shivamoggi. Edge states and the bulk-boundary correspondence in dirac hamiltonians. *Phys. Rev. B*, 83(12):125109, Mar 2011.

[61] Gregory Moore and Nicholas Read. Nonabelions in the fractional quantum hall effect. *Nuc. Phys. B*, 360(2-3):363–396, August 1991.

[62] J. E. Moore and L. Balents. Topological invariants of time-reversal-invariant band structures. *Phys. Rev. B*, 75(12):121306, Mar 2007.

[63] Joel E. Moore and Leon Balents. Topological invariants of time-reversal-invariant band structures. *Phys. Rev. B*, 75(12):121306(R), March 2007.

[64] Chetan Nayak, Steven H. Simon, Ady Stern, Michael Freedman, and Sankar Das Sarma. Non-abelian anyons and topological quantum computation. *Rev. Mod. Phys.*, 80(3):1083–1159, Sep 2008.

[65] Johan Nilsson, A. R. Akhmerov, and C. W. J. Beenakker. Splitting of a cooper pair by a pair of majorana bound states. *Phys. Rev. Lett.*, 101(12):120403, Sep 2008.

[66] Yuval Oreg, Gil Refael, and Felix von Oppen. Helical liquids and majorana bound states in quantum wires. *Phys. Rev. Lett.*, 105(17):177002, Oct 2010.

[67] Xiao-Liang Qi, Taylor L. Hughes, and Shou-Cheng Zhang. Topological field theory of time-reversal invariant insulators. *Phys. Rev. B*, 78(19):195424, November 2008.

[68] Xiao-Liang Qi, Yong-Shi Wu, and Shou-Cheng Zhang. General theorem relating the bulk topological number to edge states in two-dimensional insulators. *Phys. Rev. B*, 74(4):045125, July 2006.

[69] Xiao-Liang Qi and Shou-Cheng Zhang. The quantum spin hall effect and topological insulators. *Physics Today*, 63:33–38, 2010.

[70] Xiao-Liang Qi and Shou-Cheng Zhang. Topological insulators and superconductors. unpublished, 2010.

[71] N. Read and Dmitry Green. Paired states of fermions in two dimensions with breaking of parity and time-reversal symmetries and the fractional quantum hall effect. *Phys. Rev. B*, 61(15):10267–10297, April 2000.

[72] G. Refael and J. E. Moore. Entanglement entropy of random quantum critical points in one dimension. *Phys. Rev. Lett.*, 93(26):260602, Dec 2004.

[73] Gil Refael and Daniel S. Fisher. Energy correlations in random transverse field ising spin chains. *Phys. Rev. B*, 70(6):064409, Aug 2004.

[74] Rahul Roy. Topological phases and the quantum spin Hall effect in three dimensions. *Phys. Rev. B*, 79:195322, May 2009.

[75] Shinsei Ryu and Yasuhiro Hatsugai. Topological origin of zero-energy edge states in particle-hole symmetric systems. *Phys. Rev. Lett.*, 89(7):077002, Jul 2002.

[76] Shinsei Ryu, Andreas Schnyder, Akira Furusaki, and Andreas W. W. Ludwig. Topological insulators and superconductors: ten-fold way and dimensional hierarchy. *New J. Phys.*, 12:065010, June 2010.

[77] Jay D. Sau, Roman M. Lutchyn, Sumanta Tewari, and S. Das Sarma. Generic new platform for topological quantum computation using semiconductor heterostructures. *Phys. Rev. Lett.*, 104(4):040502, Jan 2010.

[78] Andreas P. Schnyder, P. M. R. Brydon, Dirk Manske, and Carsten Timm. Andreev spectroscopy and surface density of states for a three-dimensional time-reversal invariant topological superconductor. unpublished, 2010.

[79] Andreas P. Schnyder, Shinsei Ryu, Akira Furusaki, and Andreas W. W. Ludwig. Classification of topological insulators and superconductors in three spatial dimensions. *Phys. Rev. B*, 78(19):195125, November 2008.

[80] J. Robert Schrieffer. *Theory of Superconductivity*. Perseus Books, Reading, Massachusetts, 1999.

[81] Sodano P. Semenoff, G. W. Stretching the electron as far as it will go. *Electron. J. Theor. Phys.*, 10:157–190, 2006.

[82] Shun-Qing Shen, Wen-Yu Shan, and Hai-Zhou Lu. $\mathbb{Z}_2$ topological invariant and solutions of the Dirac equation. unpublished, 2010.

[83] V. Shivamoggi, G. Refael, and J. E. Moore. Majorana fermion chain at the quantum spin hall edge. *Phys. Rev. B*, 82(4):041405(R), Jul 2010.

[84] Barry Simon. Holonomy, the Quantum Adiabatic Theorem, and Berry's Phase. *Phys. Rev. Lett.*, 51(24):2167–2170, December 1983.

[85] Tudor Stanescu, Roman M. Lutchyn, and S. Das Sarma. Majorana Fermions in Semiconductor Nanowires. unpublished, 2011.

[86] W. P. Su, J. R. Schrieffer, and A. J. Heeger. Solitons in polyacetylene. *Phys. Rev. Lett.*, 42(25):1698–1701, June 1979.

[87] Jeffrey C. Y. Teo, Liang Fu, and C. L. Kane. Surface states and topological invariants in three-dimensional topological insulators: Application to $bi_{1-x}sb_x$. *Phys. Rev. B*, 78(4):045426, July 2008.

[88] Jeffrey C. Y. Teo and C. L. Kane. Topological defects and gapless modes in insulators and superconductors. *Phys. Rev. B*, 82(11):115120, September 2010.

[89] Sumanta Tewari, S. Das Sarma, and Dung-Hai Lee. Index theorem for the zero modes of majorana fermion vortices in chiral p-wave superconductors. *Phys. Rev. Lett.*, 99(3):037001, Jul 2007.

[90] D. J. Thouless, M. Kohmoto, M. P. Nightingale, and M. den Nijs. Quantized Hall Conductance in a Two-Dimensional Periodic Potential. *Phys. Rev. Lett.*, 49(6):405–408, August 1982.

[91] J. A. van Dam, Y. V. Nazarov, E. P. A. Bakkers, S. De Franchesci, and L. P. Kouwenhoven. Supercurrent reversal in quantum dots. *Nature*, 442:667–670, 2006.

[92] Xiao-Gang Wen. Topological orders and edge excitations in fractional quantum Hall states. *Advances in Physics*, 44:405–473, October 1995.

[93] R. L. Willett, L. N. Pfeiffer, and K. W. West. Measurement of filling factor 5/2 quasiparticle interference with observation of e/4 and e/2 period oscillations. *PNAS*, 106(22):8853–8838, 2009.

[94] Frank Wilzcek. Majorana Returns. *Nature Physics*, 5:614–618, 2009.

[95] Y. Xia, D. Qian, D. Hsieh, L. Wray, A. Pal, H. Lin, A. Bansil, D. Grauer, Y. S. Hor, R. J. Cava, and M. Z. Hasan. Observation of a large-gap topological-insulator class with a single Dirac cone on the surface. *Nature Physics*, 5:398–402, May 2009.

[96] Cenke Xu and Liang Fu. Fractionalization in josephson junction arrays hinged by quantum spin hall edges. *Phys. Rev. B*, 81(13):134435, Apr 2010.

[97] Haijun Zhang, Chao-Xing Liu, Xiao-Liang Qi, Xi Dai, Zhong Fang, and Shou-Cheng Zhang. Topological insulators in Bi_2Se_3, Bi_2Te_3 and Sb_2Te_3 with a single Dirac cone on the surface. *Nature Physics*, 5:438–442, May 2009.